**UPC** **CTTC**

# A new grey area mitigation technique for DDES. Theory and assessment.

Centre Tecnològic de Transferència de Calor
Departament de Màquines i Motors Tèrmics
Universitat Politècnica de Catalunya

Arnau Pont-Vílchez
Doctoral Thesis

# A new grey area mitigation technique for DDES. Theory and assessment.

Arnau Pont-Vílchez

TESI DOCTORAL

presentada al

Departament de Màquines i Motors Tèrmics
E.S.E.I.A.A.T.
Universitat Politècnica de Catalunya

per a l'obtenció del grau de

Doctor per la Universitat Politècnica de Catalunya

Terrassa, December 2020

# A new grey area mitigation technique for DDES. Theory and assessment.

Arnau Pont-Vílchez

**Directors de la Tesi**

Dr. Francesc Xavier Trias Miquel

Dr. Assensi Oliva Llena

**Tribunal Qualificador**

Dr. Eng. Charles Mockett
Upstream CFD GmbH

Dr. Joaquím Rigola
Universitat Politècnica de Catalunya

Dr. Tatiana Kozubskaya
Keldysh Institute of Applied Mathematics of Russian Academy of Sciences

*Aquesta tesi està dedicada als meus pares, Ramon i Leo,*

*i als meus germans, Ramon i Clara,*

*i a la meva companya de tots aquests anys, Judith.*

# Agraïments

La veritat és que sense el fet que el Prof. Assensi Oliva no hagués cregut en mi quan estava fent la carrera, res del que he viscut aquests anys hauria estat possible. Així que si a algú he de donar les gràcies, és a ell.

Aquesta aventura va començar amb un ordinador, amb un sistema operatiu que no sabia com funcionava i amb un munt de coses per aprendre. Sort de la meva companya a la dreta, la Roser Capdevila, que em va ajudar a canalitzar tot el que estava per venir. Gràcies Roser!

He de dir que el contingut d'aquesta tesi no hauria estat possible sense l'aportació de moltes persones. Tot i això, si a algú he de remarcar a aquí, aquest és al Xavi Trias, que més enllà d'un brillant tutor de tesis a acabat sent un bon amic. Gràcies Xavi!

També, no hi ha dubte, de la important contribució de l'Alistair Revell, que vaig tenir la sort de conèixer durant la meva estada a Manchester. També als amics que vaig fer allà, Marta, Sam, Ben, Azin and Philipp. Thank you Alistair and all of you "lads"!

Uns agraïments com aquests també es mereixen parlar dels que no han fet "*ni brot*" pel que fa a la tesi, però que són igual o més importants pels moments que hem passat junts. Sí, sí, em refereixo als següents bandarres: Ali Naseri, Kike Gutiérrez, Joan Calafell (àlies company!), Nico Valle, Xavier Álvarez, Eduard Bartrons i Nina Morozova. Gràcies, nois!

A tu Jesús Ruano, et guardo un lloc a part, perquè sempre ho has estat ja sigui per les xarrades o per les mil i una reflexions durant el doctorat. Company de penes, glòries, i també de gimnàs. Ets molt gran, gràcies!

...ara venen dos d'inigualables, d'aquells que fan màgia i resolen problemes quan més ho necessites. D'aquells que et foten canya i et fan emprendre nous reptes. Gràcies Octavi Pavon i Víctor Ruiz.

La família i els amics de Tàrrega es mereixen probablement pàgina i mitja d'agraïments, però seré breu dient que agraeixo el seu suport incondicional i fer del poble, un oasi aliè al doctorat.

Finalment a tu, per ser la meva companya d'infinitat d'aventures durant tots aquests anys. Per compartir infinitat de moments, els bonics i els també tristos. Un petó ben fort. Gràcies, Judith.

# Abstract

The use of hybrid RANS-LES methods has become widespread during the last decade, as an interesting approach for covering the gap between RANS and LES turbulence models in terms of both computational resources and degree of modelling. In particular, for those situations where the flow unsteadiness needs to be well-captured or those flow configurations where RANS has demonstrated to be unreliable, such as massive flow separation. Within the family of hybrid models, Delayed - Detached Eddy Simulation (DDES) outstands due to its user-friendly non-zonal approach and its proved success in several applications. Despite their benefits, these models usually suffer from a slow RANS to LES transition (named *Grey Area*), resulting in unphysical delays of critical flow instabilities in sensitive regions, such as Kelvin-Helmholtz structures in free shear layers. This delay in the triggering process could significantly affect the flow dynamics downstream of the flow, as well as those kind of physics that require high quality unsteady turbulent motion, such as fluid structure interaction and computational aeroacoustics. In this regard, the present thesis aims to perform a consistent study of different techniques for mitigating such delay, as well as presenting a promising easy-to-apply new strategy. Due to the lack of publicly available highly reliable data set, a Direct Numerical Simulation (DNS) of a Backward-Facing Step (BFS) at $Re_\tau = 395$ and expansion ratio (ER) 2 has been carried out during the first part of this thesis for comparison purposes. In contrast to the rest of reference cases, it provides a detailed view of the triggering and feeding processes of the flow instabilities through the free shear layer. As a result, the thesis provides a highly reliable data set publicly available on internet, as well as a competitive new technique for mitigating the *Grey Area* shortcoming.

The thesis content is arranged as follows. In the first chapter, a general overview of the different approaches for modelling turbulence is presented, emphasising the importance of the Hybrid RANS-LES strategies for industrial applications. In second chapter, the DNS of the BFS at $Re_\tau = 395$ and $ER = 2$ is explained in detail. Special attention is paid on the triggering of the flow instabilities in the free shear layer downstream the step-edge. The third chapter describes the new techniques proposed in this thesis, based on the LES literature, for mitigating the *Grey Area* shortcoming. These are tested in the fourth chapter, which presents a consistent study of the different methodologies for addressing the unphysical delay of the shear layer instabilities. Finally, the last chapter gathers the main conclusions of the overall thesis and defines possible further work lines.

# Contents

# List of Figures

# List of Tables

# 1

# Introduction

**Abstract.** In this introductory chapter, the chaotic motion defined by a fluid under certain conditions, commonly known as turbulence, is firstly described from both physical and mathematical perspective. This explanation naturally comes up with the need of turbulence models, setting the basis for introducing them and defining their pros and cons. The diverse family of turbulence models is discussed and justified depending on the application in terms of computational cost and degree of modelling. All this information is summarized by means of a simple flow configuration, observing the effects entailed by each modelization strategy. Finally, the main conclusions from this chapter are presented, justifying the need of doing research on Hybrid RANS-LES models for industrial applications, presenting a significant improvement in the quality of the data with a reasonable price increment.

## 1.1 Description of Turbulence

Turbulence is a branch of fluid mechanics, which explains the chaotic motion manifested by any fluid subjected under certain conditions. This motion is mathematically governed by the Navier-Stokes (NS) equations,

$$\underbrace{\partial_i u_i}_{Continuity} = 0; \qquad \underbrace{\partial_t u_i}_{Transient} + \underbrace{u_j \partial_j u_i}_{Convection} = \underbrace{-\partial_i p}_{Pressure\ Gradient} + \underbrace{\nu \partial_j^2 u_i}_{Difussion} + \underbrace{\sum f_i}_{Internal\ Forces} \tag{1.1}$$

which are a system of non-linear Partial Differential Equations (PDEs) discovered by *Claude-Louis Navier* and *George Gabriel Stokes* during the 19th century. These two transport equations define how both mass and momentum are conserved along space and time in any Newtonian fluid. In this case the fluid is considered incompresible (constant density, $\rho = ct$), so the *continuity* equation can be expressed such as $\partial_i u_i = 0$. Where $u_i$ referes to the velocity components, $p$ is the kinematic pressure, $\nu$ represents the kinematic viscosity and $\sum f_i$ can be used for any internal force, such as

gravity, buoyancy effects, electromagnetic forces etc. Hereafter, internal forces will not be longer mantained as they are out of the scope from this thesis and gravity effects can be directly absorved by the *Pressure Gradient* term.

In the end, the flow chaotic motion is naturally defined by the way how a fluid handles those superficial and internal forces applied on it. It obviously depends on the physical properties of each fluid (such as $\nu$), but also on the inherent condition of being a Newtonian fluid. By inherent, I mean having the *Convection* and *Diffusion* transport mechanisms, as well as ensuring the *Continuity* of an incompresible flow by means of the *Pressure Gradient*.

It is worth noting here that, while Navier-Stokes equations have been solved for lots of particular cases, a general analytical solution is not known yet (if any). This fact, together with the broad influence of turbulence in a vast range of industrial applications, justifies the necessity of applying numerical techniques for providing particular solutions to such complex equations.

### 1.1.1 Physical perspective

From a physical point of view, there is not an exact or accepted definition of turbulence, but there is a list of items that a flow state needs to satisfy in order to be considered as turbulent. These are:

- Apparent disorganization, nonrepeatability, chaotic...
- Three dimensionality, unsteady and rotational.
- Multiscale phenomenon.
- Substantial increasement of diffusion, mixing and dissipation.

Indeed, Navier-Stokes equations are able to provide solutions satisfying the above-mentioned requirements under certain conditions. Actually, expressing NS equations in its dimensionless form through the following conversions,

$$\hat{u}_i = u_i / U_{ref}; \qquad \hat{p} = p / \rho U_{ref}^2; \qquad \hat{x} = x / x_{ref}; \qquad \hat{t} = t U_{ref} / x_{ref}; \tag{1.2}$$

can help to understand when turbulence occurs,

$$\partial_i \hat{u}_i = 0; \qquad \partial_{\hat{t}} \hat{u}_i + \hat{u}_j \partial_j \hat{u}_i = -\partial_i \hat{p} + \frac{1}{Re} \partial_j^2 \hat{u}_i. \tag{1.3}$$

Where $U_{ref}$ and $x_{ref}$ are a reference velocity and dimension respectively, for a given domain and flow configurations. Reynolds value, $Re = U_{ref} x_{ref} / \nu$ is directly derived from the dimensionless procedure as a non-dimensional balancing term between

the *Convection* and *Diffusion* transport mechanisms. Analysing Eq. 1.3 we can see how high *Re* values entails that the diffusion need to be higher in order to balance the convection term. The only way to increase the dimensionless diffusion term is by increasing the deformation of the velocity field. The natural mechanism in nature for creating such flow deformations in a divergence free system, is by means of creating and destroying eddies (unsteady system). The process where these eddies are produced/destroyed and how the kinetic energy from the bigger eddies is transfered to the smaller eddies is known as turbulence. This is the general state of almost any engineering application, as the reference conditions are usually quite challenging (high $U_{ref}$ and/or $x_{ref}$ values). In those situations where the *Re* values are not high enough, nature has no need to trigger the above mentioned eddies. In other words, the required amount of diffusion for balancing the convective term is accomplished with a steady deformation of the velocity field. It is usually the case of highly viscouse fluids (such as oils) at low or moderate operation conditions (low $U_{ref}$ and/or $x_{ref}$ values). It is worth to point out that any fluid can behave in a laminar or turbulent manner, depending on its *Re* value.

This section provides some interesting insights of the NS equations from a physical perspective, focusing on 3 different well-known flow configurations. These are: homogeneous iostropic turbulence, boundary layers and free-shear layers.

**Homogeneous isotropic turbulence**

The dimensionless NS equations (Eq. 1.3) has shown how high *Re* values contribute to a rising of the non-linear effects into the conservation of momentum. This predominance is rapidly observed from a physical point of view, as the flow motion it is no longer laminar, becoming a complex movement represented by different scales of motion in space and time (multiscale). Citing a quote from Richardson [1]:

*Big whorls have little whorls,*
*which feed on their velocity;*
*And little whorls have lesser whorls,*
*And so on to viscosity.*

In fact, this is a short but good approach about what turbulence is and how it behaves. Some years later, the inspiring ideas behind this famous quote were mathematically expressed by Kolmogorov's theory of 1941 (*K41*), defining the kinetic energy transfer cascade process (Fig. 1.1). Or, in other words, the mechanism how big whorls create little whorls and so on to viscosity :

- *Large scales:* based on the domain geometry (anisotropic).
- *Integral scales:* the most energetic scales (anisotropic).

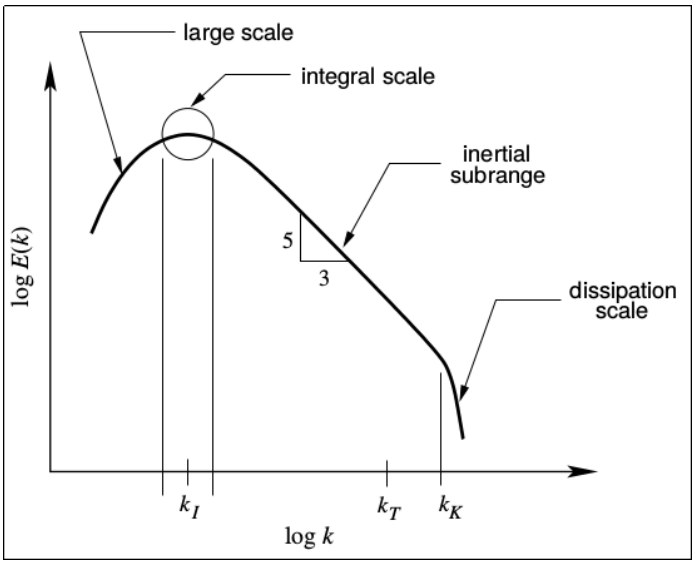


**Figure 1.1:** Turbulence energy wavenumber spectrum (McDonough [2]).

- *Inertial subrange:* set of isotropic scales where the kinetic energy is transfered from little scales to lesser scales.
- *Dissipation scales:* the smallest scales (isotropic), also known as *Kolmogorov scales*, are located at the cascade region where the main dissipation take place. Where the kinetic energy is converted in thermal energy by means of viscouse efforts.

Kolmogorov postulated that at high enough *Re* values, the anisotropy of the *Large scales* (induced by geometry) was lost through the cascade isotropization process, defending the universal isotropic character of the smallest scales, where the main dissipation takes place (*Kolmogorov scales*). The spatial, temporal and velocity scales of such particular structures can be estimated through dimensional analysis,

$$\eta = (\nu^3/\epsilon)^{1/4}; \quad \tau_\eta = (\nu/\epsilon)^{1/2}; \quad u_\eta = (\nu\epsilon)^{1/4}. \tag{1.4}$$

It can be observed how they depend only on $\nu$ and the dissipation rate $\epsilon$, so no matter their origin. Interesting research supporting this universal theory of the Kolmogorov scales can be found in Schummaher et al. [3], who studied the universal behaviour of the *Kolmogorov scales* originated by different sources (forced convection, buoyancy forces produced by natural convection, magnetohydrodynamic effects...). Apart from these interesting universality behaviour, *K41* also described the cascade

mechanism (Eq. 1.5) from the *integral scales* to the *dissipation scales* known as *inertial subrange*.

In contrast to the *integral scales*, this isotropic subrange was featured by having a net nonlinear transfer of energy from the large to the small scales, exhibiting then a constant dissipation rate between scales. In other words, a global dissipation rate close to 0. The dimensional analysis carried out by Kolmogorov deduced the following relation between scales in the inertial subrange

$$E(k) = C\epsilon^{2/3}k^{-5/3}, \tag{1.5}$$

where k referes to the wavenumber and C is a constant $\sim 1.5$ according to numerical observations. From an engineering point of view, knowing the existence of this iostropic well-defined behaviour is extremely important and useful, as it is the range of scales where turbulence can be easily predicted (so easily modeled).

**Boundary layer**

Near the wall vicinity, the maximum eddies' size is conditioned by the normal-wall distance. The zone where the wall dependence take place is known as boundary layer, which has its own particularities depending on *Re* value and the case geometry, but its general behaviour is quite similar. The instabilities triggered in such region are fed and propagated through the boundary layer, growing and sustaining turbulence in the whole domain. We can observe in figure 1.2 how a set of boundary layers obtained with different Reynolds values, can be defined with the same line using the proper scaling (except for the area away from the wall). This scaling is based on the friction velocity, which is defined as

$$u_\tau = \sqrt{\frac{\tau_w}{\rho}}. \tag{1.6}$$

Where $\tau_w$ represents the tangential efforts and $\rho$ is the fluid density. Those dimensionless values obtained with $u_\tau$ are commonly marked by $+$, such as $u^+ = u/u_\tau$ and $y^+ = y\nu/u_\tau$. A detailed explanation of the different flow regions [4] present in the boundary layer are described in table 1.1.

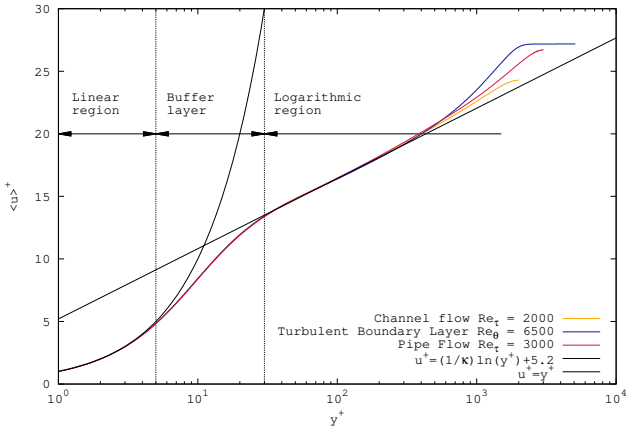


**Figure 1.2:** The law of the wall obtained through DNS of three different canonic flows: Channel flow at $Re_\tau \sim 2000$ [5] (orange line), a Flat plate turbulent boundary layer at $Re_\theta \sim 6500$ [6] (blue), and a Pipe flow at $Re_\tau \sim 2000$ [7] (red). The expressions of Prandtl and Von Karman are also shown. This figure was obtained from Calafell's PhD thesis [8].

**Table 1.1:** Classification of the different regions found within a boundary layer according to their physical behavior and properties. Their location is delimited by the distance to the wall, in wall units or as a fraction of $\delta$ depending on their physical properties. [4]

| Region | Location | Properties |
|---|---|---|
| Viscous sublayer | $y^+ < 5$ | The mean streamwise velocity is linear with respect to the wall distance, both in wall units $u^+ = y^+$. Viscous forces prevail over inertial ones. |
| Buffer layer | $5 < y^+ < 30$ | Region between the viscous sublayer and the log-law region. Turbulent instabilities are triggered |
| Log-law region | $y^+ > 30$<br>$y/\delta < 0.3$ | The mean streamwise velocity has a logarithmic behavior with respect to the wall distance, $u^+ = (1/\kappa)\ln y^+ + B$. The flow regime is predominantly turbulent. |
| Inner layer | $y/\delta < 0.1$ | The mean streamwise velocity scales with $u_\tau$ and is not affected by the far field velocity characteristic. |
| Outer layer | $y^+ > 50$ | The effects of the viscosity on the streamwise velocity are negligible. |
| Overlap region | $y^+ > 50$<br>$y/\delta < 0.1$ | Inner and outer layers are overlapped in this region (at high Reynolds numbers) |

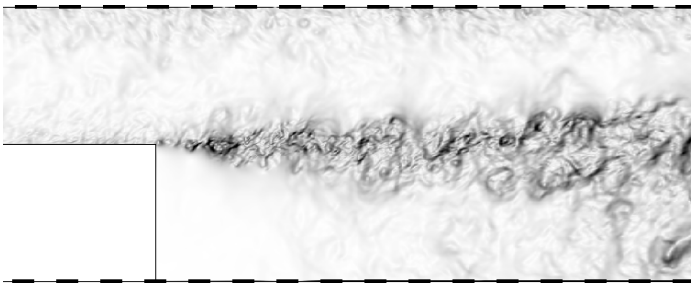

**Figure 1.3:** Pressure gradient magnitude in a free shear layer risen from a suddenly separated boundary layer in a Backward-Facing Step configuration [10].

Two subtables are shown in table 1.1. First, the different flow behaviours, depending on their scaling are shown. In the other hand, the second subtable shows a more general classification. The first group in the second subtable, the inner layer, includes all the layers influenced by the wall vicinity coefficients ($u_\tau$ and log-law), while in the outer layer, second group, the flow parameters are almost unaffected by the viscosity effects, and they scale with outer parameters (bulk velocity and $\delta$).

From an engineering point of view, the need of capturing the multiscale phenomenon present in any wall-bounded flow remains a critical point, as it dramatically increases the simulation computational cost in terms of both spatial and temporal resolution. In this context, several modelling strategies exist in the literature in order to address this shortcoming.

**Free shear layer**

Free shear layers are present in many different flow cofigurations, but its origin is often linked with separated boundary layers (Fig. 1.3). The instabilities triggered at free shear layer (Kelvin-Helmholtz instabilities) have some similarities with the wall-bounded flows, as both involve a shear layer in the feeding process. However, its origin is completely different, as the free shear layer instabilities size is not governed by the wall distance, but the velocity gradient and the average streamwise velocity. The information contained in this chapter, including pictures, has been mainly obtained from Jimenez [9]. The free shear layer behaviour scales following the similarity law,

$$\frac{u(x_2)}{\Delta U}, \frac{u'(x_2)}{\Delta U}, \cdots = f(x_2/x_1, \beta), \tag{1.7}$$

where $\Delta U = U_a - U_b$ is the velocity difference between streams in a plane shear layer (Fig. 1.4), $\beta = \Delta U/2U_c$ and $U_c$ is the average mean velocity, $(U_a + U_b)/2$.

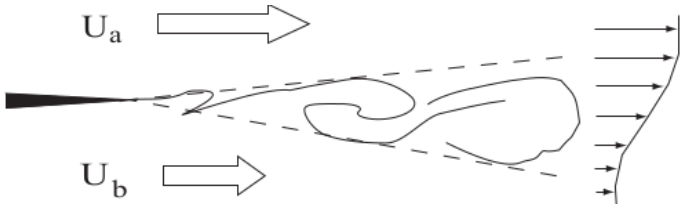


**Figure 1.4:** Schematic view of a plane shear layer [9].

The root-mean-square (*rms*) has been represented as $u'$. A probe of this similarity is figure 1.5, where the theory is compared with different experimental results. The growing behaviour of the Kelvin-Helmholtz instabilities can be explained using the pairing approach, as once the vorticity waves stop being linearly amplified, nonlinearity takes over. The final result of the Kelvin–Helmholtz instability is that the vorticity tends to concentrate and, in the nonlinear regime, collapses into discrete vortex blobs in a process named *pairing*. This is a process of mutual deformation between vortices, resulting in a new row of vorticity clouds, each of which has twice the circulation of the original ones. The time between mergings also doubles, and the result is a system that grows linearly in the average, but whose growth happens in discrete steps instead of smoothly. This process resembles an inverse cascade of growing vortex cores [9]. Even though this theory is defined in 2D, interesting similarities can be observed in 3D (such as the Backward-Facing Step in figure 1.3), due to the strong 2D behaviour of free shear layers in 3D domains.

All free shear layers share some common properties obtained from linear stability theory or following the vortex pairing picture, such as being thin and slowly-spreading, as well as having large-scale structures of the order of the width of the flow and perturbation velocities of the order of the velocity difference across the shear. Understanding free shear layers is important as they act as noise sources and also increase dissipation (increasing drag forces). Moreover, it is also an excellent mixing mechanism when two species are considered, being of special interest for chemical industry or combustion applications.

### 1.1.2 Mathematical perspective

From a mathematical point of view, turbulence could be defined as any solution of the Navier-Stokes equations at high enough *Re* value [12]. Even though it can seem a quite rough description, it is another manner to explain a phenomenon which has no clear definition. So, definitely, it can be easily added to the long list of items that a flow state needs to satisfy in order to be considered turbulent (defined in section 1.1.1). This section pretends to provide some interesting insights of the NS equations from

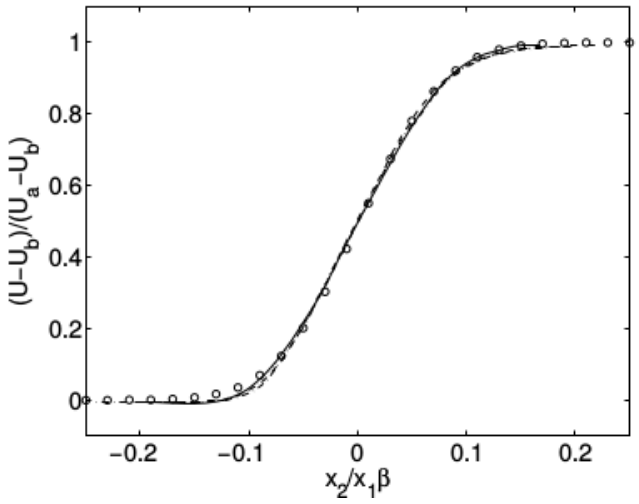


**Figure 1.5:** Mean streamwise velocity [11] in a plane shear layer at different conditions, $\beta x_1/\theta_o$, where $\theta_o$ is the initial momentum thickness [9]. —·—, 40; ----- 60; ·····, 90; ——, 135. The numerical theory is represented in ○.

a Mathematical perspective. In particular, the following topics are commented: NS equations expressed in the Fourier space; relation between the vortex-streching term with the multi-scale turbulence behaviour and a short introduction showing the importance of numerical conservative schemes in the convective term.

**Fourier descomposition of the NS equations**

The content of this section has been obtained from the document entitled "*Introductory Lectures on Turbulence*" written by McDonough [2]. The monograph by Canuto et al. [13] is recommended for those who are interested on this matter.

The representation of a simplified 1D form of the dimensionless Eqs. 1.3 in the Fourier space can help to deduce the mechanism how momentum is transported in NS flows. First, the dependent variables are converted in the Fourier space:

$$\hat{u}(\hat{x},\hat{t}) \quad = \quad \sum_{\mathbf{k}}^{\infty} a_{\mathbf{k}}\phi_{\mathbf{k}}(\hat{x}) \tag{1.8}$$

Where $\mathbf{k}$ is a wavevector in 1D space, so it could be expressed as $\mathbf{k} \equiv (k_1)^T$. For convenience we assume periodic boundary conditions naturally leading to a complex

exponential basis of functions, so

$$\phi_{\mathbf{k}}(\hat{\mathbf{x}}) = e^{i\mathbf{k}\cdot\hat{\mathbf{x}}} = e^{ik_1\hat{x}} \tag{1.9}$$

This conversion can be easily applied in the different terms defined in Eq. 1.3 (1D), leading to an expression which define the interaction between different wavenumbers. The influence of *Diffusion* term is firstly studied,

$$\underbrace{\partial_{\hat{t}} a_{\mathbf{k}}}_{Transient} = -\underbrace{\frac{|\mathbf{k}|^2}{Re} a_{\mathbf{k}}}_{Diffusion}, \tag{1.10}$$

obtaining its analytical solution in 1D

$$a(\hat{t}) = a(0)e^{-\frac{|\mathbf{k}|^2}{Re}\hat{t}}. \tag{1.11}$$

Due to the linearity of the Laplacian operator ($\partial_j^2$) in the *Diffusion* term, Eq. 1.11 shows how there is no interaction between different wavenumbers. Even though $\mathbf{k}$ is an infinite series, from a numerical point of view the maximum wavenumber is defined by the given mesh. Apart from that, Eq. 1.11 also shows how this solution always decays in time approaching to 0 ($t \to \infty$) and the rate how it occurs ($|\mathbf{k}|^2/Re$). This ratio shows how high wavenumbers are dissipated quicker than those which are lower. Moreover, it also shows how the higher the Reynolds value, the lower are the dissipation effects of a given wavenumber. This feature directly impacts on the energy cascade (section 1.1.1), explaining why kinetic energy is mainly dissipated at higher scales (higher wavenumbers) and why higher Reynolds values involves longer cascades.

In contrast to the *Diffusion* term, *Convection* behaves in a completely different manner, as can be observed once the Fourier conversion is applied,

$$\hat{u}\partial_{\hat{x}}\hat{u} = \frac{1}{2}\partial_{\hat{x}}\hat{u}\hat{u} = \frac{\partial}{\partial\hat{x}}\sum_{\mathbf{l},\mathbf{m}}^{N} a_{\mathbf{l}}a_{\mathbf{m}}\phi_{\mathbf{l}}(\hat{x})\phi_{\mathbf{m}}(\hat{x}) \tag{1.12}$$

where

$$\phi_{\mathbf{l}}(\hat{x})\phi_{\mathbf{m}}(\hat{x}) = e^{i\mathbf{l}\hat{x}}e^{i\mathbf{m}\hat{x}} = e^{i(\mathbf{l}+\mathbf{m})\hat{x}}. \tag{1.13}$$

The non-linearity of this term is defined by $\mathbf{k}+\mathbf{m}$, indicating the ability for generating new modes. These new wavenumbers will create even higher wavenumbers, so creating smaller vortices and contributing to the extension of the cascade phenomenon. Finally, the highest wavenumbers will be dissipated by the diffusion term, according to the behaviour observed in Eq. 1.11.

**Vortex stretching phenomenon**

A set of tranport equations can be directly derived from the NS equations, providing useful insights about how those other properties directly related to the velocity field behave in the space-time continuum. A probe of that is the flow vorticity ($\omega_i$),

$$\omega_i = \varepsilon_{ijk}\partial_j u_k \tag{1.14}$$

which is ruled by the following tranport equation

$$\partial_t \omega_i + \underbrace{u_j \partial_j \omega_i}_{Convection} = \underbrace{\omega_j \partial_j u_i}_{V.\ Stretching} + \underbrace{\nu \partial_j^2 \omega_i}_{Diffusion} . \tag{1.15}$$

This is naturally obtained applying the rotational operator into Eq. 1.1 (without considering internal forces). Apart from the classical *Convection* and *Diffusion* transport mechanisms, a particular extra term named *Vortex Stretching* is emerged. This term causes the vortex rupture in smaller vortices, increasing vorticity values and spreading it in all directions. In order to better understand how this term behaves, a simple example is provided decomposing *Vortex Stretching* and analysing its impact into the transient term

$$\partial_t \omega_1 \propto \underbrace{\omega_1 \partial_1 u_1}_{Stretching} + \underbrace{\omega_2 \partial_2 u_1 + \omega_3 \partial_3 u_1}_{Tilting} \tag{1.16}$$

The *Stretching* term shows how $\omega_1$ increases when $\omega_1$ and $\partial_1 u_1$ are aligned, resulting in a vortex stretching as mass and angular momentum ($r^2\omega_1$) must be conserved. Apart from that, *Tilting* terms are also important as they switch vorticity from one direction to another, through a tilting vortex process. The same explanation can be applied into the other 2 directions, exhibiting its clearly 3D tendency and obviously contributing to the turbulence cascade process. It is worth noting here that *Vortex Stretching* does no exist in a 2D approach, supporting the idea that turbulence is clearly a 3D phenomenon.

**Kinetic Energy Conservation**

Kinetic energy transport conservation equation can be derived from the NS equations, similarly to the vorticity transport equation (Eq. 1.15). Instead of applying the rotational operator, NS equations (Eq. 1.1) are multiplied by the velocity field,$u_i$ (inner product). As a result, the following transport equation is obtained

$$\partial_t k + \underbrace{u_j \partial_j k}_{Convection} = \underbrace{\nu \partial_j^2 k}_{Difussion} \underbrace{-\nu \partial_j k \partial_j k}_{Disspation} . \tag{1.17}$$

Again, apart from obtaining the classical *Convection* and *Diffusion* transport mechanisms, a new term naturally derived from *Diffusion* (Eq. 1.1)

$$\nu u_i \partial_j^2 u_i = \nu \partial_j^2 k - \nu \partial_j k \partial_j k \tag{1.18}$$

comes in (*Dissipation*). This definite negative term clearly contributes to a decreasement of the flow kinetic energy, $k = u_j u_j / 2$. The most interesting result in this derivation is the fact that there are no dissipation physical effects derived from *Convection* (Eq. 1.1). This is a feature in the continuum space-time, which should be preserved for any numerical scheme applied in the *Convection* term. In the literature, those convective schemes which preserve this property are known as *symmetry-preserving* schemes. Otherwise, any kind of extra dissipation introduced by the discretization will have a numerical non-physical origin, harming all mechanism involved in turbulence, such as the turbulent cascade, free-shear layers and boundary layers.

## 1.2 Turbulence Modelling

Few analytical solutions of the NS equations are currently available in the literature, due to the inherent complex non-linearity of such equations. Even though they treat rather simple flow configurations, these studies set the basis for understanding more complex flow behaviours. However, it is not enough for dealing with the problems faced by industry nowadays. For this reason, and because the breathtaking growth rate of the computational resources during the last decades, the only feasible approach seems to be solving the NS equations by means of numerical simulations. Unfortunately, at high Reynolds values, the numerical resolution of the NS equations can become an extremelly expensive action, usually impossible to achieve. Mainly, this is because of the NS non-linearity term (commented in section 1.1.2), as it generates new modes which will interact with the existing ones, generating higher frequency modes (smaller scales) and contributing to the kinetic energy cascade process (commented in section 1.1.1). The first idea for significantly decreasing the required amount of computational resources is based on not simulating the entire cascade. However, it can lead to multiple numerical issues as the behaviour of the simulated part clearly depends on the one that is not being simulated. Ideally, the effect of the non-simulated part of the cascade would be modelled in the part that is being simulated. This is where the turbulence modellization strategies take place (figure 1.6).

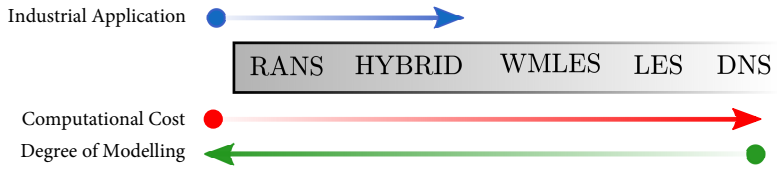


**Figure 1.6:** Scheme showing the different turbulence modelling strategies, including the use of computational resources, degree of modelling and how used they are for industrial applications.

Apart from their pros and cons, each strategy is compromised with a balance between computational cost and degree of modelling. It is definitely a big challenge considering that the way the eddies interact to each other is governed by a non-linear system of equations. In this section, the main methodologies are briefly described, showing only those details which are considered necessary for ensuring the good thesis comprehension.

### 1.2.1 Reynolds-Averaged Navier-Stokes (RANS)

RANS models are based on applying a temporal averaging into the NS equations, completely modelling the cascade process, or in other words, entirely removing any evidence of scale and modelling their effect into the mean flow. The Reynolds decomposition

$$u_i = \bar{u}_i + u_i'; \qquad p = \bar{p} + p', \tag{1.19}$$

where

$$\overline{u_i} = \overline{\bar{u}_i + u_i'} \quad \rightarrow \quad \overline{u_i} = \overline{\bar{u}_i} + \cancelto{0}{\overline{u_i'}} \quad \rightarrow \quad \bar{u}_i = \bar{u}_i, \tag{1.20}$$

is applied to the NS, where $\bar{u}_i$ and $\bar{p}$ are the time average variables that only depends on space, but not time. Therefore, continuity equation leads to

$$\begin{aligned} \overline{\partial_i(\bar{u}_i + u_i')} &= 0 \\ \overline{\partial_i \bar{u}_i} + \cancelto{0}{\overline{\partial_i u_i'}} &= 0 \\ \partial_i \bar{u}_i &= 0 \end{aligned} \tag{1.21}$$

the conservation of the average flow $\partial_i \bar{u}_i$, directly ensuring the conservation of the flow oscillations, $\partial_i u_i'$. Regarding the momentum equation, the Reynolds decomposi-

tion is also applied

$$\begin{aligned}
\overline{\partial_t(\bar{u}_i + u_i') + (\bar{u}_j + u_j')\partial_j(\bar{u}_i + u_i')} &= \\
\overline{-\partial_i(\bar{p} + p') + \nu\partial_j^2(\bar{u}_i + u_i')} & \\
\overline{\partial_t\bar{u}_i} + \overline{\partial_t u_i'} + \overline{\bar{u}_j\partial_j\bar{u}_i} + \overline{u_j'\partial_j\bar{u}_i} + \overline{\bar{u}_j\partial_j u_i'} + \overline{u_j'\partial_j u_i'} &= \\
-\overline{\partial_i\bar{p}} - \overline{\partial_i p'} + \overline{\nu\partial_j^2\bar{u}_i} + \overline{\nu\partial_j^2 u_i'} & \\
\partial_t\bar{u}_i + \cancelto{0}{\partial_t\bar{u'}_i} + \bar{u}_j\partial_j\bar{u}_i + \cancelto{0}{\bar{u'}_j\partial_j\bar{u}_i} + \cancelto{0}{\bar{u}_j\partial_j\bar{u'}_i} + \overline{u_j'\partial_j u_i'} &= \\
-\partial_i\bar{p} + \cancelto{0}{-\partial_i\bar{p'}} + \nu\partial_j^2\bar{u}_i + \cancelto{0}{\nu\partial_j^2\bar{u'}_i} &
\end{aligned} \tag{1.22}$$

resulting in

$$\partial_t\bar{u}_i + \bar{u}_j\partial_j\bar{u}_i = -\partial_i\bar{p} + \nu\partial_j^2\bar{u}_i - \partial_j(\underbrace{\overline{u_i'u_j'}}_{RS}). \tag{1.23}$$

Due to the non-linearity of the NS equations, an extra term named *Reynolds stresses* (RS) emerges from the convective term, representing the global effect of turbulence into the mean flow. As can be observed, it is an unclosured problem, as there are more unknowns than equations. Any approach with the aim of closing the system of equations is known as a RANS turbulence model. In the literature, several different RANS models can be found, but the most widely used are based on the Boussinesq turbulence approximation,

$$\begin{aligned}
-\left(\overline{u_i'u_j'} - 2/3k\delta_{ij}\right) &= 2\nu_t\overline{\hat{S}_{ij}} \\
-\overline{u_i'u_j'} &= \nu_t\left(\partial_j\bar{u}_i + \partial_i\bar{u}_j - 2/3\partial_k\bar{u}_k\delta_{ij}\right) - 2/3k\delta_{ij},
\end{aligned} \tag{1.24}$$

where

$$k = 1/2\overline{u_k'u_k'}. \tag{1.25}$$

Boussinesq stated a proportional relation between the trace-less *Reynolds stresses* and the trace-less mean strain rate tensor ($\overline{\hat{S}_{ij}}$). This proportionality was defined by $\nu_t$, a scalar property called *kinetic eddy viscosity* due to the strong analogy with the kinetic molecular viscosity ($\nu$). Following this approach, the closure problem is significantly simplified as there is only one variable to model $\nu_t$, instead of the six variables from the *Reynolds stresses* symmetric tensor, $\underbrace{\overline{u_i'u_j'}}_{RS}$. RANS models based on

the Boussinesq approximation can be classified in the zero-, one- or two- equation models depending on the number of extra equations needed for the $\nu_t$ definition. There are more complex RANS models, such as Reynolds Stress Models (RSM), which define six tranport equations for the six independent *Reynolds Stresses*. Even though these models are more accurate, they are also significantly more expensive as six extra transport equations must be solved, and also can lead to stability issues.

Probably, RANS is the most widely used turbulence modelling technique as it is the most economic modellization option and provides an acceptable level of accuracy in a wide range of cases. Their tunning capabilities are also appreciated, as case specific strategies can be applied for optimization purposes. However, RANS models have also some important shortcoming entailed to their nature, such as their incapability for providing accurate unsteady solutions in most cases.

### 1.2.2 Large Eddy Simulation (LES)

LES is based on a spatial averaging ($\widetilde{\square}$), filtering those scales higher than a certain frequency in the inertial subrange region (Fig. 1.1). It means that all large and integral scales are completely resolved ($\tilde{u}_i$), as well as part of the inertial subrange scales. For resolving such scales, time step needs to be in conjunction with the level of mesh refinement. Otherwise the inertial subrange will not be properly resolved, leading to a wrong LES simulation. Any LES simulation is based on applying a LES decomposition to the dependent variables,

$$u_i = \tilde{u}_i + u_i''; \qquad p = \tilde{p} + p'', \tag{1.26}$$

where

$$\widetilde{u_i} = \widetilde{\tilde{u}_i + u_i''} \tag{1.27}$$

$$\tilde{u}_i = \tilde{\tilde{u}}_i + \widetilde{u''}_i \tag{1.28}$$

$$\tilde{\tilde{u}}_i \neq \tilde{u}_i; \quad \widetilde{u''}_i \neq 0 \tag{1.29}$$

In contrast to the RANS decomposition, $\tilde{u}_i$ includes resolved scales, so it depends on space and time, whereas $u_i''$ represents those scales which are too small (high frequencies) for being resolved. This decomposition is applied into the filtered NS equations, leading to

$$\begin{aligned}
\widetilde{\partial_t u_i + u_j \partial_j u_i} &= \widetilde{-\partial_i p + \nu \partial_j^2 u_i} \\
\partial_t \tilde{u}_i + \widetilde{u_j \partial_j u_i} &= -\partial_i \tilde{p} + \nu \partial_j^2 \tilde{u}_i \\
\partial_t \tilde{u}_i + \partial_j \widetilde{u_j u_i} &= -\partial_i \tilde{p} + \nu \partial_j^2 \tilde{u}_i
\end{aligned} \tag{1.30}$$

where,

$$\widetilde{u_j u_i} = \tilde{u}_j\tilde{u}_i + (\widetilde{u_j u_i} - \tilde{u}_j\tilde{u}_i) = \tilde{u}_j\tilde{u}_i + (\widetilde{(\tilde{u}_j + u_j'')(\tilde{u}_i + u_i'')} - \tilde{u}_j\tilde{u}_i) = \tilde{u}_j\tilde{u}_i + \underbrace{(\widetilde{\tilde{u}_j\tilde{u}_i} + \widetilde{u_j''\tilde{u}_i} + \widetilde{\tilde{u}_j u_i''} + \widetilde{u_j'' u_i''} - \tilde{u}_j\tilde{u}_i.)}_{\tau_{ij}^{SGS}} \quad (1.31)$$

The subgrid stress tensor, $\tau_{ij}^{SGS}$, represents the effect of the filtered scales into the resolved scales. As can be observed, $\tau_{ij}^{SGS}$ is based on the interaction of different filtered scales (Eq. 1.31), such as $\widetilde{\tilde{u}_j\tilde{u}_i} - \tilde{u}_j\tilde{u}_i$ or $\widetilde{u_j'' u_i''}$. During the early days of LES, these coefficients were treated separatelly. However, it was demonstrated by Sagaut [14] that these terms are not Galilean invariant when they are individually treated, recommending then a modellization of the $\tau_{ij}^{SGS}$ as a single entity.

$$\partial_t\tilde{u}_i + \tilde{u}_j\partial_j\tilde{u}_i = -\partial_i\tilde{p} + \nu\partial_j^2\tilde{u}_i - \partial_j\tau_{ij}^{SGS} \quad (1.32)$$

In this context, several LES models are available in the literature, from those which consider simple turbulence flow configurations (*Smagorinksy*) to those which are sensitive to complex effects such as wall-bounded flows or 2D-like flow behaviours ($\sigma - LES$, $S3PQR$). These models are not explained in detail in this section, as we consider that they are not needed for introduction purposes. Therefore, it is clear that in a LES simulation only the effect of the highest frequencies (part of the subrange scales and dissipation scales) is modeled. These scales are intensively affected by the vortex-stretching 3D mechanism (section 1.1.2), so completely losing any kind of trend inherited from the case geometry. Hence, LES models are usually benefited for considering these high frequency scales isotropic. Problems arise when complex flow configurations appear, such as wall-bounded flows (section 1.1.1), where the above-mentioned resolved scales are already extremely small, requiring finer meshes and smaller time-steps. In contrast to RANS, where a time average filter is applied, LES simulations are always unsteady and a correct cascade process needs to be ensured. In particular, the main requirement recommended for guaranteeing a proper LES simulations are:

- Simulating a 3D domain is needed as turbulence multiscale process is a 3D phenomenon.
- Ensuring a good level of refinement in all directions, able to partially resolving those scales located at the inertial subrange. The time-step need to be in conjunction with the spatial refinement.

- The statistically stationary state needs to be reached before starting the averaging process.
- Once the statistically stationary state is achieved, data needs to be averaged during a certain period of time (case specific property) in order to obtain the mean properties (first and second order statistics are the most common).

All these requirements makes LES simulations extremely expensive in comparison with RANS, supporting the scheme shown in figure 1.6. The high quality average and unsteady data provided by proper LES simulations is indeed consistent with their extra computational cost. Even though LES is also an option for industrial applications, its use is rather limited to specific products developed by high-tech industries such as nuclear energy and aeronautical sectors. The rest of current applications are purely academic.

### 1.2.3 Wall Modeled Large Eddy Simulation (WMLES)

The main content of this subsection has been extracted from the recent PhD thesis presented by Calafell [8], which is fully dedicated to WMLES subject. Wall modeled Large Eddy Simulation is an active research field given the promising benefits of this approach respect to the classical LES, also named Wall Resolved LES (WRLES). The strategy is based on taking advantage of the temporal and spatial accuracy of the LES methodology while avoiding the unaffordable requirements imposed by the presence of a solid wall.

Some works in the literature intended to quantify tha gains using WMLES instead of WRLES, such as Chapman [15] or Choi and Moin [16]. Both of them carried out their studies based on a turbulent boundary layer over a flat plate case, denoted as $L_x$. Chapman proposed a mesh resolution proportional to $Re_{L_x}^{9/5}$ and $Re_{L_x}^{2/5}$ for WRLES and WMLES, respectively. Three decades later, Choi and Moin [16] updated the Chapman's work, leading to a mesh resolution proportional to $Re_{L_x}^{13/7}$ and $Re_{L_x}$. However, those works did not consider the significant restrictions of the time step into the overall computational cost. Calafell [17] proposed an estimation considering the well-known time step CFL (Courant-Friedrichs-Levy) restriction, leading to a computational cost proportional to $Re_{L_x}^{65/21}$ and $Re_{L_x}^{4/3}$ for WRLES and WMLES, respectively. While the total computational cost scaling of a WMLES suffers a slight change when considering the time-integration contribution compared to the Choi and Moin estimates (from $Re_{L_x}$ to $Re_{L_x}^{1.33}$), in a WRLES the scaling increases dramatically from approximately $Re_{L_x}^{1.85}$ to $Re_{L_x}^{3.09}$. These new expressions highlight even more the extreme difficulty of performing WRLES computations for industrial applications at relevant Reynolds numbers.

After reviewing the difficulties that arise when dealing with WRLES, it is clear that WMLES is a very promising strategy to make wall-bounded flow computations at high Reynolds number affordable. Several approaches have been developed to deal with the boundary layer complexity. All of them are based on modeling the inner layer (Tab. 1.1) in one way or the other instead of fully resolving it from a temporal and spatial point of view.

### 1.2.4 Hybrid RANS-LES

Hybrid RANS-LES methods were developed in response of the strong gap between RANS and LES turbulence models techniques in terms of both computational resources and numerical accuracy (Fig. 1.6). In this regard, hybrid RANS-LES models can be presented as a set of techniques, bridging from RANS-DNS, according to the industrial needs in conjuction with the available computational amenities. Quoting Chaouat [18],

"*It is opinion to the author to consider that the most appropriate method for a particular application will depend on the expectations of the engineer and the computational resources the user is prepared to expend on the problem*".

Despite the strong improvements presented by the computational resources during the last decades, pure LES simulations remain still unfeasible for general industrial applications (section 1.2.2). Considering that this prospect will not change significantly in the near future [4, 16], hybrid methodologies are presentend as a good alternative able to take advantadge from the current computational global scenario. Apart from providing significant quality improvements in comparison to RANS, this kind of methodologies are able to adapt their accuracy in response to the available computational amenities.

Hybrid RANS-LES strategies can be divided in two main categories, zonal and non-zonal. Zonal methods are based on applying two different models, RANS and LES, in different domains previously defined by the user. This division leads to a set of sharp interfaces boundaring the different domains and requiring special treatments, which not always ensure mass continuity. Instead, non-zonal methods naturally switch from RANS to LES (and viceversa) depending on the mesh capabilities and the flow topology. The latter approach, is of growing interest in hybrid RANS-LES modeling due to its user-friendly approach, as there is no need of defining neither RANS and LES zones by the user nor special interface treatments. A good and recent review which presents, assesses and also discusses the principal hybrid methods that are currently used for industrial applications can be found in Chaouat [18]. These are: *Very Large Eddy Simulation* (VLES) [19], *Detached Eddy Simulation* (DDES) [20], *Partially Integrated Transport Modeling* (PITM) [21, 22], *Partially Averaged Navier-Stokes* (PANS) [23]

and the *Scale Adaptive Simulation* (SAS) [24]. According to Friess et al. [25], some of these thechniques present a common background, such as PITM-PANS or PITM-DDES. It is worth noting that even though the theoretical foundation of PITM/PANS is considerably better than DDES, the latter approach has resulted in a very successful modification of a RANS model [26]. Actually, DDES is currently one of the most popular hybrid strategies for modelling strongly turbulent flows with the presence of bluff-bodies and/or massive flow separations. Despite their benefits, these models usually suffer from a slow RANS to LES transition (named *Grey Area*), resulting in unphysical delays of critical flow instabilities in sensitive regions, such as Kelvin-Helmholtz structures in free shear layers.

In this regard, the present thesis aims to perform a consistent study of different techniques for mitigating such delay in DDES models. A promising easy-to-apply new strategy for addressing this unphysical behaviour is also presented, discussed and tested with a set of well-known cases in the literature. The theoretical description of DDES, as well as their shortcomings and the proposed remedies are described in chapter 3. Accordingly, the assessment of such remedies can be found in chapter 4.

### 1.2.5 Direct Numerical Simulation (DNS)

As the name implies, DNS is a direct simulation of the NS equations, without any kind of modelization or experimental results (except for fluid physical properties). This concept could be applied for resolving any kind of PDE, but the degree of complexity of the NS equations is much higher, due to its multiscale behaviour. Strictly speaking, in a DNS the cascade process needs to be fully resolved, from the largest scales strongly conditioned by the geometry, to the dissipation scales featured by having a universal isotropic behaviour (section 1.1). For this purpose, care should be taken during the discretization of the NS equation, as the numerical schemes cannot act as an extra source of numerical difussion. This artificial diffusion contributes to the dissipation of the turbulent kinetic energy, seriously harming the kinetic energy transport between scales in the cascade process. Depending on the physics, such as compresible flows at high Mach values ($M \geq 1$), the use of numerical difussion is allowed for stability reasons due to the strong gradients in shock wave areas.

Apart from the importance of the numerical schemes, the resolution of the multiscale process is extremally expensive from a computational point of view. Its cost basically depends on the geometry size, the Reynolds value and also the presence of complex flow behaviour such in wall-bounded flows (almost any engineering application includes walls). Considering that the ratio between *integral scales* vs the *dissipation scales* (section 1.1.1) is around

$$\ell/\eta \sim Re_\ell^{3/4}, \tag{1.33}$$

the space scaling in a 3D geometry is around $Re_\ell^{9/4}$. Where $Re_\ell$ referes to the Reynolds value of the *integral scales*. Rergarding the time scale scaling, it can be estimated using the Courant condition leading to $\sim Re_\ell^{3/4}$ [27]. Hence, an optimist estimation of a DNS cost considering both space and time resolution is $Re_\ell^3$. Despite the breathtaking improvements presented by the computational resources during the last decades, this scaling factor remains a huge restriction for applying DNS in industrial applications, as usual operation conditions entails high Reynolds values.

## 1.3 Selection's Consequences

Obviously, if Computational Cost (CC) is filtered out from Fig. 1.6, those models with lower Degree of Modelling (DoM) will be preferable in any sector, including industry. In fact, the dream of any CFD application engineer would be to perform DNS in any situation, without worrying about the required DoM in each application (forgetting about RANS, Hybrid RANS-LES, WMLES and LES). It could actually happen if computational resources were not only free and unlimited but also able to provide results almost instantaneously. In a far future, this scenario cannot be discarded due to the strong rythm of growth of the computational resources (well-predicted by the Moore's law), as well as the emergence of new techonolgies such as cloud-based quantum computing [28]. In this regard, the present thesis is underspinned by the fact that quantum computing will not be broadly available during the next decades.

To come back to current realities, in industry a balance between CC and DoM needs to be found for each application (Fig. 1.6). In this section, a table containing the DoM and the associated CC of all techniques described in section 1.2 is shown. In addition, a canonical geometry with forced convection has been resolved using three different turbulence modelling strategies (RANS, Hybrid RANS-LES and DNS) in order to palpably show their implications (pros and cons).

### 1.3.1 Degree of Modelling (DoM)

A summarizing table 1.3.1 comprising all the methodologies discussed above is presented. It includes the range of applicability for each methodology as well as their CC and the strength of their physical assumptions, represented by the DoM [8]. In general, the stronger the assumptions, the lower the model generality and its ease of use. Increasing the DoM, usually entails that model coefficients and boundary conditions for some specific quantities must be provided and tuned to obtain correct flow prediction. Some of these specific quantities may range from turbulent kinetic energy to energy dissipation, and they may not be easily determined. On the other hand, although some models might be applicable for complex non-equilibrium conditions, a strong a priori flow knowledge is needed to adjust the model properly

and obtaining acceptable results. Additionally, the DoM is usually detrimental to the temporal and spatial resolutions, and therefore, much fewer details of the flow behavior can be obtained, especially for quantities related to the temporal behavior such as high frequency velocity fluctuations.

**Table 1.2:** Numerical strategies for Computational Fluid Dynamics classified according their Degree of Modeling (DoM) and Computational Cost (CC). Symbols legend: (Maximum) $\Uparrow \uparrow \nearrow \rightarrow \searrow \downarrow \Downarrow$ (Minimum). The table is split into methodologies suitable for free and wall-bounded flows [8].

**Free flows**

| Methodology | Applicabilty range | DOM | CC |
|---|---|---|---|
| DNS | Any flow condition | $\Downarrow$ | $\Uparrow$ |
| LES | Any flow condition | $\downarrow$ | $\uparrow$ |
| RANS/Unsteady-RANS | Limited-to-non-equilibrium flows | $\nearrow$ | $\rightarrow$ |

**Wall-bounded flows**

| Methodology | Wall treatment | Wall model | Applicability range | DOM | CC |
|---|---|---|---|---|---|
| DNS | N/A | N/A | Any flow condition | $\Downarrow$ | $\Uparrow$ |
| WRLES | N/A | N/A | Any flow condition | $\downarrow$ | $\uparrow$ |
| WMLES | Wall shear stress | Unsteady-RANS-based TLM | Non-equilibrium flows<br>Detached boundary layer | $\searrow$ | $\nearrow$ |
| | | wall functions | Equilibrium flows<br>Attached boundary layer | $\nearrow$ | $\downarrow$ |
| Hybrid-RANS/LES | N/A | N/A | Non-equilibrium flows<br>Detached boundary layer | $\rightarrow$ | $\rightarrow$ |
| RANS/Unsteady-RANS | N/A | N/A | Limited non-equilibrium flows<br>Attached boundary layer | $\nearrow$ | $\searrow$ |
| | Wall shear stress | wall functions | Limited non-equilibrium flows<br>Attached boundary layer | $\uparrow$ | $\downarrow$ |

## 1.3.2 Example

This section aims to alert what selecting a turbulence model entails. For this purpose, an incompressible flow through a Backward-Facing Step (BFS) configuration is simulated using different modelling strategies. In this part of the thesis, we are more interested in showing the turbulence model implications, rather than the interesting physical insights of the BFS case. Chapter 2 is completely dedicated to this end. Hence, the simulation set-up and the case geometry (Fig. 2.1) can be found in section 2.2. Three different turbulence modelling strategies have been considered. These are: *Spalart-Allmaras* (RANS-SA), one of the most widely used *RANS* techniques; *DDES-SA*, an *hybrid RANS-LES* approach broadly used in industry; *DNS*, extremly costly and accuracte simulation.

**Table 1.3:** CC comparison of different turbulence modelling approaches in a Backward-Facing Step (BFS) geometry. A cost of core per hour equal to 0.02 € has been considered.

| Turbulence Model | Computational Cost (CC) | | | | |
|---|---|---|---|---|---|
| | **Mesh [cells]** | **Integration Time [tu]** | **CPUs [core]** | **Simulation Time [hours]** | **Cost [€]** |
| *RANS-SA* | $12 \cdot 10^3$ | - | 1 | 0.5 | 0.01 |
| *DDES-SA* | $70010^3$ | 40 | 6 | 58 | 7 |
| *DNS* | $173 \cdot 10^6$ | 200 | 1536 | 336 | 10000 |

In terms of cost, the impact of choosing a particular turbulence models can be easily seen in Table 1.3. Even though it is not a rigorous study, as those simulations were carried out using different machines, it helps realize how pronounced the differences between turbulence strategies are. For instance, performing the *RANS* simulation is around 700 times cheaper than a *DDES-SA* and $10^6$ times respect to the DNS. In the case of DNS, these differences are caused by the fact that this strategy needs to recreate all turbulence scales in space and time, entailing extremelly fine meshes and small time steps. In contrast, RANS simulations model the entire effect of the kinetic energy cascade into the mean flow. For this reason, 3D meshes are no longer needed for resolving such phenomenon in the BFS case. This fact has significant implications in terms of both space and time resolution, as coarser meshes and higher time steps are allowed. Moreover RANS simulations usually achieve a steady state, so the Integration Time (Tab. 1.3) is also saved. Hence, in those cases where RANS is a reliable option, the cost of creating the mesh and engineers' salary (among others) are significantly higher than running the CFD simulation. In contrast, this is not necessarily true for DNS as the CC required by this strategy is around $10^6$ times higher than RANS. Finally, even though the DDES-SA model is considerably more expensive than RANS, it is currently a feasible option for those cases where RANS becomes unreliable. It is also recommendable for obtaining high quality transient data (if it is required), in contrast to the Unsteady-RANS. The DDES-SA cost increasement respect to RANS is because of the need of having 3D meshes in the LES region in order to partially resolve the kinetic energy cascade. It directly leads to a time step reduction for capturing the smallest scales allowed by the mesh. Moreover, the inherent transient behaviour of the Hybrid RANS-LES simulation makes necessary the use of an Integration Time (Tab. 1.3) for assessing the average statistics.

The huge CC discrepancies among modelling strategies have a direct impact in the quality of the final solution, as the DoM of each technique is also significantlly differ-

ent. It can be conceptually appreciated in Fig. 1.7, where the instantaneous pressure gradient magnitude of the selected models is shown. Pressure gradient magnitude is a well-known scalar for detecting the flow instabilities in a shear layer [10, 29]. RANS simulation (top) only shows an important pressure gradient magnitude at the step-edge (just downstream of the sudden expansion), but there is no evidence of instabilities in this area. It makes sense, as the diffusion (high DoM) inserted by the model kills any transient effect, such as the instability triggering at the free shear layer (sec. 1.1.1). Moreover, the mesh used for carrying out this simulation was 2D, erasing any possibility of having a 3D flow behaviour (good practice in RANS modelling). All this leads to achieving a steady-state instead of a transient signal, so in the pressure gradient magnitude in Fig. 1.7 (top) there is not trace of flow instabilities. In contrast to the steady state behaviour observed in a RANS simulation, the Hybrid RANS-LES model ($DDES - SA$, middle) switches from RANS to LES at the step-edge, triggering the flow instabilities downstream of the sudden expansion. It is worth noting, that this figure has not been obtained using the standard $DDES - SA$, but including the modifications proposed in the present thesis. Otherwise, the triggering would not be so pronounced. The $RANS$ behaviour of the Hybrid RANS-LES model can also be observed upstream of the step-edge and downstream at the upperwall. Finally, an image of the DNS (without DoM) is presented in Fig. 1.7 (bottom), where a fully-turbulent flow is observed, recreating all the physical phenomena mentioned in section 1.1.1. These are: the entire cascade energy process from the integral to the Kolmogorov scales, the turbulence triggered in the wall bounded flows and also the Kelvin-Helmholtz instabilities at the free shear layer.

## 1.4 Conclusions

This chapter provides a general overview of turbulence, from a physical and mathematical point of views. The different numerical approaches for modelling turbulence are also introduced. The implications of the turbulence model selection is discussed using a practical example, showing up its huge impact in both computational resources and degree of modelling. In fact, the previous section concludes that, even though DNS is the most accurate technique (lowest DoM), is also the most expensive one (check CC in Tab. 1.3). It makes DNS a technique only feasible for scientific applications. The same can be applied to LES when there are walls involved in the simulated domain. If we add that RANS becomes unreliable for certain applications, and the good rate of growth of the computational resources during the last years, it seems that Hybrid RANS-LES models will be the next main technique to be adopted by the industrial sector (shifting the RANS predominance).

Within the family of hybrid models, Delayed-Detached Eddy Simulation (DDES) outstands due to its user-friendly non-zonal approach and its proved success in

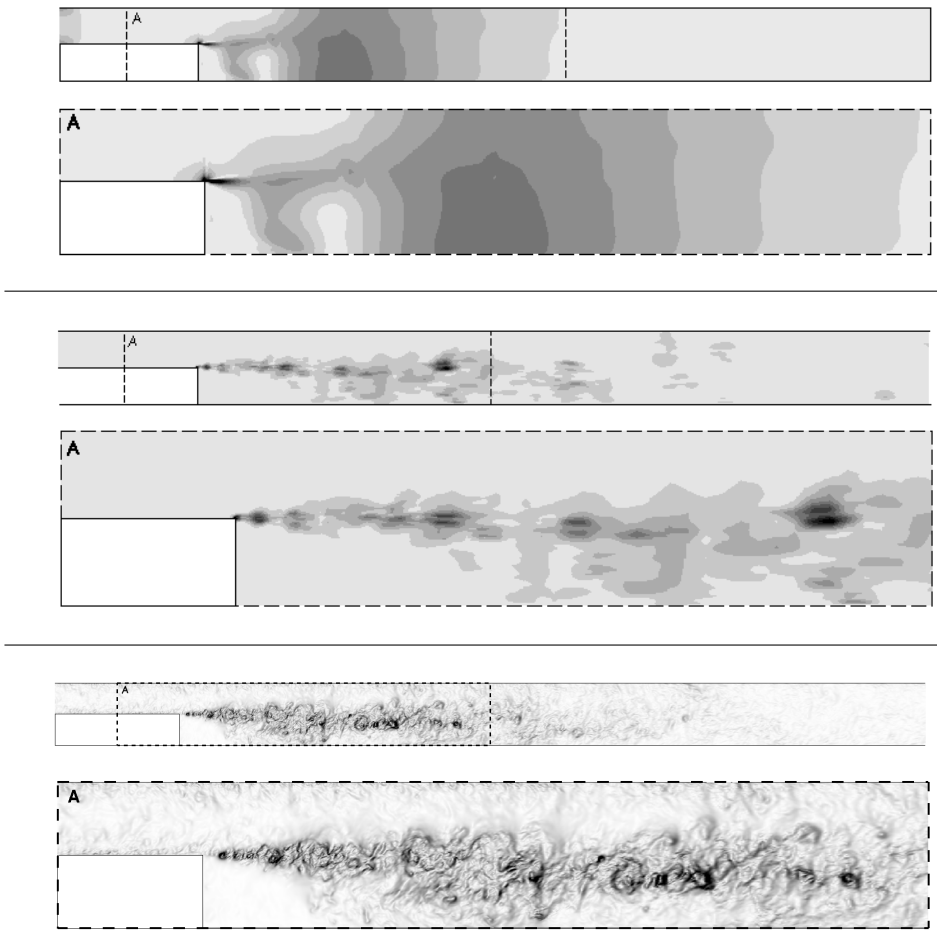


**Figure 1.7:** Instantaneous pressure gradient magnitude of a BFS at $Re_\tau = 395$ and $ER = 2$, using the following modelization strategies: (top) $RANS - SA$, (middle) $DDES - SA$ and (top) $DNS$. Black denotes strong values, but all figure use different scalings for visualization purposes. CC is shown in Table 1.3.

several applications. Despite their benefits, these models usually suffer from a slow RANS to LES transition (named *Grey Area*), resulting in unphysical delays of critical flow instabilities in sensitive regions, such as Kelvin-Helmholtz structures in free shear layers. In this regard, the present thesis aims to perform a consistent study of different techniques for mitigating such a delay, as well as presenting a promising easy-to-apply new strategy (third chapter). However, due to the lack of publicly available highly reliable data set, a Direct Numerical Simulation (DNS) of a Backward-Facing Step (BFS) at $Re_\tau = 395$ and expansion ratio (ER) 2 has been carried out during the first part of this thesis for comparison purposes. This work is presented in chapter two. In contrast to the rest of experimental reference cases, it provides a detailed view of the triggering and feeding processes of the flow instabilities through the free shear layer.

# References

[1] L. F. Richardson. *Weather Prediction by Numerical Process*. Cambridge University Press, 1972.

[2] J. M. McDonough. *Introductory Lectures on Turbulence*. 2007.

[3] J. Schumacher, J. D. Scheel, D. Krasnov, D. A. Donzis, V. Yakhot, and K. R. Sreenivasan. Small-scale universality in fluid turbulence. *Proceedings of the National Academy of Sciences*, 111(30):10961–10965, 2014.

[4] S. B. Pope. *Turbulent flows*. Cambridge University Press, 2000.

[5] S. Hoyas and Jimenez J. Scaling of the velocity flutuations in turbuup to up to $Re_\tau = 2003$. *Physics of Fluids*, 18, 2006.

[6] Sillero J. A., Jimenez J., and Moser R. D. One-point statistics for turbulent wall-bounded flows at Reynolds numbers up to $\delta^+ \sim 2000$. *Physics of Fluids*, 25, 2013.

[7] J. Lee J. H. Kang J. Ahn, J. H. Lee and H. J. Sung. Direct numerical simulation of a 30R long turbulent pipe flow at $Re_\tau = 3008$. *Physics of Fluids*, 27, 2015.

[8] J. Calafell. *Efficient Wall Modeling for Large Eddy Simulations of General Non-Equilibrium Wall-Bounded Flows.* PhD thesis, 2019.

[9] J. Jimenez. *Free Shear Flows*. Universidad Politecnica de Madrid, 2013.

[10] A. Pont-Vílchez, F. X. Trias, A. Gorobets, and A. Oliva. Direct numerical simulation of backward-facing step flow at $re_\tau = 395$ and expansion ratio 2. *Journal of Fluid Mechanics*, 863:341–363, 2019.

[11] J. Delville, S. Bellin, J. H. Garem, and J. P. Bonnet. Analysis of structures in a turbulent, plane mixing layer by use of a pseudo flow visualization method based on hot-wire anemometry. In Hans-Hermann Fernholz and Heinrich E. Fiedler, editors, *Advances in Turbulence 2*, pages 251–256, Berlin, Heidelberg, 1989. Springer Berlin Heidelberg.

[12] P Bradshaw. The understanding and prediction of turbulent flow. *Aeronautical Journal*, pages 403–418, 1972.

[13] Claudio Canuto, M. Yousuff Hussaini, Alfio Quarteroni, Thomas A., and Zan Jr. Springer, 1988.

[14] P. Sagaut. *Large Eddy Simulation for Incompressible Flows: An Introduction*. Springer, third edition, 2005.

[15] D. R. Chapman and G. D. Kuhn. The limiting behaviour of turbulence near a wall. *Journal of Fluid Mechanics*, 170:265–292, 1986.

[16] Haecheon Choi and Parviz Moin. Grid-point requirements for large eddy simulation: Chapman's estimates revisited. *Physics of Fluids*, 24(1):011702, 2012.

[17] J. Calafell, F.X. Trias, O. Lehmkuhl, and A. Oliva. A time-average filtering technique to improve the efficiency of two-layer wall models for large eddy simulation in complex geometries. *Computers Fluids*, 2019.

[18] Bruno Chaouat. The State of the Art of Hybrid RANS/LES Modeling for the Simulation of Turbulent Flows. *Flow, Turbulence and Combustion*, 99(2):279–327, 2017.

[19] C. Speziale. Turbulence Modeling for Time-Dependent RANS and VLES: A Review. *AIAA Journal*, 36(2):173–184, feb 1998.

[20] P. R. Spalart, S. Deck, M. L. Shur, K. D. Squires, M. Kh Strelets, and A. Travin. A new version of detached-eddy simulation, resistant to ambiguous grid densities. *Theoretical and Computational Fluid Dynamics*, 20(3):181–195, 2006.

[21] Roland Schiestel and Anne Dejoan. Towards a new partially integrated transport model for coarse grid and unsteady turbulent flow simulations. *Theoretical and Computational Fluid Dynamics*, 18(6):443–468, feb 2005.

[22] Bruno Chaouat and Roland Schiestel. A new partially integrated transport model for subgrid-scale stresses and dissipation rate for turbulent developing flows. *Physics of Fluids*, 17(6):065106, jun 2005.

[23] Sharath S. Girimaji, Ravi Srinivasan, and Euhwan Jeong. PANS Turbulence Model for Seamless Transition Between RANS and LES: Fixed-Point Analysis and Preliminary Results. In *Volume 2: Symposia, Parts A, B, and C*, pages 1901–1909. ASME, jan 2003.

[24] F. R. Menter and Y. Egorov. The Scale-Adaptive Simulation Method for Unsteady Turbulent Flow Predictions. Part 1: Theory and Model Description. *Flow, Turbulence and Combustion*, 85(1):113–138, jul 2010.

[25] Ch Friess, R. Manceau, and T. B. Gatski. Toward an equivalence criterion for Hybrid RANS/LES methods. *Computers and Fluids*, 122:233–246, 2015.

[26] L Davidson, C Friess, Aix-marseille Universit, Centrale Marseille, and M P Umr. The PANS and PITM model : a new formulation of f k. pages 1–6, 2018.

[27] Uriel Frisch. *Turbulence: The Legacy of A. N. Kolmogorov*. Cambridge University Press, nov 1995.

[28] Aram W. Harrow, Avinatan Hassidim, and Seth Lloyd. Quantum algorithm for linear systems of equations. *Phys. Rev. Lett.*, 103:150502, Oct 2009.

[29] F. X. Trias, A. Gorobets, and A. Oliva. Turbulent flow around a square cylinder at Reynolds number 22,000: A DNS study. *Computers and Fluids*, 123(22):87–98, 2015.

# 2

# Direct Numerical Simulation of Backward-Facing Step flow

Main contents of this chapter have been published in:

A. Pont-Vílchez, F.X. Trias, A. Gorobets, and A. Oliva. Direct Numerical Simulation of Backward-Facing Step flow at $Re_\tau = 395$ and expansion ratio 2. *Journal of Fluid Mechanics*, 863:341–363, 2019.

**Abstract.** Backward-Facing Step (BFS) constitutes a canonical configuration to study wall-bounded flows subject to massive expansions produced by abrupt changes in geometry. Recirculation flow regions are common in this type of flows, driving the separated flow to its downstream reattachment. Consequently, strong adverse pressure gradients rise through this process which feeds flow instabilities. Therefore, both phenomena are strongly correlated as the recirculation bubble shape defines how the flow is expanded, and how the pressure rises. In an incompressible flow, this shape depends on the Reynolds value and the expansion ratio. The influence of these two variables on the bubble length is widely studied, presenting an asymptotic behaviour when both parameters are beyond a certain threshold. This is the usual operating point of many practical applications, such as in aeronautical and environmental engineering. Several numerical and experimental studies have been carried out

regarding this topic. The existing simulations considering cases beyond the above-mentioned threshold have only been achieved through turbulence modelling, whereas Direct Numerical Simulations (DNS) have been performed only at low Reynolds numbers. Hence, despite the great importance of this phenomenon, there is a lack of reliable numerical data to assess the accuracy of turbulence models. In this context, a DNS of an incompressible flow over a BFS is presented in this chapter, considering a $Re_\tau = 395$ at the inflow and an expansion ratio 2. Finally, the elongation of the Kelvin-Helmholtz instabilities along the shear layer is also studied.

## 2.1 Introduction

Sudden massive expansions are common in many engineering applications: from internal flows in heat exchangers and combustors to external flows, such as vehicle aerodynamics. Usually, the separation and reattachment process yield to dramatic drag rises, as well as reductions of the pressure growth and heat transfer rate. Even so, the shear layer can also be beneficial in some industrial applications, triggering turbulence transition and enhancing the mixing rate of chemical species.

In this regard, the Backward-Facing Step (BFS) represents a canonical configuration to study this kind of wall-bounded fluids (see figure 2.1). This case consists of two channel flows connected by a sharp step of height $h$. Both channels share the same aspect ratio ($AR = L_z/h$), whereas the difference between the channel heights is defined by the expansion ratio, $ER = H/(H-h)$. Where $L_z$ and $H$ represent the BFS span-wise length and the outlet channel height, respectively. The flow in a BFS is massively separated due to the sudden expansion, but reattached downstream of the channel. The abrupt separation leads to a shear layer which feeds a recirculation bubble attached to the step. This bubble governs the flow progressive expansion downstream of the step-edge, as well as the way the pressure grows along the channel (reattachment process). At low Reynolds numbers, the shear layer and the recirculation bubble represents a stable system, as the kinetic energy transferred by the shear layer into the recirculation zone is well dissipated because of the friction forces. However, when the Reynolds is high enough, the viscous forces cannot dissipate all the kinetic energy provided by the shear layer. Thus, the system becomes unstable. Therefore, the inertial forces tend to flap the shear layer, becoming a source of the well-known Kelvin-Helmholtz instabilities ($KH$). Finally, these instabilities are fed, paired and elongated along the shear layer, until they impinge at the lower wall, contributing to the recirculation bubble detachment. Needless to say, the inflow and wall effects also play an important role in all this process.

In addition to its engineering interest, the simplicity of the BFS geometry makes it a suitable case to study the above explained complex phenomena by means of both, experimental and numerical analysis. The vast majority of the experimental

studies such as Eaton & Johnston [1], Armaly et al. [2], Driver & Seegmiller [3], Kasagi & Matsunaga [4] and Jovic & Driver [5] were focused on the measurement of the reattachment length ($X_r$) depending on a single configuration of Reynolds number and $ER$. By contrast, there were only a few researchers such as Kuehn [6], Durst & Tropea [7] and Ötügen [8] who studied the $ER$ effects on $X_r$, using late transitional or turbulent boundary layers at separation. Recently, Nadge & Govardhan [9] carried out a complete set of parametric studies analyzing the influence of the Reynolds number and the $ER$ on the $X_r$. Besides reducing the huge data scattering observed in previous studies, the authors also provided results showing the aysmptotic behaviour of the $X_r$ beyond a certain threshold. It should be noticed here that almost all the experimental works mentioned above followed the Brederode & Bradshaw [10] recommendation to avoid the sidewall effects ($AR > 10$).

Apart from the large amount of experimental research dedicated during the last decades, numerical simulations are also quite numerous. First studies, i.e. Speziale & Ngo [11], Thangam & Speziale [12] and Lasher & Taulbee [13], were focused on on RANS in order to test and improve the existing models. Once the computational resources became more available to the scientific community, less case-dependent methodologies such as LES and other hybrid RANS-LES models were studied. In particular, the Detached Eddy Simulation (DES) family models presented by Spalart et al. [14] in the late 90s were designed to simulate massively separated flows such as BFS, airfoils at stall and jets. Since then, several authors such as Spalart et al. [15], Shur et al. [16] and Gritskevich et al. [17] focused their efforts on addressing the main two DES shortcomings, which are: the shielding of the RANS boundary layers against any unwanted incursion of the LES formulation and the delay of the $KH$ instabilities produced during the RANS to LES transition (Mockett et al. [18]). In this context, the selected BFS configuration ($ER = 2$) presents a challenging configuration where both problematic areas coexist in the same case (DES simulation). In particular, the flow structures ($KH$ instabilities) created at the shear layer (LES area) incur into the upper wall, damaging the flow behaviour at the boundary layer (RANS area). It is worthwile pointing out that this phenomenon is negligible if the distance between the LES and RANS area is large enough (low $ER$ value).

In spite of the numerous numerical studies using turbulence models, there has been very little research in the BFS area using DNS so far. This fact is mainly due to the computational resources that this sort of simulations require. First DNS of a fully turbulent BFS was not carried out until late 90s, when Le et al. [19] simulated a BFS at $Re_b \sim 4250$ and $ER = 1.2$. Where $Re_b$ is defined using the step height, $h$, and the inlet bulk velocity, $U_b$. The authors performed a complete analysis and demonstrated that the log-profile downstream of the channel flow was not fully recovered even $19h$ after the reattachment. Their results presented a good agreement with the experiments carried out by Jovic & Driver [5]. Afterwards, other researchers such as Biswas et

al. [20] and Schäfer et al. [21] performed DNS to study the BFS flow transition from laminar to turbulent. Both authors used low Reynolds values and laminar velocity profiles at the inflow. The first author studied a range of small Reynolds numbers, $Re_b \in [5 \cdot 10^{-5}, 400]$, and expansion ratios, $ER \in [1.9423, 3]$, to detect the transition value in which the turbulence emerges. Otherwise, the second one was focused on the structures created at the step-edge of a BFS in a single flow configuration at a higher Reynolds number ($Re_b = 3000$) and $ER = 1.9423$. This author also studied how those structures were related to the $X_r$ oscillations. However, few authors carried out research at higher Reynolds numbers and using turbulent inflows, such as Meri & Wengle [22] and Barri et al. [23]. The former studied the effect of $2^{nd}$ and $4^{th}$ order spatial discretization schemes at $Re_b = 3300$ and a $ER = 1.5$, while the latter used a $Re_b = 5600$ and $ER = 2$ by testing its turbulent inflow boundary condition in a configuration with a non-homogeneous stream-wise direction. This turbulent inflow was previously tested in a channel flow by Barri et al. [24] showing a good performance. Although these authors considered different parameters in their simulations, both used the same channel flow configuration at the entrance, $Re_\tau = 180$ (based on the wall skin friction velocity, $u_\tau$, and the half height of the plane). This is a well-known and widely studied turbulent channel flow, but the low-Reynolds effects are still present. Currently, there is still a lack of numerical data reporting BFS flow behaviour at higher Reynolds numbers, where the low-Reynolds effects are diminished. Moreover, all DNSs carried out so far are significantly away from reaching the $X_r$ asymptotic behaviour.

In this chapter, a DNS of an incompressible fluid flow over a BFS with an $ER = 2$ has been performed using a turbulent channel flow at $Re_\tau = 395$ as an inlet condition. Besides being close to reaching an $X_r$ asymptotic behaviour, the studied case is also interesting for understanding how a classical turbulent channel flow is expanded under certain conditions. Regarding the inflow boundary condition, there are two main approaches in order to address this issue. Inflow data can either be generated by previously running a channel flow simulation ( as Meri & Wengle [22] investigated), and saving the velocity field in a stream-wise plane or using turbulent synthetic algorithms. The former is used in this chapter as it is suitable for performing a DNS. Finally, it is worth noting here that besides giving insights into the physics of turbulent flows after massive separations, the aim of this work consists of providing reference data (Pont-Vílchez et al. [25]) for this canonical configuration, and not to reproduce any particular experimental set-up.

The rest of the chapter is arranged as follows. In the next section, the governing equations and the problem definition are described together with an overview of the numerical methods. The methodology to verify the simulation is presented in Section 2.3. The core of the results is in Section 4.4. Firstly, the main features of the time-averaged flow are discussed on a basis of a direct comparison with

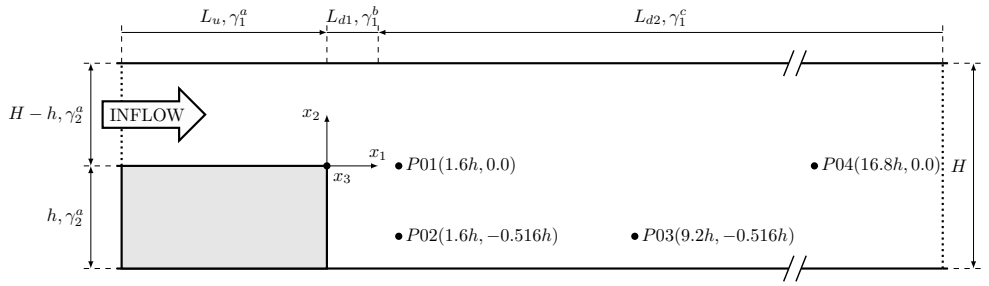


**Figure 2.1:** Schematic figure of the Backward Facing Step problem, $ER = H/(H - h) = 2$, and details about its geometry and grid spacing (size of zones and concentration factors; arrows indicate the grid refinement direction). Not to scale.

previous experimental results. Reynolds stress transport terms are also presented and commented in this section. The discussion focuses on the flow dynamics, observing the $KH$ instabilities and presenting the kinetic energy spectrum cascade at different flow locations: in the shear layer, recirculation bubble, reattachment and recovery regions. The rate of growth of the $KH$ instabilities along the shear layer and their elongation due to the vortex pairing phenomenon are also studied and compared with experimental observations [26, 27]. Finally, the most significant results are summarized and conclusions are given in the last section.

## 2.2 Governing equations and numerical methods

The incompressible Navier-Stokes (NS) equations in primitive variables are considered

$$\partial_t u_i + u_j \partial_j u_i = -\partial_i p + \nu \partial_j^2 u_i; \qquad \partial_i u_i = 0, \tag{2.1}$$

where $u_i$ is the velocity field, $p$ represents the kinematic pressure, and $\nu$ is the kinematic viscosity. A schema of the problem under consideration is shown in figure 2.1.

The dimensions of the computational domain are $38h \times 2h \times 2\pi h$ in the streamwise, normal and span-wise direction, respectively. The sudden expansion is located at $L_u = 6h$ from the inflow, whereas the domain length downstream of the step is divided into two parts ($L_{d1} = 1h, L_{d2} = 31h$) because of refinement reasons. The origin of coordinates is placed at the expansion sharp edge. A detailed discussion about the determination of the domain size and grid spacing is given in the next section.

Regarding the boundary conditions, a turbulent channel flow is imposed at the inflow following the same strategy used by Meri & Wengle [22], whereas a convective boundary condition is used at the outflow, $\partial_t u_i + 0.5 U_b \partial_1 u_i = 0$. Global mass conservation may be not exactly preserved after imposing such boundary conditions. It is forced by means of a minor correction (a constant many orders of magnitude lower than $U_b$) at the outflow conditions. Finally, periodic boundary conditions are imposed in the span-wise direction, and no-slip boundary conditions are imposed at the walls.

The incompressible NS equations (2.1) are discretized on a non-uniform structured staggered mesh, and a $4^{th}$ order symmetry-preserving discretization [28] scheme is used. Shortly, the temporal evolution of the spatially discrete staggered velocity vector, $\mathbf{u}_s$, is governed by the following operator-based finite-volume discretization of Eqs.(2.1),

$$\mathbf{\Omega} \frac{d\mathbf{u}_s}{dt} + \mathbf{C}\left(\mathbf{u}_s\right)\mathbf{u}_s + \mathbf{D}\mathbf{u}_s - \mathbf{M}^T \mathbf{p}_c = \mathbf{0}_s, \tag{2.2}$$

where the subscript $s, c$ refers to discrete staggered and collocated vectors, respectively. The discrete incompressibility constraint is given by $\mathbf{M}\mathbf{u}_s = \mathbf{0}_h$, where $\mathbf{M}$ indicates the divergence matrix. The diffusive matrix, $\mathbf{D}$, is symmetric and positive semi-definite, representing the integral of the diffusive flux, $-\nu \partial_j u_i n_j$, through the faces (where $n_j$ refers to a normal surface direction). The diagonal matrix, $\mathbf{\Omega}$, describes the sizes of the control volumes and the approximate, convective flux is discretized as in Verstappen & Veldman [28]. The resulting convective matrix, $\mathbf{C}\left(\mathbf{u}_s\right)$, is skew-symmetric, *i.e.*

$$\mathbf{C}\left(\mathbf{u}_s\right) = -\mathbf{C}^T\left(\mathbf{u}_s\right). \tag{2.3}$$

In a discrete setting, the skew-symmetry of $\mathbf{C}\left(\mathbf{u}_s\right)$ implies that

$$\mathbf{C}\left(\mathbf{u}_s\right)\mathbf{v}_s \cdot \mathbf{w}_s = \mathbf{v}_s \cdot \mathbf{C}^T\left(\mathbf{u}_s\right)\mathbf{w}_s = -\mathbf{v}_s \cdot \mathbf{C}\left(\mathbf{u}_s\right)\mathbf{w}_s, \tag{2.4}$$

for any discrete velocity vector $\mathbf{u}_s$ (if $\mathbf{M}\mathbf{u}_s = \mathbf{0}_s$), $\mathbf{v}_s$ and $\mathbf{w}_s$. The evolution of the discrete energy, $\|\mathbf{u}_s\|^2 = \mathbf{u}_s \cdot \mathbf{\Omega}\mathbf{u}_s$, is governed by

$$\frac{d}{dt}\|\mathbf{u}_s\|^2 = -2\mathbf{u}_s \cdot \mathbf{D}\mathbf{u}_s < 0, \tag{2.5}$$

where the convective and pressure gradient contributions cancel because of Eq.(2.3) and the incompressibility constraint, $\mathbf{M}\mathbf{u}_s = \mathbf{0}_c$, respectively. Therefore, even for coarse grids, the energy of the resolved scales of motion is convected in a stable manner, *i.e.* the discrete convective operator transports energy from a resolved scale of motion to other resolved scales without dissipating any energy, as it should be from a physical point-of-view. For a detailed explanation, the reader is referred to Verstappen & Veldman [28].

The governing equations are integrated in time using a classical fractional step projection method [29]. Namely, the solution of the unsteady Navier-Stokes equations is obtained by first time-advancing the velocity field, $\mathbf{u}_s^n$, without regard for its solenoidality constraint, then recovering the proper solenoidal velocity field, $\mathbf{u}_s^{n+1}$ ($\mathbf{M}\mathbf{u}_s = \mathbf{0}_c$). For the temporal discretization, a $2^{nd}$ order fully explicit one-leg scheme is used for both the convective and diffusive terms [30]. Thus, the resulting fully-discretized problem reads

$$\frac{(\kappa + 1/2)\,\mathbf{u}_s^p - 2\kappa\mathbf{u}_s^n + (\kappa - 1/2)\,\mathbf{u}_s^{n-1}}{\Delta t} = \mathbf{R}\left((1+\kappa)\,\mathbf{u}_s^n - \kappa\mathbf{u}_s^{n-1}\right), \tag{2.6}$$

where $\mathbf{R}(\mathbf{u}_s) = -\mathbf{C}(\mathbf{u}_s)\,\mathbf{u}_s - \mathbf{D}\mathbf{u}_s$ and $\mathbf{u}_s^p$ is a predictor velocity that can be directly evaluated from the previous expression. The time-integration parameter, $\kappa$, is computed to adapt the linear stability domain of the time-integration scheme to the instantaneous flow conditions in order to use the maximum time-step possible. For further details about the time-integration method the reader is referred to Trias & Lehmkuhl [30]. Finally, $\mathbf{u}_s^p$ must be projected onto a divergence-free space,

$$\mathbf{u}_s^{n+1} = \mathbf{u}_s^p + \mathbf{\Omega}^{-1}\mathbf{M}^T\tilde{\mathbf{p}}_c^{n+1}, \tag{2.7}$$

by adding the gradient of the pseudo-pressure, $\tilde{\mathbf{p}}_c = \Delta t/(\kappa + 1/2)\mathbf{p}_c$, satisfying the following Poisson equation

$$\mathbf{L}\tilde{\mathbf{p}}_c^{n+1} = \mathbf{M}\mathbf{u}_s^p \qquad \text{with} \qquad \mathbf{L} = -\mathbf{M}\mathbf{\Omega}^{-1}\mathbf{M}^T, \tag{2.8}$$

where the discrete Laplacian operator, $\mathbf{L}$, is represented by a symmetric negative semi-definite matrix. For details about the numerical algorithms and the parallel Poisson solver, the reader is referred to Gorobets et al. [31]. Notice that the pressure is not considered in the prediction step (2.6). On staggered grids with prescribed velocity boundary conditions, as in this case, the incompressibility condition occurs naturally and no specific boundary condition for the discrete pressure field, $\mathbf{p}_c$, needs to be specified, as pointed out in Kim & Moin [32]. Nevertheless, Neumann boundary conditions are prescribed for $\mathbf{p}_c$. Regarding the verification of the code, the reader is referred, for example, to Trias et al. [33]. The verification process of the DNS simulation carried out in this work is addressed in the next section.

## 2.3 Verification of the simulation

Averages over the two statistically invariant transformations (time and $x_3$-direction) are carried out for all the fields. The standard notation $\langle\cdot\rangle$ is used to denote this averaging procedure.

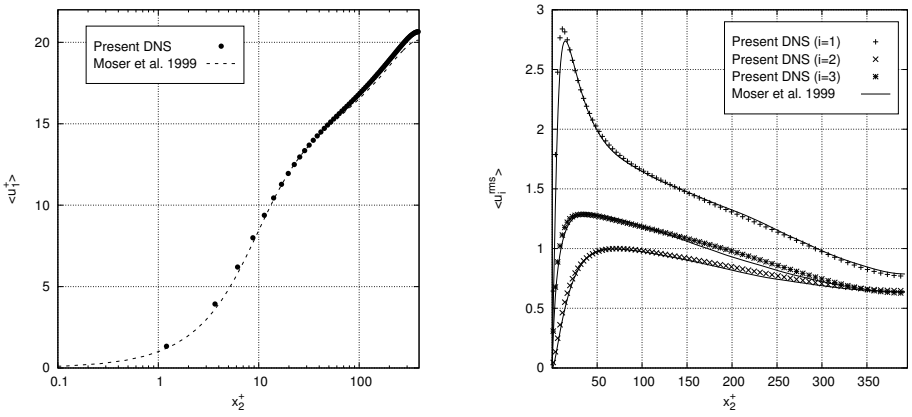


**Figure 2.2:** Log-Law (left) and Root-Mean-Square (right) profiles at $-5h$ over the step ($1h$ downstream of the inflow). Moser et al. [34] results are used as benchmark data.

During this section, the DNS results are verified using well-known tests in the literature. They are mainly focused on BFS, but the inflow quality is firstly discussed. As was mentioned before, the inflow data is obtained from a previous channel flow simulation at $Re_\tau = 395$. The signal is preprocessed before being used by the BFS. A linear spatial interpolation is applied as a slightly coarser mesh is used in the BFS case because of computational cost reasons. The quality of the preprocessed inflow is assessed in figure 2.2, where the log-velocity (left) and the root mean square (right) profiles $(rms)$ at a certain cross-section $(-5h)$ over the step are presented. They show a good agreement with the benchmark case [34]. A short distance from the inflow is selected $(6h - 5h = h)$ to demonstrate that there is no need of recovery region when this method is applied.

Once the behaviour of turbulence at the entrance is assessed, the minimum time integration period is determined. It has been achieved evaluating the normalized infinite norm of the $1^{st}$, $2^{nd}$ and $3^{rd}$ order tensors turbulent statistic values at each time step (Eq. 2.9).

$$||A||_{o,\infty}(t_s) = \max_{n}^{N} \left| 1 - \frac{1}{\langle a_{o,n} \rangle} \int_0^{t_s} a_{o,n} dt \right| \tag{2.9}$$

Where $[a_o]$ denotes a list of $N$ elements, which depends on the order $(o)$, and $n$ refers to a specific list element, $a_{o,n}$. The symbology $[\cdot]$ converts whatever tensor in a list of elements. Elements presenting average values, $\langle a_{o,n} \rangle$, close to zero are excluded in order to avoid $0/0$ indeterminate forms. The maximum absolute value in a list

of $N$ elements is selected at each $t_s$ and denoted as $||A||_{o,\infty}(t_s)$. For instance, $1^{st}$ order list ($N = 3$) is filled by all velocity components ($[a_1] = [u_i]$), whereas the $2^{nd}$ order list ($N = 9$) includes all $2^{nd}$ order tensor elements ($[a_2] = [u_i u_j]$). The same explanation is valid for the $3^{rd}$ order list. A set of probes has been distributed along the domain, but only the most important ones are shown in figures 2.1 and 2.3. The largest integration period is required at $P04$, where large structures dragged from the recirculation region are present. Similar behaviour is observed in the shear layer region, $P01$, where high velocity fluctuations also appear. The rest of probes are located between the two recirculation bubbles, $P02$, and in the reattachment region, $P03$. A schematic view of the probes location can be observed in figure 2.1. In contrast to the 280 average integration time units $(h/u_\tau)$ suggested by Barri et al. [23], figure 2.3 shows that $180h/u_\tau$ provides satisfactory results. This simulation time reduction can be attributed to the fact that different time integration techniques are applied. A set of individual quasi-independent flow fields separated by $0.25h/u_\tau$ were taken into account by Barri et al. [23], whereas a continuous integration along time is used in the present chapter. Apart from that, other factors such as the $Re_\tau$ could also affect the integration time period. From here on, all time-average results presented in this chapter have been obtained using $180h/u_\tau$, around 55 flow units ($t_f$=$(L_u + L_d ER)/U_b$).

The BFS geometry in the span and stream-wise directions is also studied because of its influence in the fluid behaviour. The capability of the span-wise length to reproduce the larger scales is assessed through two-point correlations, $B_i^{norm}(x_3 = 0, \hat{x}_3) = B_i^{norm}(\hat{x}_3)$, in the locations shown in figure 2.1.

$$B_i^{norm}(x_j, \hat{x}_j) = \frac{\langle u_i'(x_j) u_i'(x_j + \hat{x}_j) \rangle}{\langle u_i'(x_j) \rangle \langle u_i'(x_j + \hat{x}_j) \rangle} \tag{2.10}$$

All velocity components present correlations no longer than the periodic half-length (see figure 2.4). Thus, the periodic direction requirement is satisfied. The largest structures appear in the recirculation bubble ($P02$), where fluid becomes quasi-laminar, and the recovery region ($P04$). Furthermore, the stream-wise length is also examined as some experimental works, such as Nadge & Govardhan [9], reported a systematic increase of the $X_r$ and the recovery region under the step when the $Re$ was increased. In particular, Nadge demonstrated that this trend exists up to $Re_b \approx 16300$. Beyond this threshold, the $X_r$ only depends on the $ER$. In the present chapter, and despite the recirculation length increasement with respect to the case studied by Barri et al. [23], the recirculation zone remains far enough to be affected by the outflow effects. More information regarding the stream-wise length can be obtained in Section 4.4.

Once the physical parameters are controlled, the grid resolution and the time step need to be determined. A Cartesian staggered mesh with $1510 \times 302 \times 360$ grid points has been used to cover the computational domain. The grid spacing in

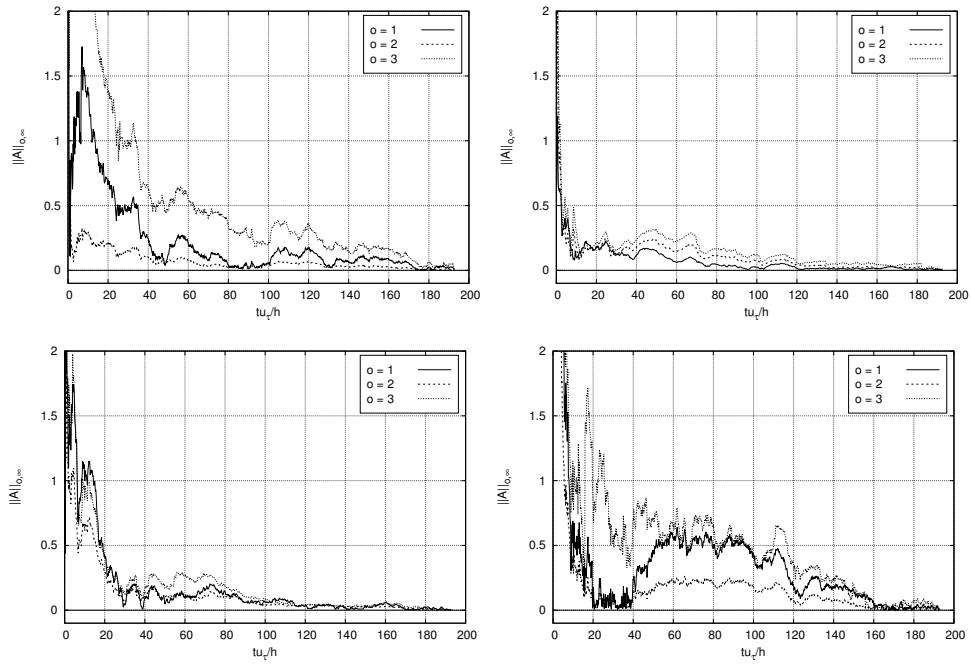


**Figure 2.3:** Normalized infinite norm $(||A||_{o,\infty})$ (defined in Eq.2.9) of the $1^{st}$, $2^{nd}$ and $3^{rd}$ order of the non-zero velocity turbulent statistic at P01(top-left), P02 (top-right), P03 (bottom-left) and P04 (bottom-right). Probes location is defined in figure 2.1.

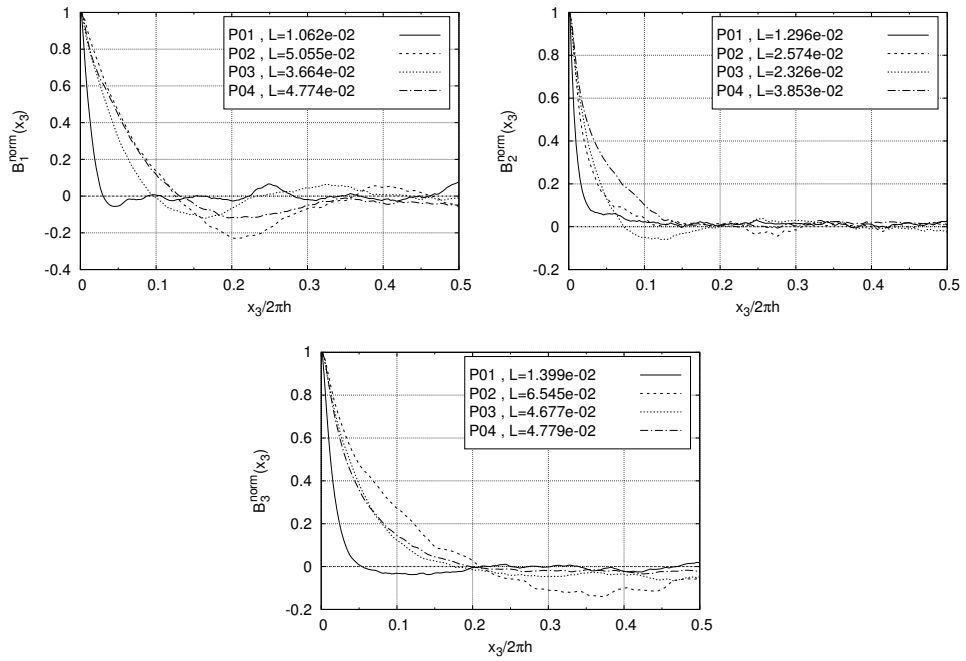


**Figure 2.4:** Two-point correlation in the span-wise direction of three velocity components at $P01$, $P02$, $P03$ and $P04$ location (see figure 2.1). The integral scale value ($L$) of each cross-correlation is presented at the legend. Stream-wise (top-left), Normal (top-right) and Span-wise (bottom) components.

the periodic $x_3$-direction is uniform, whereas the rest of directions use piece-wise hyperbolic-tangent functions. For example, the points distribution in the $x_2$-direction corresponding to the step region, i.e. $-h \leq x_2 \leq 0$ , is given by

$$x_{2,k} = x^a_{2,0} + \frac{h}{2}\left(1 + \frac{tanh\left\{\gamma^a_2\left(2\left(k-1\right)/N_2 - 1\right)\right\}}{tanh\gamma^a_2}\right), \quad k = 1, \ldots, N_2 + 1. \quad (2.11)$$

where the starting point, the grid points number and the refinement factor are $x^a_{2,0} = -h$, $N_2 = 302/2$ and $\gamma^a_2 = 1.16855$. The same is true above the step region, but using $x^a_{2,0} = 0$. In these regions, the mesh is refined in both directions. The grid refinement formula needs to be properly adapted for those areas where the mesh is refined only in one direction (see figure 2.1 for details). For example, the grid points in the region upstream of the step, i.e. $-L_u \leq x_1 \leq 0$, are distributed as follows

$$x_{1,k} = x^l_{1,0} + \frac{L^l_1}{2}\left(1 + \frac{tanh\left\{\gamma^l_1\left(\left(k-1\right)/N^l_1 - 1\right)\right\}}{tanh\gamma^l_1}\right), \quad k = 1, \ldots, N^l_1 + 1. \quad (2.12)$$

where $l$ refers to the zone which is being studied ($a$,$b$,$c$). In this case $l = a$, while the starting point, the region length and the refinement factor are $x^a_{1,0} = -L_u$, $L^a_1 = L_u$ and $\gamma^a_1 = 1.1$, respectively. The same technique is applied in the outflow region ($l = c$), where $x^c_{1,0} = L_{d1}$ and $\gamma^c_1 = 1.5$. There are no arrows in region $l = b$, as a uniform distribution is imposed in order to increase the mesh resolution in this area and capture the shear layer phenomena. Finally, the number of grid points follows straightforwardly by imposing that $N^a_1 + N^b_1 + N^c_1 = N_1 = 1510$, and that the sizes of two consecutive control volumes corresponding to different areas are equal. The grid points in the $x_2$-direction are distributed following the same restrictions.

Mesh quality has been assessed using the present DNS results, analyzing the control volume size next to the wall and at the core. The former is evaluated using wall units, whereas a comparison with the estimated Kolmogorov length scales is performed with the latter. Figure 2.5 presents the mesh dimensions in wall units at the upper and lower walls along the stream-wise direction. It can be noticed as the mesh refinement at the lower wall upstream of the step ($x_1 \leq 0$) has not been provided, due to it exhibits a similar behaviour to the upper wall (difference lower than 1.5%). Hence, Figure 2.5 shows how the selected mesh is fine enough in all directions to perform a channel flow DNS upstream and downstream of the step edge. In particular, the mesh dimension in the normal direction is $\Delta x^+_2 \lesssim 1.3$. A mesh decreasement in wall units is observed in all directions just under the step (lower wall) due to the recirculation bubbles smooth the velocity gradients close to the wall. Although this decreasement also affects $\Delta x^+_1$, its reduction is mainly caused by the mesh refinement in order to capture the well-known massive expansion phenomenon.

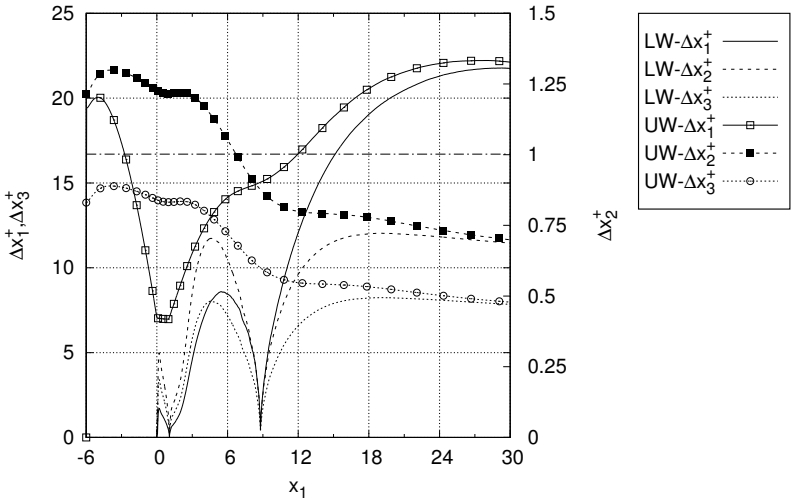


**Figure 2.5:** Mesh dimensions next to the upper ($UW$) and lower ($LW$) walls expressed in wall units ($\delta_+ = \nu/u_\tau$).

It is worth noting here that both walls lead to the same channel flow behaviour far away from the step-edge (recovery region).

Regarding the mesh quality at the core of the BFS, the ratio of different spatial length scales versus the estimated Kolmogorov length scales, $\eta = (\nu^3/\langle\varepsilon\rangle)^{1/4}$, have been evaluated in the sudden-expansion zone. Where $\langle\varepsilon\rangle$ refers to the turbulent kinetic energy dissipation term. The spatial length scale would define the smallest scales that can be created in a given mesh, which not only depends on the mesh itself but also on the flow behaviour. In this context, two common approaches for assessing the spatial length scales are considered : the ratio of the maximum local control volume dimension, $\Delta_{max} = \max(\Delta x_1, \Delta x_2, \Delta x_3)$, and the cube root of the cell volume, $\Delta_\forall = (\Delta x_1 \Delta x_2 \Delta x_3)^{1/3}$. The former is prefereable in zones with isotropic-like turbulence, while the latter performs better in zones where important anisotropies are present [35]. The consequences of the spatial length election in the sudden-expansion zone can be observed in Figure 2.6, where the ratio values using both scales are displayed. First, the highest values in both figures (left,right) are located downstream of the step-edge and at the reattachment zone. The former is caused by the shear layer effects, while the latter is attributed to the mesh coarsening in the stream-wise direction. In addition, the ratio $\Delta_{max}/\eta$ (left) generally presents higher values than $\Delta_\forall/\eta$ (right).

It is worth noting here that, even though $\Delta_{max}/\eta$ (left) is considerably larger at

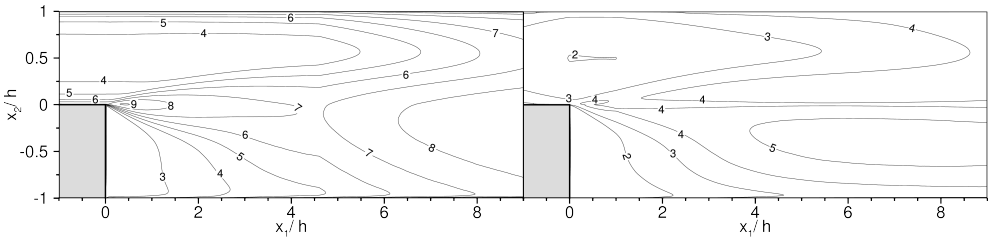


**Figure 2.6:** Mesh quality assessment, comparing different local spatial scales with the Kolmogorov length scales, $\eta$. Those are: the maximum local control volume dimension (left), $\Delta_{max}$, and the cell volume cube root (right), $\Delta_{\forall}$.

the shear layer, it is not a suitable criterion due to the high flow anisotropies (2D-like). Therefore, in this case the $\Delta_{\forall}$ (right) ratio would be more representative. The contrary is true downstream of the shear layer, at the core of the channel, where the flow starts the recovery process. In any case, values higher than 10 are not observed, which is similar to the resolution requirements discussed by Trias et al. [36]. In this regard, a recent work carried out by Vreman & Kuerten [37] has shown that most of the dissipation in a turbulent channel flow occurs at scales greater than $30\eta$. Finally, a good agreement with the results provided by Meri & Wengle [22] have also been observed, though these authors provided only shorthand information regarding this verification part.

## 2.4 Results and discussions

The average flow fields and the time dependent signals collected during the simulation are discussed in this section. For the sake of clarity, this work only contains the most signficant results according to the authors' criterion. All data obtained in this research is publicly available on internet [25].

### 2.4.1 Time-averaged flow

The pressure coefficient distribution, $\langle C_p \rangle = (\langle p \rangle - p_o)/\frac{1}{2}U_c^2$, the velocity components and the streamlines of the average flow in the recirculation region are shown in figure 2.7. Here $p_o$ refers to the kinematic pressure at the step-edge. The sudden expansion leads to a massive flow separation (bottom), and its respective adverse pressure gradient (top). The velocity field distribution (centre) is consistent with the pressure rise and the streamlines. Velocity components are depicted in a different

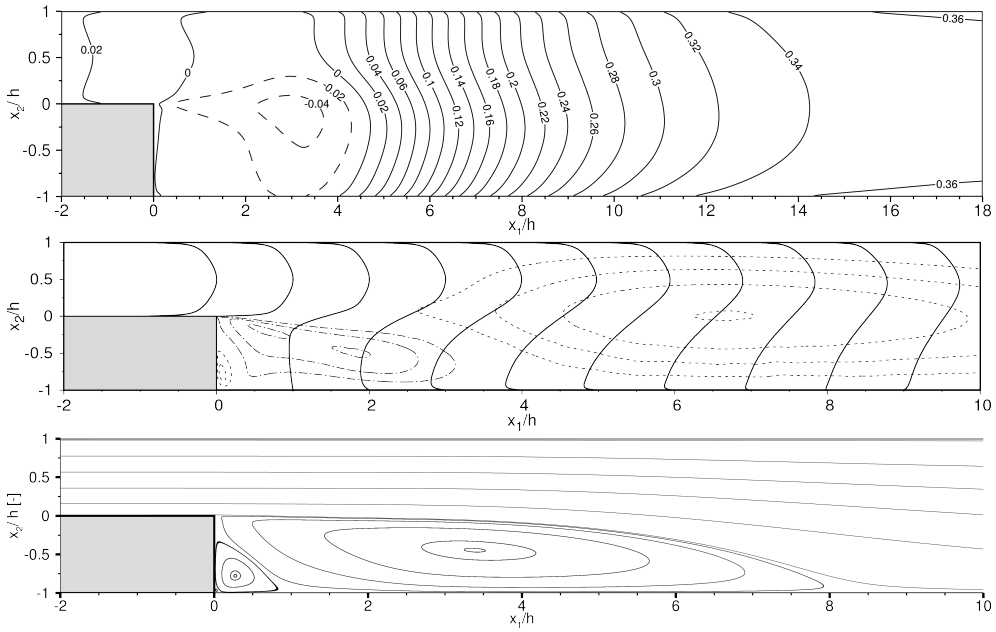


**Figure 2.7:** Pressure coefficient distribution (top), $\langle C_p \rangle$, the average velocity field (centre), $\langle u_i \rangle$, and flow streamlines in the recirculation region (bottom). For the sake of clarity, the stream-wise velocity, $\langle u_1 \rangle$, is referred using solid lines, wheras the normal velocity component, $\langle u_2 \rangle$, is depicted using isolines (where dashed lines denote positive values and dot-dashed lines denote negative ones). The $\langle u_1 \rangle$ values have been normalized using the maximum velocity at each profile, following the Ötügen [8] criterion.

manner in order to improve its visualization and provide a dynamic perception. The $\langle C_p \rangle$ rise at the lower wall across the stream-wise direction is detailed in figure 2.8 (bottom). DNS data shows a good agreement in comparison with the experimental work carried out by Ötügen [8], though higher adverse pressure gradient were detected by this author. The skin friction, $\left\langle C_f \right\rangle = \langle \tau_w \rangle / \frac{1}{2}\rho U_c^2$, is also presented in the same figure at the upper and lower walls (top), which are compared to the numerical DNS results obtained by Barri et al. [23] ($Re_\tau = 180, ER = 2$). Regarding the Jovic & Driver [5] study, a significant reduction of the $\left\langle C_f \right\rangle$ negative peak located at the lower wall ($LW$) is perceived when the $Re_b$ increases. It points out a depletion of the diffused momentum in the recirculation region with respect to the amount of

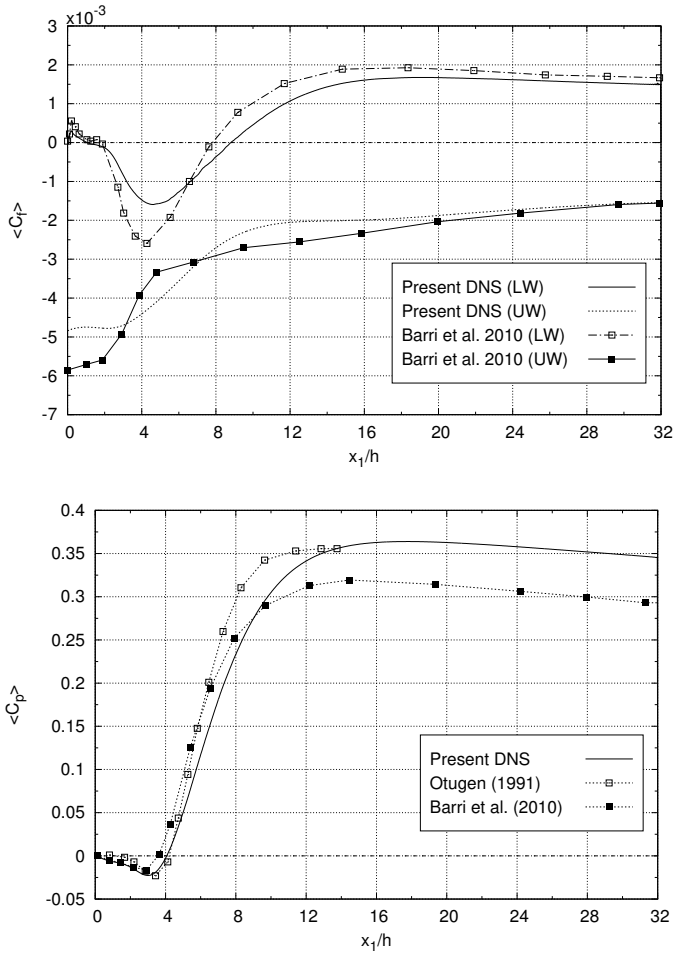


**Figure 2.8:** Comparison of the skin friction (top), $\left\langle C_f \right\rangle$, at $Re_\tau = 395$ (present DNS) with the results obtained by Barri et al. [23] at $Re_\tau = 180$ using an $ER = 2$. The $\left\langle C_f \right\rangle$ is assessed in the lower $(LW)$ and upper $(UW)$ walls. Pressure coefficient (bottom), $\left\langle C_p \right\rangle$, at the $LW$ obtained in the present DNS compared to the results provided by Barri et al. [23], $Re_\tau = 180$, and Ötügen [8], $Re_\tau = 395$.

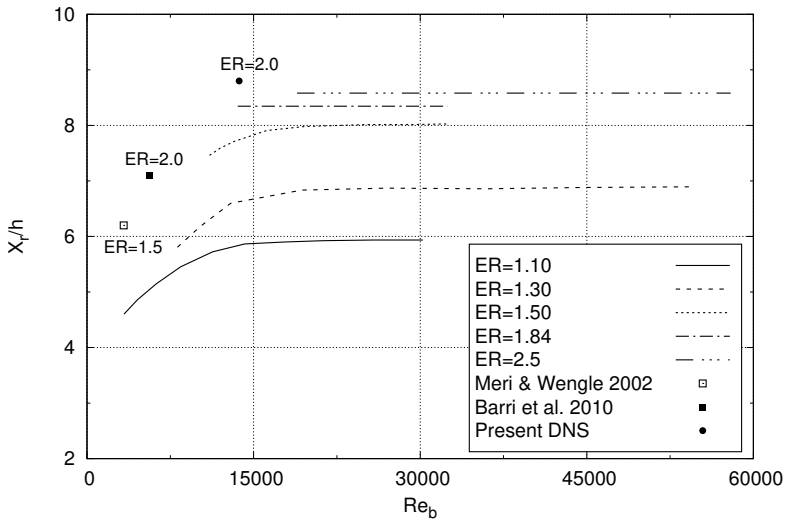


**Figure 2.9:** Recirculation length ($X_r$) using different Reynolds ($Re_b$) and expansion ratios ($ER$). Experimental results depicted by lines were obtained by Nadge & Govardhan [9].

momentum that is entering through the inflow. According to the literature, the $X_r$ elongation phenomenon is also observed, exhibiting an $X_r$ equal to $8.8h$ at $Re_\tau = 395$ and $7.1h$ at $Re_\tau = 180$. This trend is detailed in figure 2.9, where the DNS results of different authors are compared with the experimental results obtained by Nadge & Govardhan [9]. The present DNS is not only located in the asymptotic region, but also exhibits a good agreement with the experimental data (relative difference $\leq 3.5\%$). It is worth noting that the $X_r$ value reported by Ötügen [8] work is not presented in this figure as the author evaluated this coefficient considering other methodologies. Even so, not all results provided by Ötügen [8] have been disregarded, such as the stream-wise velocity and *rms* profiles, which have been compared with the present DNS at different locations in figure 2.10. Although some differences can be observed, an acceptable agreement is present in both variables. The discrepancies observed between the experimental and numerical data could be related to the important scattering registered by Nadge & Govardhan [9]. The author reflected his concerns about this topic, concluding that other elements in addition to the Reynolds number and the $ER$ could affect the massive expansion behaviour. In particular, the flow performance just before the sudden expansion is considered an influential factor, though it has not been commonly reported in the literature. In this chapter a $Re_\tau = 400.5$

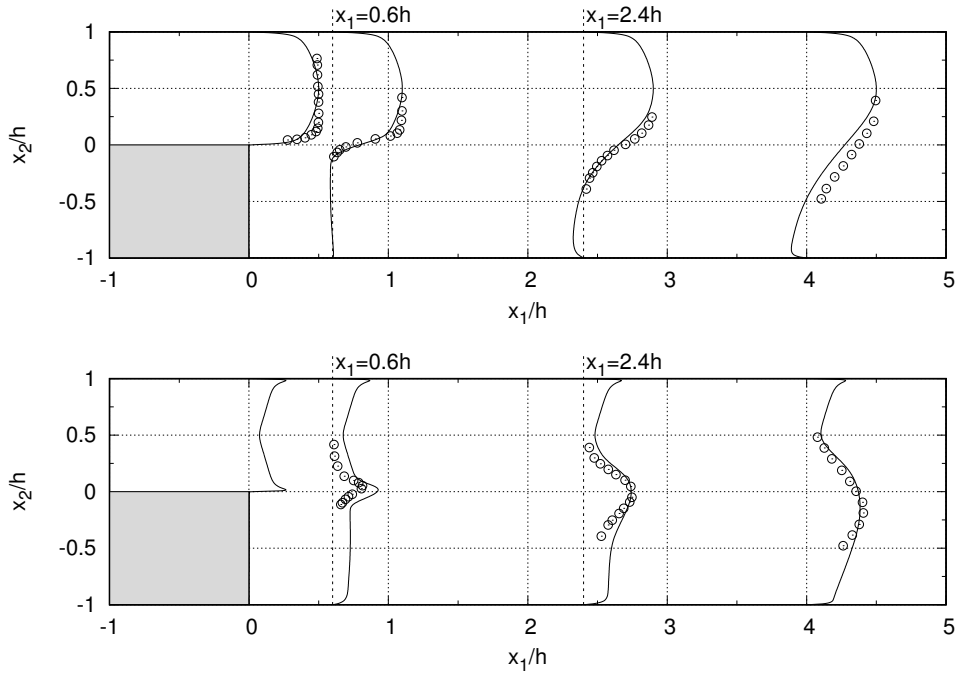


**Figure 2.10:** Stream-wise velocity (top) and *rms* (bottom) profiles of the present DNS (−) compared to the experimental results (⊙) obtained by Ötügen [8]. Velocity ($u_1$) and *rm* are normalized using the maximum value at each profile, $U_c$.

and a turbulence intensity in the stream-wise direction equal to $u_{rms}/U_c \approx 3.8\%$ are observed. Hence, the lack of agreement observed in figure 2.10 could be attributed to the fluid behaviour misalignments at the step-edge.

The strong turbulence behaviour presented in this BFS configuration is quantified through the Reynolds stresses, as well as the production and dissipation terms derived from their respective transport equations.

$$\underbrace{\partial_t \left\langle u_i' u_j' \right\rangle}_{\simeq 0} + \underbrace{\langle u_k \rangle \, \partial_k \left\langle u_i' u_j' \right\rangle}_{\text{Convection}} = \underbrace{\left\langle P_{ij} \right\rangle}_{\text{Production}} + \underbrace{\left\langle \Pi_{ij} \right\rangle}_{\text{Pressure-Strain}} + \underbrace{\left\langle D_{ij} \right\rangle}_{\text{Diffusion Terms}} - \underbrace{\left\langle \varepsilon_{ij} \right\rangle}_{\text{Dissipation}} , \tag{2.13}$$

where:

$$\langle P_{ij} \rangle = - \langle u_i' u_k' \rangle \partial_k \langle u_j \rangle - \left\langle u_j' u_k' \right\rangle \partial_k \langle u_i \rangle , \tag{2.14a}$$

$$\langle \Pi_{ij} \rangle = \left\langle p' (\partial_j u_i' + \partial_i u_j') \right\rangle , \tag{2.14b}$$

$$\langle D_{ij} \rangle = -\partial_k [\left\langle u_i' u_j' u_k' \right\rangle + (\left\langle p' u_j' \right\rangle \delta_{ik} + \langle p' u_i' \rangle \delta_{jk}) - \nu \partial_k \left\langle u_i' u_j' \right\rangle], \tag{2.14c}$$

$$\langle \varepsilon_{ij} \rangle = 2\nu \left\langle \partial_k u_i' \partial_k u_j' \right\rangle . \tag{2.14d}$$

In order to simplify the analysis process, only the non-zero components are depicted and nearly the same layout as used by Barri et al. [23] is considered. A general increasement of the Reynolds stresses is well observed in all directions in comparison to Barri et al. [23] results. A downstream shifting of the Reynolds stress zero-gradient area can also be appreciated.

The highest momentum oscillations are in the stream-wise direction, $\langle u_1' u_1' \rangle$, as can be noticed in figure 2.11 (top). This turbulence, which is triggered by the huge emanation term (middle-left), is balanced by the isotropization behaviour of the pressure-strain (middle-right). In fact, the energy from the most energetic components (stream-wise) is distributed to weakest ones (normal and span-wise directions) because of the pressure-strain phenomenon. In contrast to the channel flow behaviour, some positive values appear in the impinging regions. They are located at the end of the recirculation length and at the lower part of the shear layer. In both cases, the velocity in the stream-wise direction is accelerated $\partial_1 u_1$, whereas some pressure positive peak rises from the impinging interactions. As was expected, the dissipation term, $\langle \varepsilon_{11} \rangle$, is positive and achieves its maximum values in the shear layer and close to the walls. At the lower wall, the opposite is true due to the oscillations and gradient reduction at the recirculation bubble zone.

Fluctuations in the normal direction, $\langle u_2' u_2' \rangle$, are shown in figure 2.12 (top). Although in this case they are less energetic in comparison to $\langle u_1' u_1' \rangle$, they remain significant. The production term (middle-left) is non-zero, in contrast to a channel flow, and significantly lower than the pressure-strain (middle-right). Dissipation term (bottom) is also positive and, as was expected, stronger in the shear layer and close to the walls.

The periodic nature of the span-wise direction, $\langle u_3' u_3' \rangle$, leads to an absence of the production term. However, the oscillations in this direction (see top figure 2.13) are nearly as vivid as the stream-wise ones. This phenomenon occurs because of the isotropization effect of the pressure-strain tensor, which converts the $\langle u_1' u_1' \rangle$ fluctuations into $\langle u_3' u_3' \rangle$ ones. The dissipation (right-bottom) term presents the same trend the above-mentioned Reynolds stresses.

In order to complete the Reynolds stress assessment, the Reynolds stress non-zero cross-term ($- \langle u_1' u_2' \rangle$) is depicted in figure 2.14 (top). The classic axisymmetry pre-

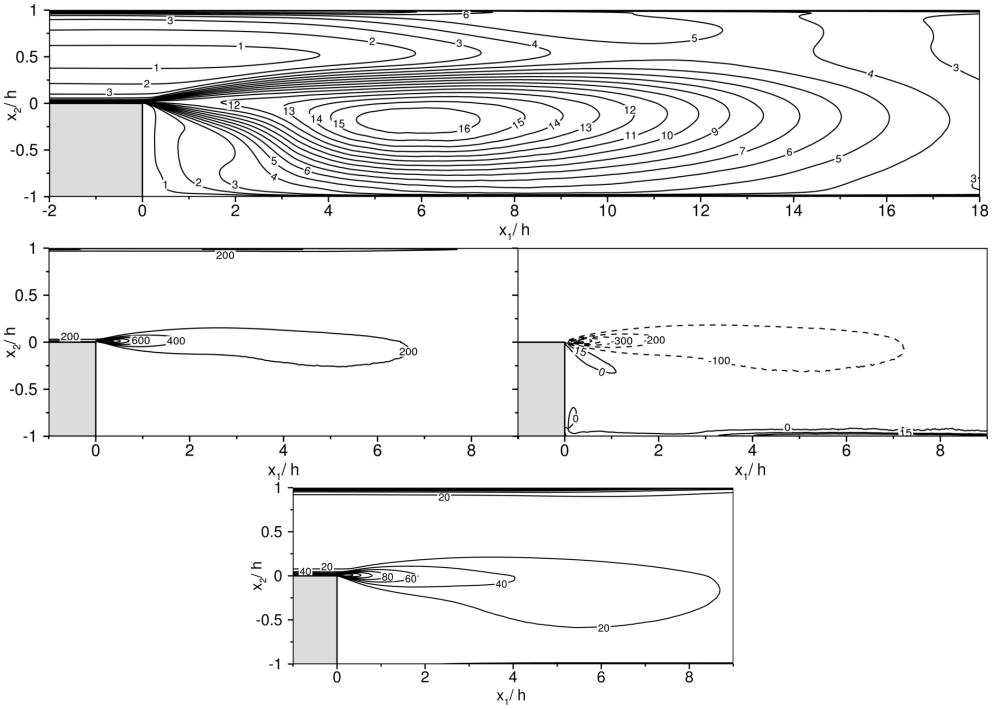


**Figure 2.11:** Reynolds stress $\langle u_1' u_1' \rangle / u_\tau^2$ (top) and their associated transport source-sink terms scaled using $u_\tau^3/h$: production $\langle P_{11} \rangle$ (middle-left), pressure-strain $\langle \Pi_{11} \rangle$ (middle-right) and dissipation $\langle \varepsilon_{11} \rangle$ (bottom). Dashed lines depict negative values.

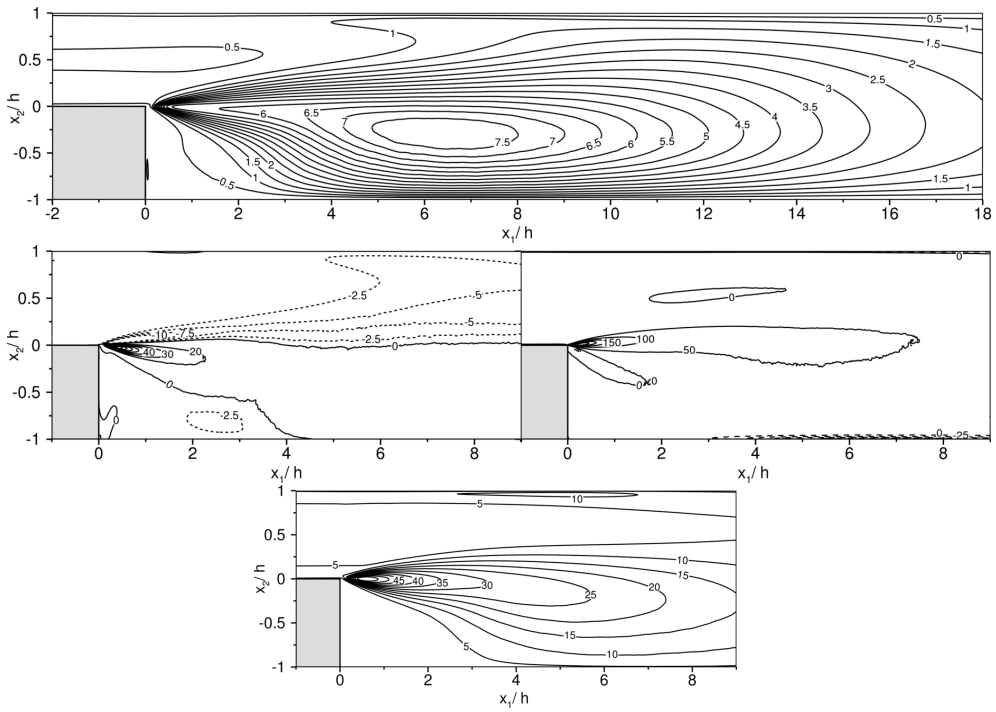


**Figure 2.12:** Reynolds stress $\langle u_2' u_2' \rangle / u_\tau^2$ (top) and their associated transport source-sink terms scaled using $u_\tau^3/h$: production $\langle P_{22} \rangle$ (middle-left), pressure-strain $\langle \Pi_{22} \rangle$ (middle-right) and dissipation $\langle \varepsilon_{22} \rangle$ (bottom). Dashed lines depict negative values.

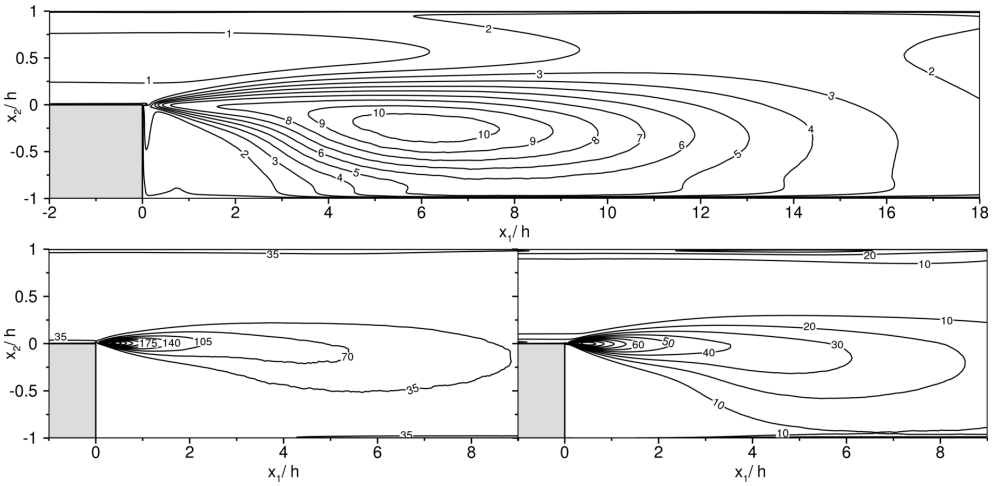


**Figure 2.13:** Reynolds stress $\langle u_3' u_3' \rangle / u_\tau^2$ (top) and their associated transport source-sink terms scaled using $u_\tau^3/h$: pressure-strain $\langle \Pi_{33} \rangle$ (left-bottom) and dissipation $\langle \varepsilon_{33} \rangle$ (right-bottom). Dashed lines depict negative values.

sented in a channel flow is lost downstream of the step, but slowly recovered after the reattachment. Although this term does exhibit rather weak values (top) in comparison to the other stresses, their production (middle-left) and pressure-strain (middle-right) terms are quite energetic. Both terms almost present a complementary behaviour in the shear layer, explaining why the dissipation term in this zone is nearly zero.

### 2.4.2 Flow dynamics

Once the average time properties have been analyzed, the time dependent variables are assessed. An idea of the flow dynamics is given in figure 2.15, where the pressure gradient magnitude in the recirculation zone is shown. First, *KH* structures are visualized just after the sharp edge (bottom), leading to the highest Reynolds stress values in the BFS domain (see figure 2.11-2.14). In contrast, a particular lack of pressure gradient is observed in the secondary recirculation bubble region due to its non-turbulent behaviour. Additional information is provided in the film [25], i.e. the slow motion of the recirculation bubble flow and the progressive expansion of the mainstream flow downstream of the step. The sudden expansion effects into the flow topology can also be noticed in the normal view at $x_2^+ = 1$ in figure 2.16. For instance, the turbulence triggering produced by the step-edge are visualized with

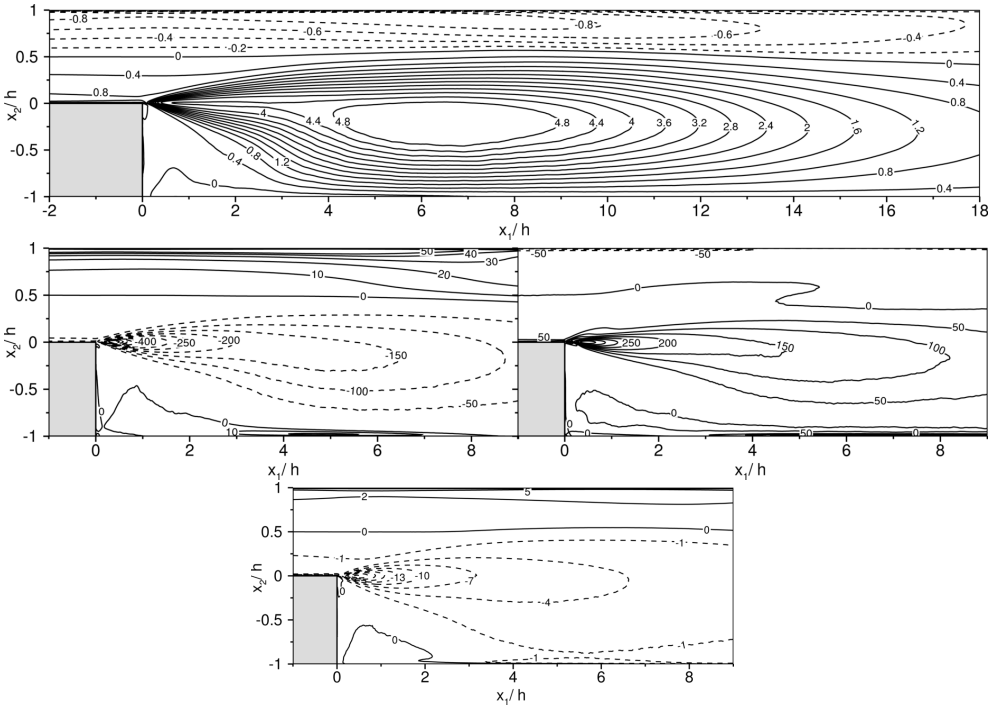


**Figure 2.14:** Reynolds stress $-\left\langle u_1' u_2' \right\rangle / u_\tau^2$ (top) and their associated transport source-sink terms scaled using $u_\tau^3/h$: production $\langle P_{12} \rangle$ (middle-left), pressure-strain $\langle \Pi_{12} \rangle$ (middle-right) and dissipation $\langle \varepsilon_{12} \rangle$ (bottom). Dashed lines depict negative values.

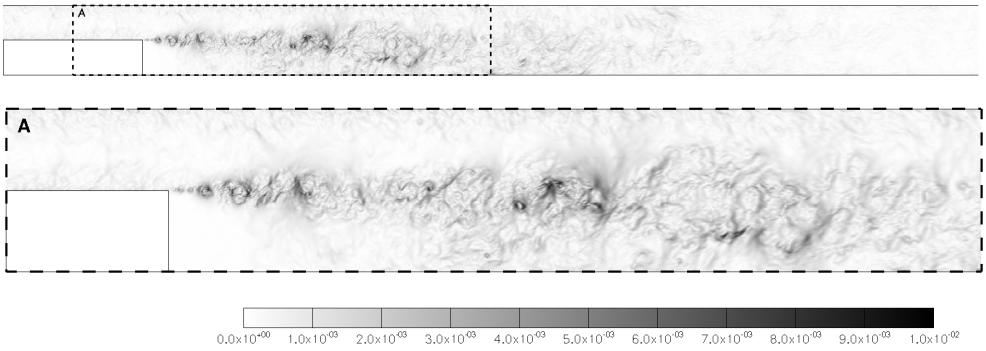


**Figure 2.15:** Instantaneous magnitude of the dimensionless pressure gradient in a large part of the BFS domain (top), and a detailed view ($A$) of the sudden expansion (bottom). The gray scale represents the following expression, $\frac{h}{u_\tau^2}\sqrt{\partial_i p \partial_i p}$. See the film attached in the paper data base [25].

the $Q$-invariant (top), showing how the highest intensity is located just downstream of the expansion. Furthermore, the channel flow streaks are also well-observed in figure 2.16 (bottom) until the sudden expansion. Downstream of the step-edge, nearly "$2D$" coherent structures are shown from 0 up to $\sim 0.5h$ in the $u_2'$ figure (bottom-left). Beyond this threshold, the "$2D$" coherence is lost, but the structures still grow. A similar behaviour can be observed in $u_1'$ (bottom-right).

Besides the turbulence triggered at the step-edge and its respective spreading, figures 2.15 and 2.16 also display a significant flow heterogeneity. In order to assess such diversity of flow regimes, the turbulent kinetic energy cascade at different locations has been considered (see figure 2.17). A schematic view of the probes location can be observed in figure 2.1. Unfortunately, $KH$ instabilities are not well captured in figure 2.17 (top), as their low energy structure effects can be easily hidden by turbulent scales coming from the channel flow boundary layer. Even so, a good trend is observed in the inertial zone ($\bar{f}^{-5/3}$). It is worth noting here that the $P02$ frequency cascade has not been included in this figure, as the probe is located in a quasi-laminar region. Regarding the rest of $\bar{f}^{kmg}$ shown in figure 2.17, they diminish along the downstream direction because of the sudden expansion ($P03$,$P04$). Due to the spatial scale is $ER$ times higher at the outflow, the flow moves $ER$ times slower in order to ensure the mass conservation law. Consequently, time scale is decreased by a factor of $ER^2$, bringing out the $\bar{f}^{kmg}$ observed trend (these relations can be easily demonstrated through dimensional analysis).

Even though the ejection frequency of the $KH$ instabilities has not been well-

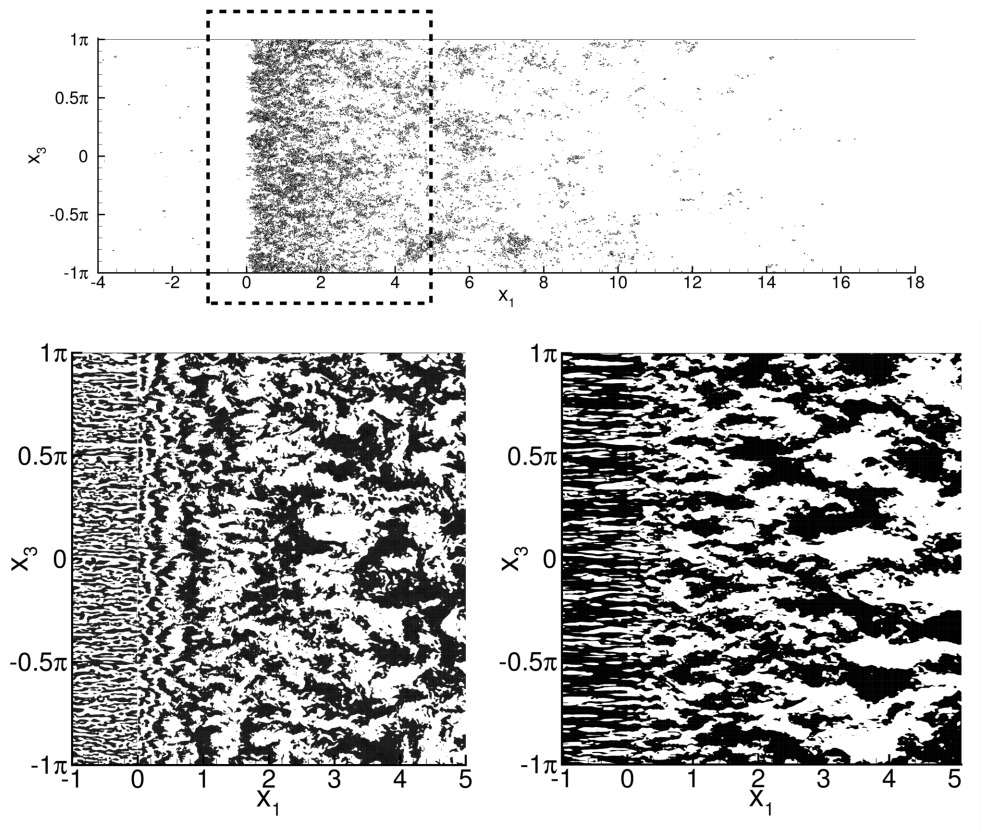


**Figure 2.16:** A normal slice at $x_2^+ = 1$ showing instantaneous views of the $Q$-invariant (top), $u_2'$ (bottom-left) and $u_1'$ (bottom-right). Black zones denote the highest values of the $Q$-invariant at the top figure and positive values at the bottom ones.

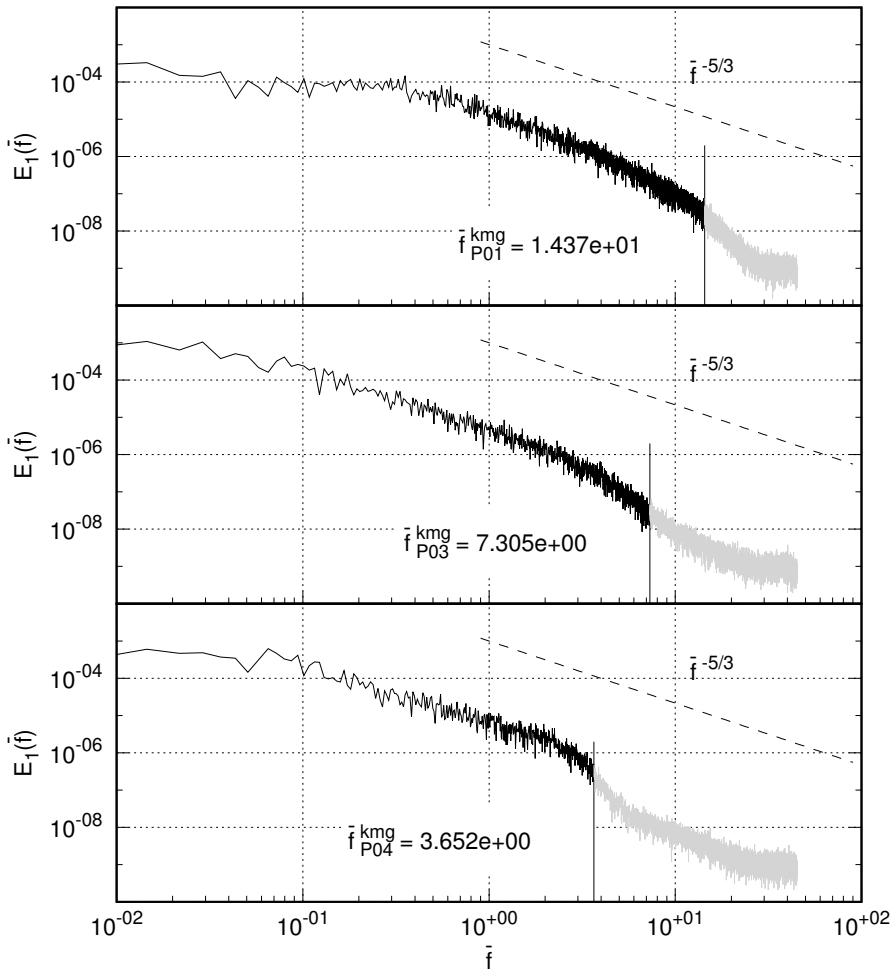


**Figure 2.17:** Normalized turbulent kinetic energy ($E_1$) *vs* normalized temporal frequency ($\bar{f} = fh/U_b$) at P01 (top), P03 (centre) and P04 (bottom). The dashed lines represent the expected turbulence decayment behaviour at the inertial region ($\bar{f}^{-5/3}$), whereas $\bar{f}^{kmg}_{P0N}$ denotes the local Kolmogorov temporal frequency in probe $N$.

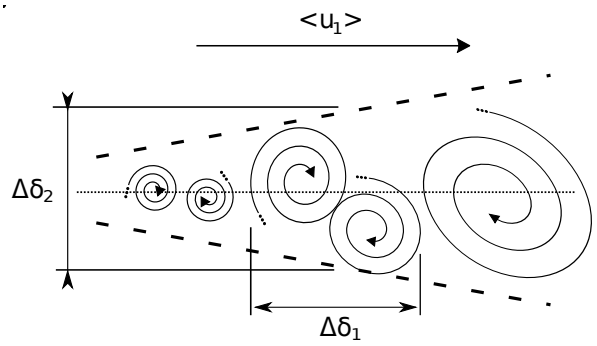


**Figure 2.18:** Schematic view of the Kelvin-Helmholtz in a shear layer, where $\Delta\delta_1$ and $\Delta\delta_2$ represent a estimation of the vortex size in the stream-wise and normal direction, respectively.

captured in $P01$, other interesting shear layer properties have been discerned, such as the $KH$ rates of growth along the stream-wise direction. A schematic view of a shear layer is presented in figure 4.9, showing different structures' size in the stream-wise ($\Delta\delta_1$) and normal ($\Delta\delta_2$) direction.

This vortex elongation was mainly attributed to the advection velocity and the vortex pairing phenomenon, which was studied by Winant & Browand [26]. In particular, an elliptic-like shape was experimentaly detected, observing a major-to-minor axis ratio of $\Delta\delta_1/\Delta\delta_2 \sim 2$. This behaviour has been analysed with the present DNS data through the two-point correlation technique in the stream-wise and normal directions. In the $\Delta\delta_1$ case, the distance from peak to peak (upstream) has been used for representing the distance between vortices (figure 2.19, top) and also an estimation of the average vortex size in a given position, $B_2^{norm}(x_1, \hat{x}_1)$. In contrast, $\Delta\delta_2$ has been measured as the distance between zero values of the two-point correlation values, $B_1^{norm}(x_2 = 0, \hat{x}_2)$. In addition, $\Delta\delta_2$ has also been assessed following the equation given in Winant & Browand [26],

$$\Delta\delta_2 = \Delta U_1 / (\partial \langle u_1 \rangle / \partial x_2)_{\max} \tag{2.15}$$

where $\Delta U_1$ referes to the flow velocity difference in the shear layer.

Two linear distributions for $\Delta\delta_1$ and $\Delta\delta_2$ have been obtained through the two-point correlation technique, showing circular structures ($\Delta\delta_1 \sim \Delta\delta_2$) just downstream of the step-edge ($\sim 0.4h$). This is in good agreement with the "2D" coherent structures observed in figure 2.16. Above this threshold, the circular structures are distorted acquiring an elliptic shape ($\Delta\delta_1 > \Delta\delta_2$), which can be attributed to the abovementioned phenomena. This elliptical shape trend seems to be mantained along the studied do-

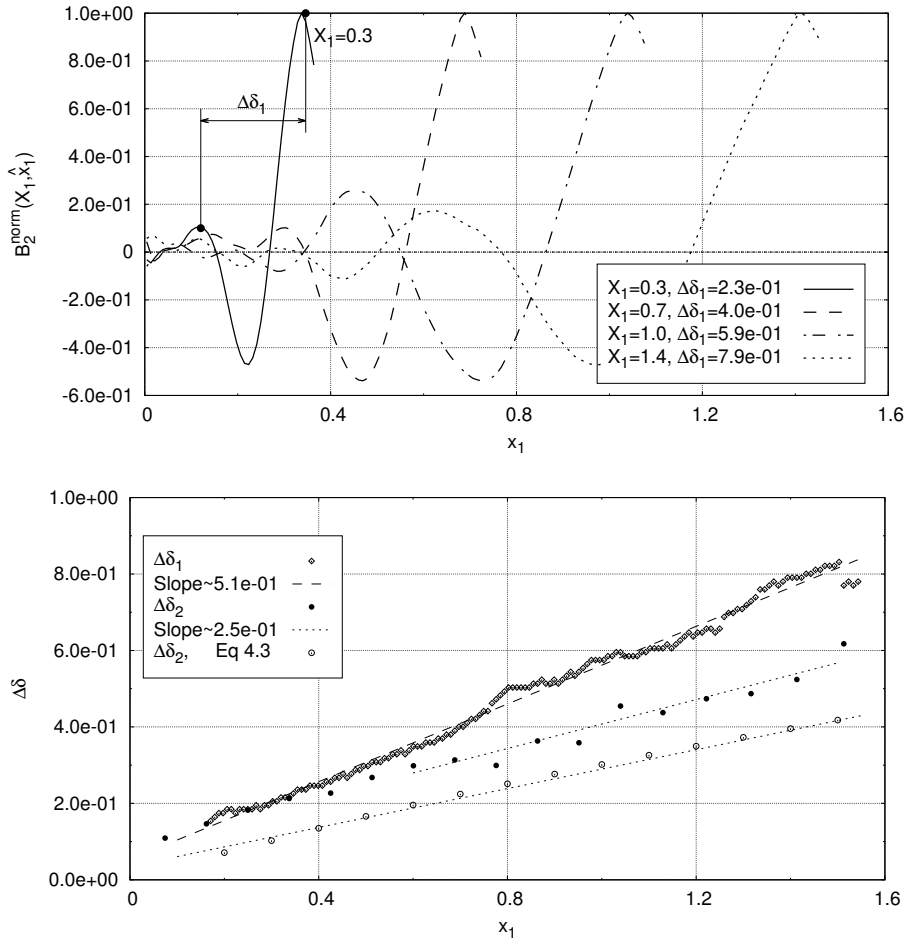


**Figure 2.19:** An example showing how $\Delta\delta_1$ have been assessed using two-point correlation at the shear layer (top). Estimation of the *KH* rate of growth ($\Delta\delta_1$,$\Delta\delta_2$) along the stream-wise direction (bottom), which is schematically depicted in figure 4.9.

main, showing a major-to-minor axis ratio limit close to 2 ($\Delta\delta_1 / \Delta\delta_2$), strenghening the experimental visualitzations carried out by Winant & Browand [26] and supporting its theory regarding the vortex pairing [25]. It is worth noting that Kostas et al. [27] observed a similar phenomenon in its BFS experimental study. Finally, the offset observed between both $\Delta\delta_2$ approaches does not seem to be critical, as both linear distributions present a similar slope. It indicates that in both cases the elongation ratio, $\Delta\delta_1 / \Delta\delta_2$, share a similar growing trend ($\sim 2$). However, this correlation is lost downstream of the studied region ($x_1 > 2$), where the free shear layer is no longer present.

## 2.5 Conclusions

A DNS of a BFS with a $ER = 2$ has been carried out at $Re_\tau = 395$, defining a case close to the $X_r$ asymptotic behaviour. A turbulent channel flow has been used as an inflow, which has been obtained from a previous simulation. The flow performance $1h$ downstream of the inflow has shown a good agreement with the well-known benchmark results provided by [34], indicating no need of recovery region. During the verification part other parameters have also been discussed: the time integration period, domain dimensions and mesh resolution. All tests have provided reasonable results concluding that the parameter values satisfy the challenging DNS requirements. Once verified, the DNS results have been compared with the experimental and numerical studies present in the literature. Besides presenting good agreement with the experimental results, the nearness in the $X_r$ asymptotic behaviour zone has also been observed. In addition, numerical benchmark results have also been considered, i.e. Barri et al. [23]. The author provided DNS results of a BFS with $ER = 2$, considering a turbulent inflow at $Re_\tau = 180$. In particular, the present DNS exhibited a significant reduction of the $\left\langle C_f \right\rangle$ peak in the recirculation region. This phenomenon was previously reported by Jovic & Driver [38] experimental work. Regarding the complexity of the flow dynamics, instantaneous views in the span-wise and normal direction have shown the evolution of the flow structures in the stream-wise direction. The Kelvin-Helmholtz instabilities can be distinguished in those planes, but they have not been detected in the kinetic energy spectra. However, their rate of growth have been identified through two-point correlations in the stream-wise and normal directions. A switching from circular to elliptical structures has been detected close to the step-edge (up to $\sim 0.4h$) produced by the advection velocity and the vortex pairing phenomenon. Finally, the elliptical shape trend agrees with the experimental observations carried out by Winant & Browand [26], showing a major-to-minor axis ratio close to 2.

# References

[1] J.K. Eaton and J.P. Johnston. Turbulent flow reattachment: An experimental study of the flow and structure behind a backward facing step. 1980.

[2] B.F. Armaly, F. Durst, JCF. Pereira, and B. Schonung. Experimental and theoretical investigation of backward-facing step flow. *Journal of Fluid Mechanics*, 127:473–496, 1983.

[3] D.M. Driver and H.L. Seegmiller. Features of a reattaching turbulent shear layer in divergent channel flow. *AIAA Journal*, 23(2), 1985.

[4] N. Kasagi and A. Matsunaga. Three-dimensional particle-tracking velocimetry measurement of turbulence statistics and energy budget in a backward-facing step flow. *International Journal of Heat and Fluid Flow*, 16(6):477–485, 1995.

[5] S. Jovic and D. Driver. Reynolds number effect on the skin friction in separated flows behind a backward-facing step. *Experiments in Fluids*, 18(6):464–467, 1995.

[6] D.M. Kuehn. Effects of adverse pressure gradient on the incompressible reattaching flow over a rearward-facing step. *AIAA Journal*, 18(3), 1980.

[7] F. Durst and C. Tropea. Turbulent backward-facing step flows in two-dimensional ducts and channels. In *Proceedings of Turbulent Shear Flow 3 Symposium Davis September*, 1981.

[8] M.V. Ötügen. Expansion ratio effects on the separated shear layer and reattachment downstream of a backward-facing step. *Experiments in Fluids*, 10(5), 1991.

[9] P.M. Nadge and R.N. Govardhan. High Reynolds number flow over a backward-facing step: Structure of the mean separation bubble. *Experiments in Fluids*, 55(1), 2014.

[10] V. De Brederode and P. Bradshaw. Three-dimensional flow in nominally two-dimensional separation bubbles. I. Flow behind a rearward-facing step. Technical report, IC Aero Rep 72-19 Imperial College, London, 1972.

[11] C.G. Speziale and T. Ngo. Numerical solution of turbulent flow past a backward facing step using a nonlinear K-$\epsilon$ model. *International Journal of Engineering Science*, 26(10):1099–1112, jan 1988.

[12] S. Thangam and C.G. Speziale. Turbulent flow past a backward-facing step - A critical evaluation of two-equation models. *AIAA Journal*, 30(5):1314–1320, may 1992.

[13] William C Lasher and Dale B Taulbee. On the computation of turbulent backstep flow. *International Journal of Heat and Fluid Flow*, 13(1):30 – 40, 1992.

[14] P. R. Spalart, W. H. Jou, M. Strelets, and S. R. Allmaras. Comments on the feasibility of LES for wings, and on a hybrid RANS/LES approach. In *C. Liu & Z. Liu (eds.) Advances in DES/LES*. Greyden Press, Columbus, OH, 1997.

[15] P. R. Spalart, S. Deck, M. L. Shur, K. D. Squires, M. Kh Strelets, and A. Travin. A new version of detached-eddy simulation, resistant to ambiguous grid densities. *Theoretical and Computational Fluid Dynamics*, 20(3):181–195, 2006.

[16] Mikhail L. Shur, Philippe R. Spalart, Mikhail Kh Strelets, and Andrey K. Travin. A hybrid RANS-LES approach with delayed-DES and wall-modelled LES capabilities. *International Journal of Heat and Fluid Flow*, 29(6):1638–1649, 2008.

[17] Mikhail S. Gritskevich, Andrey V. Garbaruk, Jochen Schütze, and Florian R. Menter. Development of DDES and IDDES formulations for the k-$\omega$ shear stress transport model. *Flow, Turbulence and Combustion*, 88(3):431–449, 2012.

[18] C. Mockett, W. Haase, and D. Schwamborn. *Go4Hybrid: Grey Area Mitigation for Hybrid RANS-LES Methods.*, volume 134. 2018.

[19] H. Le, P. Moin, and J. Kim. Direct numerical simulation of turbulent flow over a backward-facing step. *Journal of Fluid Mechanics*, 330:349–374, 1997.

[20] G. Biswas, M. Breuer, and F. Durst. Backward-Facing Step Flows for Various Expansion Ratios at Low and Moderate Reynolds Numbers. *Journal of Fluids Engineering*, 126(3):362, 2004.

[21] F. Schäfer, M. Breuer, and F. Durst. The dynamics of the transitional flow over a backward-facing step. *Journal of Fluid Mechanics*, 623:85, 2009.

[22] A. Meri and H. Wengle. DNS and LES of turbulent backward-facing step flow using 2nd-and 4th-order discretization. *Advances in LES of Complex Flows*, pages 99–114, 2002.

[23] M. Barri, G.K. El Khoury, H.I. Andersson, and B. Pettersen. DNS of backward-facing step flow with fully turbulent inflow. *International Journal for Numerical Methods in Fluids*, 64(7), 2010.

[24] M. Barri, G.K. El Khoury, H.I. Andersson, and B. Pettersen. Inflow conditions for inhomogeneous turbulent flows. *International Journal for Numerical Methods in Fluids*, 60(2), 2009.

[25] A. Pont-Vílchez, F. X. Trias, A. Gorobets, and A. Oliva. Direct numerical simulation results presented in this chapter. http://www.cttc.upc.edu/downloads/BFS_Ret395_ER2, 2018.

[26] C. D. Winant and F. K. Browand. Vortex pairing : The mechanism of turbulent mixing-layer growth at moderate Reynolds number. *Journal of Fluid Mechanics*, 63(2):237–255, 1974.

[27] J. Kostas, J. Soria, and M. Chong. Particle image velocimetry measurements of a backward-facing step flow. *Experiments in Fluids*, 33(6):838–853, 2002.

[28] R. W. C. P. Verstappen and A. E. P. Veldman. Symmetry-Preserving Discretization of Turbulent Flow. *Journal of Computational Physics*, 187:343–368, 2003.

[29] A. J. Chorin. Numerical Solution of the Navier-Stokes Equations. *Mathematics of Computation*, 22:745–762, 1968.

[30] Trias, F.X. and Lehmkuhl, O. A self-adaptive strategy for the time-integration of Navier-Stokes equations. *Numerical Heat Transfer, part B*, 60(2):116–134, 2011.

[31] A. Gorobets, F. X. Trias, and A. Oliva. A parallel MPI+OpenMP+OpenCL algorithm for hybrid supercomputations of incompressible flows. *Computers & Fluids*, 88:764–772, 2013.

[32] J. Kim and P. Moin. Application of a Fractional-Step Method to Incompressible Navier-Stokes Equations. *Journal of Computational Physics*, 123:308–323, 1985.

[33] F. X. Trias, M. Soria, A. Oliva, and C. D. Pérez-Segarra. Direct numerical simulations of two- and three-dimensional turbulent natural convection flows in a differentially heated cavity of aspect ratio 4. *Journal of Fluid Mechanics*, 586:259–293, 2007.

[34] R. D. Moser, J. Kim, and N. N. Mansour. Direct numerical simulation of turbulent channel flow up to $Re_\tau = 590$. *Physics of Fluids*, 11:943–945, 1999.

[35] Mikhail L. Shur, Philippe R. Spalart, Mikhail Kh Strelets, and Andrey K. Travin. An Enhanced Version of des with Rapid Transition from RANS to les in Separated Flows. *Flow, Turbulence and Combustion*, 95(4), 2015.

[36] F. X. Trias, A. Gorobets, and A. Oliva. Turbulent flow around a square cylinder at Reynolds number 22,000: A DNS study. *Computers and Fluids*, 123(22):87–98, 2015.

[37] A W Vreman and J G M Kuerten. Comparison of direct numerical simulation databases of turbulent channel flow at Re$\tau$ = 180. *Physics of Fluids*, 26(1):15102, 2014.

[38] S Jovic and D Driver. Backward-Facing Step Measurements at Low Reynolds Number, Reh = 5000. *Nasa Technical Memorandum*, (February), 1994.

# 3

# Theory of the new techniques for mitigating the Grey Area in DES models

**Abstract.** This section introduces a new approach for mitigating the unphysical delay in the RANS to LES transition, named *Grey Area*, which is a classical issue for hybrid RANS-LES turbulence models such as Delayed-Detached Eddy Simulation (DDES). We have adapted and tested an existing approach designed for improving the LES performance in complex flow areas. In particular, LES and DDES suffer from an excessive diffusion in critical areas where the flow does not strictly behave in a fully turbulent manner, such as free shear layers. In these situations, dissipation needs to be reduced in order to enable more physically accurate development of turbulence, and thus, the overall meanflow field. In this context, the following section assesses a recent 2D sensitive turbulent model and a new subgrid length scales, initially developed for LES applications, as a new solution for mitigating the *Grey Area*. The standard methodologies for dealing with such a numerical issue are also presented.

## 3.1 Grey Area Numerical Issue

In this thesis, there are only the concepts which are necessary for understanding its content without the need of consulting an excessive amount of bibiliography. However, the author refers the reader to following work, Mockett [1], where a comprehensive study of the DDES methodology is provided.

### 3.1.1 Delayed-Detached Eddy Simulation (DDES)

Accurate numerical simulations are essential for understanding the complex flow physics present in many aeronautical applications. RANS models are commonly used in the industry, as they are cost-effective, but their limitations for predicting complex flow behaviours and providing unsteady data are also well-known. Moreover, the routine use of accurate numerical methodologies such as Large Eddy Simulation (LES) requires heavy computational cost, so their applications are not yet feasible. In this regard, Detached Eddy Simulation (DES [2]) intended to circumvent the massive costs of pure LES simulations, modelling the boundary layer using RANS and simulating the unsteady flow behaviour with LES at the core. Instead of defininig the RANS and LES applicability area, Spalart decided to slightly modify the Spalart-Allmaras model [2] in order to behave like an LES-like model far from the wall, using the following approach

$$\partial_t(\rho\tilde{\nu}) + \partial_j(\rho u_j\tilde{\nu}) = \frac{1}{\sigma}\left(\partial_j\left(\rho\left(\tilde{\nu}+\nu\right)\partial_j\tilde{\nu}\right) + C_{b2}\rho\partial_i\tilde{\nu}\partial_i\tilde{\nu}\right) + \underbrace{C_{b1}\rho\tilde{S}\tilde{\nu}\left(1-f_{t2}\right)}_{\textit{Production Term}} - \underbrace{\left(C_{w1}\rho f_w - \frac{C_{b1}}{\kappa^2}f_{t2}\right)\left(\frac{\tilde{\nu}}{\tilde{d}}\right)^2}_{\textit{Destruction Term}}. \tag{3.1}$$

Where the classical wall distance in the destruction term, $d$, is replaced by

$$\tilde{d} = \min\left(L_{RANS}, L_{LES}\right) = \min\left(d, C_{DES}\Delta\right), \tag{3.2}$$

in order to switch from RANS to LES like turbulence model without the need of defining zones. All coefficients and functions which are not defined in this section can be obtained in the original papers [2, 3].

Unfortunately, DES suffered from important shortcomings, such as the Grey Area and the reduction of the eddy-viscosity ($\nu_e$) from RANS to LES without a corresponding balance by resolved turbulent content, named Model Stress Depletion (MSD). These issues made the model unfeasible for complex applications. Later on, Spalart et al. [3] presented a set of techniques for addressing some of the main issues noticed in

the initial DES version [2], in particular the MSD. In this context, a shielding function,

$$f_d = 1 - \tanh\left[\left(C_{d1} r_d\right)^{C_{d2}}\right],\ r_d = \min\left(\frac{\nu_{eff}}{\partial_j \tilde{u}_i \kappa^2 x_2^2}, 10\right) \tag{3.3}$$

and a model-specific low Reynolds number correction function,

$$\Psi^2 = \min\left[10^2, \frac{1 - \frac{1-C_{b1}}{C_{w1}\kappa^2 f_w^*}\left[f_{t2} + (1 - f_{t2})\, f_{v2}\right]}{f_{v1} \max\left(10^{-10}, 1 - f_{t2}\right)}\right] \tag{3.4}$$

were introduced in Eq. 3.2, leading to

$$\tilde{d} = L_{RANS} - f_d \max(L_{RANS} - L_{LES}, 0), \tag{3.5}$$

where,

$$\begin{aligned} L_{RAS} &= d, \\ L_{LES} &= \Psi C_{DES} \Delta. \end{aligned} \tag{3.6}$$

The new hybrid turbulence model was named Delayed-DES (DDES [3]), as it was able to delay the unintended transitions from RANS to LES in certain regions with an excessive refinement, where the RANS area was not well-defined by the $L_{RANS}$. Due to its user-friendly non-zonal approach and its proved success in several applications, DDES became in a widely used hybrid turbulence model. Especially in those situations where RANS models is unreliable, such as in the obtention of high quality transient data.

### 3.1.2 Grey Area (GA)

Even though DDES provided a set of improvements respect to its precedessor, some of the initial DES weaknesses are still present. In particular, the slow transition from RANS to LES, which leads to unphysical results, harming the triggering of the flow instabilities in the zone known as GA. This delay in the triggering process could significantly affect the flow dynamics downstream of the flow, as well as those kind of physics that require high quality unsteady turbulent motion, such as fluid structure interaction and computational aeroacoustics.

The unphysical delay is caused by the slow $\tilde{\nu}$ transition process between both areas, GA, where the values in the RANS zone are significantly higher than in the LES one. Depending on the flow conditions, $\tilde{\nu}$ could be even 0 in the LES area. In order to ensure a proper GA mitigation, the $\tilde{\nu}$ distribution in such area needs to be sharpened. Taking into account that DDES is not zonal (based on a unique transport

equation, Eq. 3.1), the only way to reduce the $\tilde{\nu}$ expression is identifying and acting on the parameters that control the $\tilde{\nu}$ behaviour in the LES area. These can be easily identified, considering that DDES is based on the assumption that a balance between the production and destruction terms is achieved far from the wall (LES region where $f_{t2} \sim 0$),

$$C_{b1}\rho\tilde{S}\tilde{\nu} = C_{\omega_1}f_{\omega}\rho\left(\frac{\tilde{\nu}}{\tilde{d}}\right)^2. \tag{3.7}$$

where, $\tilde{\nu} = \nu_e/f_{v1}$, so

$$\nu_e = \frac{C_{b1}f_{v1}}{C_{\omega_1}f_{\omega}}\tilde{d}^2\tilde{S}. \tag{3.8}$$

Where $\nu_e$ is the kinematic eddy viscosity. Considering that it occurs in the LES region, $\tilde{d}$ can be replaced by $\Psi C_{DES}\Delta$ according to Eq. 3.2, so

$$\nu_e = \overbrace{\frac{C_{b1}f_{v1}\tilde{S}}{C_{\omega_1}f_{\omega}D_{sgs}\left(\tilde{u}_i\right)}\Psi^2}^{A_{SA}}\left(C_{DES}\Delta\right)^2 D_{sgs}\left(\tilde{u}_i\right) \tag{3.9}$$

$D_{sgs}\left(\tilde{u}_i\right)$ is introduced in order to force an LES-*like* turbulence model, which is usually represented by the following expression,

$$\nu_e = \left(C_S\Delta\right)^2 D_{sgs}\left(\tilde{u}_i\right). \tag{3.10}$$

Hence, there are strong similarity between Eq. 3.9 and Eq. 3.10, provided of course that the $A_{SA}$ expression behaves like a constant. This constant behaviour can be forced with the introduction of the counterbalancing term, $\Psi$. With this idea in mind, the necessity of introducing the $\Psi$ function comes naturaly. Considering that $\sqrt{A_{SA}C_{DES}^2}$ should mimic the well-known LES constant ($C_S \sim 0.15$ for *Smagorinsky* model, Eq. 3.45), the only parameters able to affect the $\nu_e$ transition for mitigating the GA are, $\Delta$ and $D_{sgs}\left(\tilde{u}_i\right)$. Therefore, most of the efforts of the scientific community for mitigating the GA, by means of reducing $\nu_e$, have been focused on these two parameters. An explanation of the standard and new techniques for mitigating GA is presented in section 3.2 and section 3.3.

A visual exemple of how the GA can affect the flow instabilities is presented in figure 3.1 (right), where the blue line shows a strong GA effect when it is compared with the DNS data. From a schematic point of view, it means that the oscillations at the beginning of the shear layer are not as energetic as they should naturaly be (left). Regarding the other coloured lines, they represent other DDES simulations which have been obtained by means of special mitigation strategies (these are analyzed in section 4).

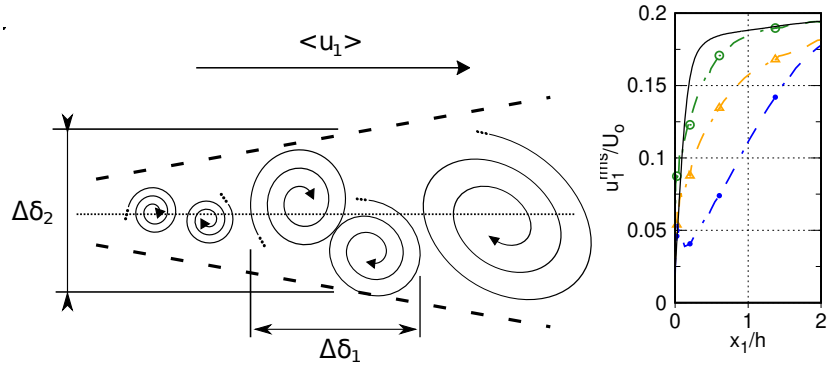


**Figure 3.1:** Schematic view of the proper triggering of the Kelvin-Helmholtz in the shear layer (left), and $u_1^{rms}$ (right) downstream of the flow in a BFS (comparison of a DNS, solid line, with various DDES simulations, coloured lines).

## 3.2 Standard Grey Area Mitigation Techniques

In the literature, there are two main strategies for leading the Grey Area [4]. One of them consists on using artificial oscillations in specific areas (zonal approach), whereas the other is based on reducing the subgrid-scale viscosity (Eq. 3.10) in particular areas, such as LES 2D flow regions. The second approach is preferable as it is aligned with the initial non-zonal philosophy. This reduction could be forced by any of the terms present in Eq. 4.1, as it has been commented in the previous section. Regarding $\Delta$, the idea of attributing kinematic sensitivity to this SLS coefficient was initially explored by Chauvet et al. [5]. Later on, Mockett et al. [4] developed

$$\tilde{\Delta}_\omega = \frac{1}{\sqrt{3}} \max_{n,m=1,\ldots,8} |l_n - l_m|, \tag{3.11}$$

defending the importance of using the maximum meaningful scale at each LES control volume. Where $\omega$ refers to the flow vorticity and $l = \omega/\|\omega\| \times r_n$, $r_n$ (n=1,...,8 for hexahedral cell) are the locations of the cell vertices. Comparing to $\Delta_{\max}$, which was the SLS proposed in the initial DES [2] and $DDES$, $\tilde{\Delta}_\omega$ was an important improvement in terms of mesh resiliency. Unfortunately, the $\nu_e$ at the Grey Area was still too high for triggering the flow instabilities in critical areas. Later on, Shur et al. [6] proposed $\Delta_{SLA}$ (Shear Layer Adapted),

$$\Delta_{SLA} = \tilde{\Delta}_\omega F_{KH}(\langle VTM \rangle) \tag{3.12}$$

$$VTM = \frac{|(S \cdot \omega) \times \omega|}{\omega^2 \sqrt{-Q_{\tilde{S}}}} \tag{3.13}$$

$$F_{KH}(\langle VTM \rangle) = \max\left(F_{KH}^{\min}, \min\left(F_{KH}^{\max}, F_{KH}^{\min} + \frac{F_{KH}^{\max} - F_{KH}^{\min}}{a_2 - a_1}\left(\langle VTM \rangle - a_1\right)\right)\right) \tag{3.14}$$

which was another SLS with the ability of switching off in 2D flow regions. It significantly contributed to the mitigation of the Grey Area. Where $\tilde{S}$ is the traceless part of the rate-of-strain tensor, $S = 1/2\left(\partial_j \tilde{u}_i + \partial_i \tilde{u}_j\right)$, *i.e.* $\tilde{S} = S - 1/3tr(S)I$. Note that for incompressible flows $tr(S) = \partial_i \tilde{u}_i = 0$, therefore, $\tilde{S} = S$. Finally, $Q_A$ refers to the second invariant of a second-order tensor A. Regarding $F_{KH}^{\max}$, $F_{KH}^{\min}$, $a_1$ and $a_2$, they were set to 1, 0.1, 0.15 and 0.3, respectively [6].

The influence of the differential operator, $D_{sgs}\left(\tilde{u}_i\right)$, into the *GA* mitigation was also reported in the literature. Some authors such as Fuchs et al. [7] and Probst et al. [8] investigated the impact of using the $\sigma - LES$ model 3.3.2, instead of Smagorinksy, due to its ability for switching off in $2D$ flow regions. Taking into account that unsteady 2D flows can not be considered as turbulent, the idea of deactivating the model in such regions looks reasonable. In fact, the $\Delta_{SLA}$ presented by Shur et al. [6] was also based on the same approach (Eq. 3.15), as the $\Delta$ turned to zero in 2D flow regions. Therefore, both strategies strenghten the importance of deactivating the turbulence model in 2D flow areas.

$$\begin{aligned} \nu_e &= \left(C_m \Delta_{SLA}\right)^2 D_{sgs}\left(\tilde{u}_i\right) \\ &= \left(C_m \tilde{\Delta}_\omega\right)^2 \left(F_{KH}(\langle VTM \rangle)^2 D_{sgs}\left(\tilde{u}_i\right)\right) \\ &= \left(C_m \tilde{\Delta}_\omega\right)^2 D_{sgs}^{2D}\left(\tilde{u}\right). \end{aligned} \tag{3.15}$$

## 3.3 New Grey Area Mitigation Techniques

### 3.3.1 Subgrid Length Scale - Least Square, $\Delta_{lsq}$

This subsection is a summary of the work published by Trias et al. [9].

#### Introduction

A new definition of the subgrid characteristic length is presented in this section. This flow-dependent length scale is based on the turbulent, or subgrid stress, tensor and its representations on different grids. The simplicity and mathematical properties suggest that it can be a robust definition that minimizes the effects of mesh anisotropies on simulation results. The performance of the proposed subgrid characteristic length was successfully tested for decaying isotropic turbulence and a turbulent channel flow using artificially refined grids [9]. Finally, a simple extension of the method for unstructured meshes is proposed. This last is tested in the simulations carried in chapter 4. Comparisons with existing subgrid characteristic length scales

show that the proposed definition is much more robust with respect to mesh anisotropies and has a great potential to be used in complex geometries where highly skewed (unstructured) meshes are present.

### Building a new subgrid length scale

Several approaches to compute the subgrid characteristic length, $\Delta$, can be found in the literature [9]. Despite these existing length scales, no consensus has been reached on how to define the subgrid characteristic length scale, particularly for (highly) anisotropic or unstructured grids. In this subsection, we therefore propose a new flow-dependent subgrid characteristic length scale that is based on the subgrid stress tensor, $\tau$, and its representations on different grids.

The subgrid characteristic length, $\Delta$, appears in a natural way when we consider the lowest-order approximation of the subgrid stress tensor, $\tau = \widetilde{\tilde{u}_i\tilde{u}_j} - \tilde{u}_i\tilde{u}_j$, *i.e.* the unclosed term in the filtered Navier-Stokes equations, Eq. (1.31). The approximation of the subgrid stress is obtained by approximating the residual velocity $u_i'' = u_i - \tilde{u}_i$.
To start, we restrict ourselves to one spatial direction and consider a box filter. The residue of the box filter can be related to the error of the midpoint rule for numerical integration, denoted by $\epsilon$ here. We have $\tilde{u}_1 = \int_{x_1-\Delta x_1/2}^{x_1+\Delta x_1/2} u_1(x_1)\,dx_1 = \Delta x_1 u_1(x_1) + \epsilon$ with $\epsilon = \frac{\Delta x_1^3}{24}\partial_1^2 u_1(c)$ where $c$ lies somewhere in between $x_1 - \Delta x_1/2$ and $x_1 + \Delta x_1/2$. An expression for the residue of the one-dimensional box filter is then obtained by dividing this error by $-\Delta x_1$ and adding $u_1$. Thus to lowest order we get $u_1'(x_1) = -\frac{\Delta x_1^2}{24}\partial_1^2 u_1(x_1) + \mathcal{O}(\Delta x_1^4)$.
On a three-dimensional, isotropic grid, *i.e.* $\Delta = \Delta x_1 = \Delta x_2 = \Delta x_3$, the above approximation of the residue becomes $u_i' = -\frac{\Delta^2}{24}\partial_j^2 u_i + \mathcal{O}(\Delta^4)$. With the help of this approximation it can be shown that the subgrid stress tensor is given by [10]

$$\tau(\tilde{u}_i) = \frac{\Delta^2}{12}\mathsf{G}\mathsf{G}^T + \mathcal{O}(\Delta^4). \tag{3.16}$$

The leading-order term of Eq. (3.16) is the gradient model proposed by Clark [10], where $\Delta$ denotes the filter length. Equation (3.16) has been derived for the box filter. However, it can be shown that the same result is obtained for any convolution filter having a symmetric kernel [11].
We stress that in the above derivation the grid is assumed to be isotropic, that is $\Delta = \Delta x_1 = \Delta x_2 = \Delta x_3$. For an anisotropic grid, we can postulate that the lowest-order approximation of the subgrid stress also provides us with $\tau(\tilde{u}_i) \approx \frac{\Delta^2}{12}\mathsf{G}\mathsf{G}^T$, that is, the approximation (1) depends quadratically on the velocity gradient, (2) is given by a symmetric tensor, (3) is invariant under a rotation of the coordinate system, and (4) is proportional to $\Delta^2$. Here, however, we do not yet know how to define the filter length, $\Delta$, because the grid is anisotropic. For the gradient model, however, we can define the filter length by mapping the anisotropic mesh onto an isotropic mesh. Therefore we consider the coordinate transformation $\hat{x}_1 = x_1/\Delta x_1$, $\hat{x}_2 = x_2/\Delta x_2$ and $\hat{x}_3 = x_3/\Delta x_3$. Expanding the subgrid stress as before, but now in the new, isotropic, coordinate

system $\hat{x}_1, \hat{x}_2, \hat{x}_3$ and applying the chain rule for differentiation yields

$$\tau(\tilde{u}_i) = \frac{1}{12}\mathsf{G}_\Delta \mathsf{G}_\Delta^T + \mathcal{O}(\Delta^4). \tag{3.17}$$

Here, the velocity gradient on the anisotropic grid is defined as

$$\mathsf{G}_\Delta \equiv \mathsf{G}\Delta, \tag{3.18}$$

where $\Delta$ is the second-order tensor containing the mesh information given by

$$\Delta \equiv (\Delta x_1, \Delta x_2, \Delta x_3). \tag{3.19}$$

Equation (3.17) does not require an explicit definition of the filter length, $\Delta$. In fact the filter length is hidden in $\mathsf{G}_\Delta$ and is not represented by a scalar but by the tensor $\Delta$. Since both Eq. (3.16) and Eq. (3.17) represent the lowest-order approximation of the subgrid stress, we can equate them and thus define the filter length $\Delta$ in Eq. (3.16) for anisotropic meshes. Here it may be remarked that we equate tensors, hence the equality is to be understood in least-square sense. This leads to the following flow-dependent definition of $\Delta$,

$$\Delta_{lsq} = \sqrt{\frac{\mathsf{G}_\Delta \mathsf{G}_\Delta^T : \mathsf{G}\mathsf{G}^T}{\mathsf{G}\mathsf{G}^T : \mathsf{G}\mathsf{G}^T}}. \tag{3.20}$$

We first remark that this length scale reduces to $\Delta$ on an isotropic mesh. Secondly, since $\Delta_{lsq}$ is formally based on the lowest-order approximation of the subgrid stress, we see it as a generic way to define the filter length. It can thus be applied in any turbulence model, not only in eddy-viscosity models. The characteristic length scale given by Eq. (3.20) depends on the velocity gradient, $\mathsf{G}$, so it is locally defined and frame invariant. Moreover, $\Delta_{lsq}$ is obviously sensitive to flow orientation.

Furthermore, it may be noted that the numerator in Eq.(3.20) can be viewed as the Frobenius norm of the tensor $\mathsf{G}^T\mathsf{G}\Delta$, *i.e.* $\mathsf{G}_\Delta \mathsf{G}_\Delta^T : \mathsf{G}\mathsf{G}^T = tr(\mathsf{G}_\Delta \mathsf{G}_\Delta^T \mathsf{G}\mathsf{G}^T) = tr(\mathsf{G}\Delta^2\mathsf{G}^T\mathsf{G}\mathsf{G}^T) = tr(\Delta\mathsf{G}^T\mathsf{G}(\Delta\mathsf{G}^T\mathsf{G})^T) = \Delta\mathsf{G}^T\mathsf{G} : \Delta\mathsf{G}^T\mathsf{G}$. Moreover, $\mathsf{G}\mathsf{G}^T : \mathsf{G}\mathsf{G}^T = tr(\mathsf{G}\mathsf{G}^T\mathsf{G}\mathsf{G}^T) = tr(\mathsf{G}^T\mathsf{G}\mathsf{G}^T\mathsf{G}) = \mathsf{G}^T\mathsf{G} : \mathsf{G}^T\mathsf{G}$, so we can also express $\Delta_{lsq}$ as

$$\Delta_{lsq} = \sqrt{\frac{\Delta\mathsf{G}^T\mathsf{G} : \Delta\mathsf{G}^T\mathsf{G}}{\mathsf{G}^T\mathsf{G} : \mathsf{G}^T\mathsf{G}}}. \tag{3.21}$$

From this definition it is obvious that $\Delta_{lsq}$ is positive and well bounded. Its applicability for unstructured meshes relies on the proper adaptation of the tensor $\Delta$. Regarding the computational cost of $\Delta_{lsq}$, this is relatively small when compared to the other flow-dependent length scales discussed in this document and special attention is only required for indeterminate forms of type $0/0$.

The inherent simplicity and mathematical properties of the proposed length scale, as well as its basis in representations of the subgrid stress tensor on different grids suggest that it can be a robust definition that minimizes the effects of mesh anisotropies on the performance of LES models.

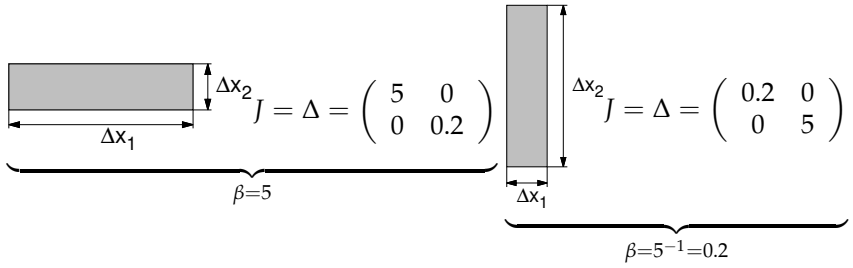


**Figure 3.2:** An example showing how the cell's shape is affected by the $\beta$ coefficient (5,1/5). The cell's volume is constant and equal to 1.

### Comparison of subgrid length scales for a 2D simplified flow

In this section, the performance of the new subgrid length scale, $\Delta_{lsq}$ is compared with $\tilde{\Delta}_\omega$ (see section 3.2). This study is assessed in a 2D simplified flow, based on the following parameters,

$$\begin{aligned} \Delta = & \begin{pmatrix} \Delta x & \\ & \Delta y \end{pmatrix} = \begin{pmatrix} \beta & \\ & \beta^{-1} \end{pmatrix}, \\ G = & \begin{pmatrix} \partial_1 u_1 & \partial_2 u_1 \\ \partial_1 u_2 & \partial_2 u_2 \end{pmatrix} = \begin{pmatrix} 0 & 1 \\ 1-2\omega & 0 \end{pmatrix}. \end{aligned} \tag{3.22}$$

Both mesh and velocity gradient are uniform in space and time. Even though turbulence is clearly a 3D phenomenon, this 2D analysis helps to understand the most essential properties of each SLS. Notice that the size of the control volume remains equal to unity (Eq. 3.22); therefore, $\Delta_{vol} = 1$, regardless of the value of $\beta$ (where $\Delta x_1$ is equal to $\beta$ and $\Delta x_2$ is $\beta^{-1}$). The effect of $\beta$ into the cell's shape can be observed in figure 3.2.
$\Delta_{lsq}$ is adapted depending on the flow behaviour and the cell orientation, providing completely different values in the simple shear ($\omega = 0.5$) case. In that situation, the spatial length scale reduces to $\beta^{-1} = \Delta x_2$, completely depending then on the mesh refinement at the highest gradient direction (usually in the streamwise orthogonal directions). It means that, $\Delta_{lsq}$ could lead to completely bad results in case of having an insuficient refinement. However, it is usually not the case if a Low-*Re* RANS models is used, as the refinement should be good enough for properly capturing the flow behaviour at the highest gradient regions (leading to meshes around $\sim x_2^+$). Issues could arise when High-*Re* RANS models are applied, as they use wall functions for representing the near wall behaviour and, thus, the extreme mesh refinement is no longer needed. In this situation, the use of $\Delta_{SLA}$ is more appropriate, as the $\Delta$ would be directly deactivated in $2D$ flow regions. In contrast to $\Delta_{lsq}$, $\tilde{\Delta}_\omega = \sqrt{(\beta^2 + \beta^{-2})/3}$ only depends on the $\beta$ ratio, but is not sensitive neither the flow behaviour nor the volume rotation (the same results are obtained with $\beta = 5$ and $\beta = 1/5$). It is worth noting here that the reason why the $\Delta_{SLA}$ performance has not been included in figure 3.3, is because it is deactivated in 2D flow.

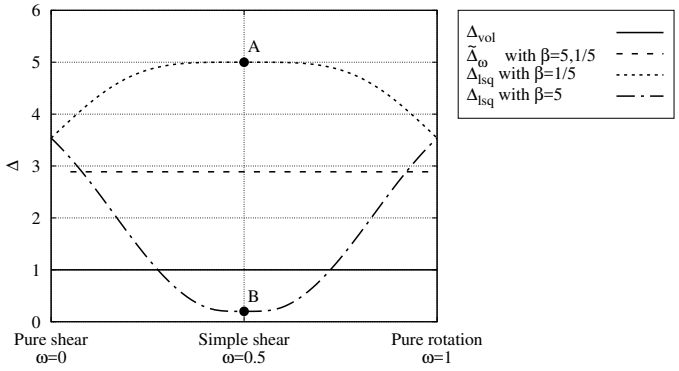


**Figure 3.3:** Comparison between $\tilde{\Delta}_\omega$ and $\Delta_{lsq}$ for the simple 2D flow defined in Eq. 3.22 with different values of $\beta = 1/5, 1/2, 2, 5, 10$

### Jacobian-based extension for unstructured meshes

In Section 3.3.1 a new method to compute the subgrid characteristic length has been proposed. Although it has been derived in the context of Cartesian meshes, the idea can be extended to unstructured meshes by noticing that it basically consists in projecting the leading term of the Taylor series expansion of $\tau$ (see Eq. 3.17) onto the basic gradient model (see Eq. 3.16).
For non-uniform Cartesian grids we considered the coordinate transformation $\hat{x}_1 = x_1/\Delta x_1$, $\hat{x}_2 = x_2/\Delta x_2$ and $\hat{x}_3 = x_3/\Delta x_3$. This leaded to a new, isotropic, coordinate system $\hat{x}_i$. Then, applying the chain rule for differentiation yielded the approximation of the subgrid stress tensor of Eq.(3.17). More generally, let $\xi_i(x_i)$ be a monotonic differentiable function which defines a mapping from the physical space in the $i$-direction, $x_i$, to the so-called computational space, $\xi_i$. Using the chain rule we obtain

$$\frac{\partial \phi}{\partial x_i} = \frac{\partial \phi}{\partial \xi_i}\frac{d\xi_i}{dx_i} = \frac{1}{J_i}\frac{\partial \phi}{\partial \xi_i}, \tag{3.23}$$

where $J_i$ is the Jacobian of the transformation $x_i \to \xi_i$. Here, no summation over $i$ is implied. Recalling that $[\mathsf{G}]_{ij} = \partial_j u_i$, the leading term of $\tau$ can be written more compactly as follows

$$\tau = \frac{1}{12}\mathsf{G}_\xi \mathsf{G}_\xi^T + \mathcal{O}(\overline{\Delta}^4), \tag{3.24}$$

where the gradient in the mapped space $\boldsymbol{\xi}$ is represented by

$$\mathsf{G}_\xi = \mathsf{G}\mathsf{J} \tag{3.25}$$

and $\mathsf{J}$ is the Jacobian of the transformation $\boldsymbol{x} \to \boldsymbol{\xi}$. Notice that this first term is generic for all practical filters [11] in the context of LES, *i.e.* filters with a Fourier transform

starting with $\hat{G}(k) = 1 - k^2\overline{\Delta}/2 + \mathcal{O}(k^4)$. At the discrete level, for a Cartesian grid the filter length in each direction is taken equal to the mesh size in the same direction, *i.e.* $\overline{\Delta}_i = \Delta x_i$. In this case, $\mathsf{J} = \Delta$ and $\mathsf{G}_{\bar{\xi}} = \mathsf{G}_{\Delta} = \mathsf{G}\Delta$; therefore, the general expression given in Eq. (3.24) reduces to Eq. (3.17) for non-uniform Cartesian meshes and to the well-known gradient model [10] given in Eq. (3.16) for uniform grid spacings.

At this point, it becomes clear that the extension of the new subgrid characteristic length $\Delta_{lsq}$ (see Eq. 3.20) in section 3.3.1 for unstructured meshes relies on the computation of the Jacobian, $\mathsf{J}$, on such grids. It is important to note that the gradient tensor, $\mathsf{G}$, is actually being computed in any LES code. Below, the method to compute the Jacobian, $\mathsf{J}$, is solely based on the discrete gradient operator; therefore, it can be easily applied to any existing code. Namely, using matrix-vector notation, the discrete gradient operator is given by a block matrix

$$\boldsymbol{G}\boldsymbol{\phi}_h = \begin{pmatrix} \boldsymbol{G}_{x_1} \\ \boldsymbol{G}_{x_2} \\ \boldsymbol{G}_{x_3} \end{pmatrix} \boldsymbol{\phi}_h, \tag{3.26}$$

where $\boldsymbol{\phi}_h = (\phi_1, \phi_2, ..., \phi_n)^T \in^n$, $n$ is the number of unknowns in our domain and $\boldsymbol{G}_{x_i}$ represent the discrete gradient operator for each spatial direction.

As a preview of things, we first consider the discretization of the gradient operator, $\boldsymbol{G}$, in one spatial direction with periodic boundary conditions. Let us consider three values of a smooth function $\phi(x)$: $\phi_{i-1} = \phi(x_{i-1})$, $\phi_i = \phi(x_i)$ and $\phi_{i+1} = \phi(x_{i+1})$ with $x_{i-1} = x_i - \Delta x_1$ and $x_{i+1} = x_i + \Delta x_1$. By a simple combination of Taylor series expansions of $\phi(x)$ around $x = x_i$, the following well-known second-order accurate approximation of the derivative follows

$$\frac{\partial \phi(x_i)}{\partial x} \approx \frac{\phi_{i+1} - \phi_{i-1}}{2\Delta x_1}. \tag{3.27}$$

Then with a uniformly meshed periodic direction, $\boldsymbol{G}_{x_1}$ results into a skew-symmetric circulant matrix of the form

$$\boldsymbol{G}_{x_1} = \frac{1}{2\Delta x_1}\text{circ}(0, 1, 0, \cdots, 0, -1). \tag{3.28}$$

Thus, eigenvalues of $\boldsymbol{G}_{x_1}$ lie on the imaginary axis, $\lambda_k^{\boldsymbol{G}_{x_1}} \in \mathbb{I}$. Then, the eigenvalues can be easily bounded with the help of the Gershgorin circle theorem, *i.e.* $|\lambda_k^{\boldsymbol{G}_{x_1}}| \leq 1/\Delta x_1$. Notice that the upper bound exactly corresponds to the Jacobian, $J_{x_1} = 1/\Delta x_1$, of the mapping from the physical to the computational space for Cartesian grids. This idea can be extended to any grid or numerical method if we consider that, at the

discrete level, the Jacobian, $\boldsymbol{J}$, is as a diagonal matrix

$$\boldsymbol{J} \equiv \begin{pmatrix} \boldsymbol{J}_{x_1} & & \\ & \boldsymbol{J}_{x_2} & \\ & & \boldsymbol{J}_{x_3} \end{pmatrix}, \tag{3.29}$$

that, like in the Cartesian case, guarantees that the spectral norm of the gradient in the so-called computational space, $\boldsymbol{\mathcal{G}} \equiv \boldsymbol{J}\boldsymbol{G} = (\boldsymbol{\mathcal{G}}_{x_1}, \boldsymbol{\mathcal{G}}_{x_2}, \boldsymbol{\mathcal{G}}_{x_3})^T$ is equal to or smaller than unity, *i.e.* $\|\boldsymbol{\mathcal{G}}\|_2 \leq 1$. This condition can easily be realized by using the Gershgorin circle theorem. Namely,

$$|\lambda_i^{\boldsymbol{\mathcal{G}}_x} - \mathcal{G}_{ii}^{x_1}| \leq \sum_{j \neq i} |\mathcal{G}_{ij}^{x_1}| \quad \text{where} \quad \mathcal{G}_{ij}^{x_1} = \mathcal{J}_{ii}^{x_1} G_{ij}^{x_1}, \tag{3.30}$$

and $\mathcal{G}_{ij}^{x_1} = [\boldsymbol{\mathcal{G}}_{x_1}]_{i,j}$, $G_{ij}^{x_1} = [\boldsymbol{G}_{x_1}]_{i,j}$ and $\mathcal{J}_{ij}^{x_1} = [\boldsymbol{J}_{x_1}]_{i,j}$ are the coefficients of the matrices $\boldsymbol{\mathcal{G}}_{x_1}$, $\boldsymbol{G}_{x_1}$ and $\boldsymbol{J}_{x_1}$, respectively. Since $\boldsymbol{G}$ (also $\boldsymbol{\mathcal{G}}$) is usually a zero-diagonal matrix, *i.e.* $G_{ii} = 0$ (summation not implied), the condition $\|\boldsymbol{\mathcal{G}}\|_2 \leq 1$ simplifies to

$$|\lambda_i^{\boldsymbol{\mathcal{G}}_{x_1}}| \leq \sum_{j \neq i} |\mathcal{G}_{ij}^{x_1}| \leq 1 \quad \forall i = 1, \ldots, n, \tag{3.31}$$

where $n$ is the number of unknowns in our domain. Finally, recalling that the Jacobian must be positive, $\mathcal{J}_{ii} > 0$, and extending the previous analysis to the $y$ and $z$ directions, the following definition for the Jacobian

$$\mathcal{J}_{ii}^{x_1} \equiv \frac{1}{\sum_{j \neq i} |G_{ij}^{x_1}|} \qquad \mathcal{J}_{ii}^{x_2} \equiv \frac{1}{\sum_{j \neq i} |G_{ij}^{x_2}|} \qquad \mathcal{J}_{ii}^{x_3} \equiv \frac{1}{\sum_{j \neq i} |G_{ij}^{x_3}|}, \tag{3.32}$$

guarantees that inequalities (3.31) are always satisfied. Here, no summation over $i$ is implied. Therefore, the spectral norm of $\boldsymbol{G}_\xi$ is equal to or smaller than unity, *i.e.* $\|\boldsymbol{\mathcal{G}}\|_2 \leq 1$. In this way, the local Jacobian for the node $i$, $\mathsf{J}_i$, is given by

$$\mathsf{J}_i = \begin{pmatrix} \mathcal{J}_{ii}^{x_1} & & \\ & \mathcal{J}_{ii}^{x_2} & \\ & & \mathcal{J}_{ii}^{x_3} \end{pmatrix}. \tag{3.33}$$

Notice that the definitions of the Jacobian given in Eq.(3.32) are solely based on the coefficients of the discrete gradient operator, $\boldsymbol{G}$. Therefore, there is no restriction regarding the type of grid and the numerical method. Moreover, it is worth to notice that for a Cartesian uniform mesh, this formula reduces to $\mathsf{J} = (\Delta x_1, \Delta x_2, \Delta x_3)$ like the definition of $\Delta$ given in Eq.(3.19).

In this way, the subgrid characteristic length scale proposed in Section 3.3.1 is straightforwardly extended to unstructured meshes by simply replacing $\Delta$ in Eq.(3.20) by the local Jacobian, $\mathsf{J}_i$, defined in Eqs.(3.32) and (3.33).

### 3.3.2 Turbulence Models, *S3PQR*

This subsection is a summary of the work published by Trias et al. [12].

#### Introduction

Eddy-viscosity models rely on differential operators that should properly detect different flow configurations (laminar and 2D flows, near-wall behavior, transitional regime...). Most of them are based on the combination of invariants of a symmetric tensor that depends on the gradient of the resolved velocity field, $\mathsf{G} = \partial_j \tilde{u}_i$. In this subsection, models are presented within a framework consisting of a 5D phase space of invariants. In this way, new models can be constructed by imposing appropriate restrictions in this space. For instance, considering the three invariants $P_{\mathsf{GG}^T}$, $Q_{\mathsf{GG}^T}$ and $R_{\mathsf{GG}^T}$ of the tensor $\mathsf{GG}^T$, and imposing the proper cubic near-wall behavior, *i.e.* $\nu_e = \mathcal{O}(x_2^3)$, it was deduced that the eddy-viscosity is given by $\nu_e = (C_{s3pqr}\Delta)^2 P_{\mathsf{GG}^T}^p Q_{\mathsf{GG}^T}^{-(p+1)} R_{\mathsf{GG}^T}^{(p+5/2)/3}$. Moreover, only $R_{\mathsf{GG}^T}$-dependent models, *i.e.* $p > -5/2$, switch off for 2D flows. This is an important feature for Hybrid RANS-LES models as it contributes to the mitigation of the Grey Area in free shear layer regions, instabilizing the flow in a natural manner. For instance, the family of *S3PQR* and the $\sigma$-model consider this interesting property.

#### Theory

The essence of turbulence are the smallest scales of motion. They result from a subtle balance between convective transport and diffusive dissipation. Numerically, if the grid is not fine enough, this balance needs to be restored by a turbulence model. The success of a turbulence model depends on the ability to capture well this (im)balance. In this regard, many eddy-viscosity models for LES have been proposed in the last decades [13,14]. In order to be frame invariant, most of them rely on differential operators that are based on the combination of invariants of a symmetric second-order tensor (with the proper scaling factors). To make them locally dependent such tensors are derived from the gradient of the resolved velocity field, $\mathsf{G} \equiv \partial_j \tilde{u}_i$. This is a second-order traceless tensor, $tr(\mathsf{G}) = \partial_i \tilde{u}_i = 0$. Therefore, in 3D, this $3 \times 3$ tensor contains 8 independent elements and it can be characterized by 5 invariants (3 scalars are required to specify the orientation in 3D). Following the same criterion that in [15,16], this set of five invariants can be defined as follows

$$\{Q_{\mathsf{G}}, R_{\mathsf{G}}, Q_{\mathsf{S}}, R_{\mathsf{S}}, V^2\}, \tag{3.34}$$

where $Q_{\mathsf{A}} = 1/2\{tr^2(\mathsf{A}) - tr(\mathsf{A}^2)\}$ and $R_{\mathsf{A}} = det(\mathsf{A}) = 1/6\{tr^3(\mathsf{A}) - 3tr(\mathsf{A})tr(\mathsf{A}^2) + 2tr(\mathsf{A}^3)\}$ represent the second and third invariant of the second-order tensor $\mathsf{A}$, respectively. Moreover, the first invariant of $\mathsf{A}$ will be denoted as $P_{\mathsf{A}} = tr(\mathsf{A})$. Notice that if $\mathsf{A}$ is traceless, $tr(\mathsf{A}) = 0$, these formulae reduce to $P_{\mathsf{A}} = 0$, $Q_{\mathsf{A}} = -1/2tr(\mathsf{A}^2)$ and $R_{\mathsf{A}} = det(\mathsf{A}) = 1/3tr(\mathsf{A}^3)$, respectively. Finally, $V^2 = 4(tr(\mathsf{S}^2\Omega^2) - 2Q_{\mathsf{S}}Q_{\Omega})$, where $\mathsf{S} = 1/2(\mathsf{G} + \mathsf{G}^T)$ and $\Omega = 1/2(\mathsf{G} - \mathsf{G}^T)$ are the symmetric and the skew-symmetric parts of the gradient tensor, $\mathsf{G}$. Notice that all these tensors are also traceless, $tr(\mathsf{S}) = tr(\Omega) = tr(\mathsf{G}) = 0$. The following relations between their principal invariants can be easily obtained

$$P_{\mathsf{G}} = P_{\mathsf{S}} = P_{\Omega} = 0, \tag{3.35}$$
$$Q_{\mathsf{G}} = Q_{\mathsf{S}} + Q_{\Omega}, \tag{3.36}$$
$$R_{\mathsf{G}} = R_{\mathsf{S}} + tr(\Omega^2\mathsf{S}), \qquad R_{\Omega} = 0. \tag{3.37}$$

Starting from the classical Smagorinsky model [17], most of the eddy-viscosity models for LES are based on invariants of second-order tensors that are derived from the gradient tensor, G. Therefore, it seems natural to re-write them in terms of the 5D phase space defined in (3.34). This is addressed in the next section. However, for convenience some other important invariants (or relations) in the context of eddy-viscosity models for LES are defined before. Namely,

$$tr(\mathsf{G}\mathsf{G}^T) = tr(\mathsf{S}^2) - tr(\Omega^2) = 2(Q_{\Omega} - Q_{\mathsf{S}}), \tag{3.38}$$
$$tr(\mathsf{S}^2\Omega^2) = 1/8(tr(\mathsf{G}^4) - tr(\mathsf{G}\mathsf{G}^T\mathsf{G}\mathsf{G}^T)) = 1/8(2Q_{\mathsf{G}}^2 - tr(\mathsf{G}\mathsf{G}^T\mathsf{G}\mathsf{G}^T)), \tag{3.39}$$
$$tr(\mathsf{S}^2\Omega^2) = V^2/4 + 2Q_{\mathsf{S}}Q_{\Omega}, \tag{3.40}$$
$$tr(\tilde{\mathsf{A}}^2) = tr(\mathsf{A}^2) - 1/3tr^2(\mathsf{A}), \tag{3.41}$$

where $\tilde{\mathsf{A}} = \mathsf{A} - 1/3tr(\mathsf{A})$ denotes the traceless part of tensor A. In this context, it is also useful to define the three eigenvalues, $\lambda_1 \geq \lambda_2 \geq \lambda_3$ of A. They are solutions of the characteristic equation

$$det(\lambda - \mathsf{A}) = \lambda^3 - P_{\mathsf{A}}\lambda^2 + Q_{\mathsf{A}}\lambda - R_{\mathsf{A}} = 0, \tag{3.42}$$

where

$$P_{\mathsf{A}} = \lambda_1 + \lambda_2 + \lambda_3; \qquad Q_{\mathsf{A}} = \lambda_1\lambda_2 + \lambda_1\lambda_3 + \lambda_2\lambda_3; \qquad R_{\mathsf{A}} = \lambda_1\lambda_2\lambda_3, \tag{3.43}$$

whereas for traceless tensors it simplifies to

$$P_{\tilde{\mathsf{A}}} = 0; \qquad Q_{\tilde{\mathsf{A}}} = -1/2\,(\lambda_1\lambda_1 + \lambda_2\lambda_2 + \lambda_3\lambda_3)\,; \qquad R_{\tilde{\mathsf{A}}} = \lambda_1\lambda_2\lambda_3. \tag{3.44}$$

## A unified framework for eddy-viscosity models

### Smagorinsky model

The Smagorinsky model [17] can be written in terms of the above-defined invariants as follows

$$\nu_e^{Smag} = (C_S\Delta)^2|\mathsf{S}(\tilde{u}_i)| = 2(C_S\Delta)^2(-Q_{\mathsf{S}})^{1/2}, \tag{3.45}$$

where $C_S$ is the Smagorinsky constant, $\Delta$ is the filter length (related with the local grid size) and $|\mathsf{S}| = (2\mathsf{S} : \mathsf{S})^{1/2}$. Notice that the Frobenius norm of S is $\mathsf{S} : \mathsf{S} = tr(\mathsf{S}^2) = -2Q_{\mathsf{S}}$.

### Vreman's model

The Vreman's model [18] is based on the ratio between the second and the first invariant of the tensor $\mathsf{G}\mathsf{G}^T$. With the help of the identity (3.38), the latter can be written as follows

$$P_{\mathsf{G}\mathsf{G}^T} = tr(\mathsf{G}\mathsf{G}^T) = 2(Q_{\Omega} - Q_{\mathsf{S}}), \tag{3.46}$$

whereas the former is given by $Q_{\mathsf{G}\mathsf{G}^T} = 1/2\{tr^2(\mathsf{G}\mathsf{G}^T) - tr(\mathsf{G}\mathsf{G}^T\mathsf{G}\mathsf{G}^T)\}$. Then, with the help of the identities (3.38) and (3.39), $Q_{\mathsf{G}\mathsf{G}^T}$ can be expressed in terms of more basic invariants

$$Q_{\mathsf{G}\mathsf{G}^T} = 2(Q_\Omega - Q_\mathsf{S})^2 - Q_\mathsf{G}^2 + 4tr(\mathsf{S}^2\Omega^2), \tag{3.47}$$

and simplified further using (3.36) and (3.40)

$$Q_{\mathsf{G}\mathsf{G}^T} = V^2 + Q_\mathsf{G}^2. \tag{3.48}$$

In the Vreman's model the eddy-viscosity is given by the following expression

$$\nu_e^{Vr} = (C_{Vr}\Delta)^2 \left(Q_{\mathsf{G}\mathsf{G}^T}/P_{\mathsf{G}\mathsf{G}^T}\right)^{1/2}. \tag{3.49}$$

Finally, plugging identities (3.46) and (3.48) leads to

$$\nu_e^{Vr} = (C_{Vr}\Delta)^2 \left(\frac{V^2 + Q_\mathsf{G}^2}{2(Q_\Omega - Q_\mathsf{S})}\right)^{1/2}. \tag{3.50}$$

**$\sigma$-model**

Even more recently, Nicoud [19] proposed a new eddy-viscosity model. In this case, it is based on the singular values of the tensor $\mathsf{G}$. Namely,

$$\nu_e^{\sigma} = (C_\sigma\Delta)^2 \frac{\sigma_3(\sigma_1 - \sigma_2)(\sigma_2 - \sigma_3)}{\sigma_1^2}, \tag{3.51}$$

where $\sigma_i$ are the three singular eigenvalues of $\mathsf{G}$, *i.e.* $\sigma_i = \sqrt{\lambda_i}$ where $\lambda_i$ is an eigenvalue of $\mathsf{G}\mathsf{G}^T$, and $\sigma_1 \geq \sigma_2 \geq \sigma_3$. Hence, the eigenvalues of $\mathsf{G}\mathsf{G}^T$ need to be determined. To do so, firstly we need to compute the three invariants of $\mathsf{G}\mathsf{G}^T$: the first two invariants, $P_{\mathsf{G}\mathsf{G}^T}$ and $Q_{\mathsf{G}\mathsf{G}^T}$, are respectively given by the identities (3.46) and (3.48), whereas the third invariant of $\mathsf{G}\mathsf{G}^T$ follows straightforwardly

$$R_{\mathsf{G}\mathsf{G}^T} = det(\mathsf{G}\mathsf{G}^T) = det(\mathsf{G})det(\mathsf{G}^T) = R_\mathsf{G}^2. \tag{3.52}$$

Finally, the eigenvalues of $\mathsf{G}\mathsf{G}^T$ are obtained by solving its characteristic equation. Hence, the formula for the eddy-viscosity given in Eq.(3.51) can be computed in terms of the following four basic invariants: $Q_\mathsf{G}$, $Q_\mathsf{S}$, $V^2$ and $R_\mathsf{G}$. However, it requires the numerical solution of a cubic equation.

*S3PQR*-**model**

At this point it is interesting to observe that new models can be derived by imposing restrictions on the differential operators they are based on. For instance, let us consider models that are based on the invariants of the tensor $\mathsf{G}\mathsf{G}^T$

$$\nu_e = (C_{s3pqr}\Delta)^2 P_{\mathsf{G}\mathsf{G}^T}^p Q_{\mathsf{G}\mathsf{G}^T}^q R_{\mathsf{G}\mathsf{G}^T}^r, \tag{3.53}$$

where $P_{\mathsf{G}\mathsf{G}^T}$, $Q_{\mathsf{G}\mathsf{G}^T}$ and $R_{\mathsf{G}\mathsf{G}^T}$ are given by Eqs.(3.46), (3.48) and (3.52), respectively. This tensor is proportional to the gradient model [10] given by the leading term of the Taylor series expansion

of the subgrid stress tensor $\tau(\tilde{u}_i) = (\Delta^2/12)\mathsf{G}\mathsf{G}^T + \mathcal{O}(\Delta^4)$. The local dissipation of gradient model is then proportional to $-\mathsf{G}\mathsf{G}^T : \mathsf{S} = -tr(\mathsf{G}\mathsf{G}^T\mathsf{S}) = 1/3(tr(\mathsf{G}^3) - 4tr(\mathsf{S}^3)) = R_\mathsf{G} - 4R_\mathsf{S}$. Hence, the local dissipation introduced by the model, *i.e.* $(\Delta^2/12)(R_\mathsf{G} - 4R_\mathsf{S})$, can also take negative values; therefore, the gradient model cannot be used as a standalone LES model, since it produces a finite time blow-up of the kinetic energy [20]. From the asymptotic near-wall behavior of the basic invariants it is easy to deduce that $P_{\mathsf{G}\mathsf{G}^T}$, $Q_{\mathsf{G}\mathsf{G}^T}$ and $R_{\mathsf{G}\mathsf{G}^T}$ scale 0, 2 and 6, and their units are $[T^{-2}]$, $[T^{-4}]$ and $[T^{-6}]$, respectively. Then, the exponents $p$, $q$ and $r$ in Eq.(3.53), must satisfy the following equations

$$-6r - 4q - 2p = -1; \qquad 6r + 2q = s, \tag{3.54}$$

to guarantee that the differential operator has units of frequency, *i.e.* $[P^p_{\mathsf{G}\mathsf{G}^T} Q^q_{\mathsf{G}\mathsf{G}^T} R^r_{\mathsf{G}\mathsf{G}^T}] = [T^{-1}]$ and a slope $s$ for the asymptotic near-wall behavior, *i.e.* $s$. The forcing of the proper cubic near-wall behavior [21], *i.e.* $s = 3$, leads to a family of $p$-dependent eddy-viscosity models,

$$\nu_e^{S3PQR} = (C_{s3pqr}\Delta)^2 P^p_{\mathsf{G}\mathsf{G}^T} Q^{-(p+1)}_{\mathsf{G}\mathsf{G}^T} R^{(p+5/2)/3}_{\mathsf{G}\mathsf{G}^T}. \tag{3.55}$$

Hereafter, this family of models will be referred as *S3PQR*-model. Restricting ourselves to solutions involving only two invariants of $\mathsf{G}\mathsf{G}^T$ three models are found. Namely,

$$\nu_e^{S3PQ} = (C_{s3pq}\Delta)^2 P^{-5/2}_{\mathsf{G}\mathsf{G}^T} Q^{3/2}_{\mathsf{G}\mathsf{G}^T}, \tag{3.56}$$

$$\nu_e^{S3PR} = (C_{s3pr}\Delta)^2 P^{-1}_{\mathsf{G}\mathsf{G}^T} R^{1/2}_{\mathsf{G}\mathsf{G}^T}, \tag{3.57}$$

$$\nu_e^{S3QR} = (C_{s3qr}\Delta)^2 Q^{-1}_{\mathsf{G}\mathsf{G}^T} R^{5/6}_{\mathsf{G}\mathsf{G}^T}, \tag{3.58}$$

for $p = -5/2$, $p = -1$ and $p = 0$, respectively. Considering that only $R_{\mathsf{G}\mathsf{G}^T}$-dependent models, *i.e.* $p > -5/2$, switch off for 2D flows, and the importance of this feature for mitigating the Grey Area in Hybrid RANS-LES models, the *S3QR* and *S3PR* are desirable. Moreover, the fact that $r$ is higher in *S3QR* than *S3PR*, makes *S3QR* the choice made, as it reduces $\nu_e$ in 2D flow areas, triggering instabilities in free shear layers.

# References


[1] Charles Mockett. A comprehensive study of detached-eddy simulation. *PhD Thesis: TU Berlin*, 2009.

[2] P. R. Spalart, W-H Jou, M. Strelets, and S. Allmaras. Comments on the Feasibility of LES for Wings, and on a Hybrid RANS/LES Approach, 1997.

[3] P. R. Spalart, S. Deck, M. L. Shur, K. D. Squires, M. Kh Strelets, and A. Travin. A new version of detached-eddy simulation, resistant to ambiguous grid densities. *Theoretical and Computational Fluid Dynamics*, 20(3):181–195, 2006.

[4] Charles Mockett, Marian Fuchs, Andrey Garbaruk, Michael Shur, Philippe Spalart, Michael Strelets, Frank Thiele, and Andrey Travin. Two Non-zonal Approaches to Accelerate RANS to LES Transition of Free Shear Layers in DES. In *Progress in Hybrid RANS-LES Modelling*, pages 187–201, Cham, 2015. Springer International Publishing.

[5] Nicolas Chauvet, Sebastien Deck, and Laurent Jacquin. Zonal detached eddy simulation of a controlled propulsive jet. *AIAA Journal*, 45(10):2458–2473, 2007.

[6] Mikhail L. Shur, Philippe R. Spalart, Mikhail Kh Strelets, and Andrey K. Travin. An Enhanced Version of DES with Rapid Transition from RANS to LES in Separated Flows. *Flow, Turbulence and Combustion*, 95(4), 2015.

[7] M. Fuchs, J. Sesterhenn, F. Thiele, and C. Mockett. Assessment of novel DES approach with enhanced SGS modelling for prediction of separated flow over a delta wing. In *22nd AIAA Computational Fluid Dynamics Conference*, 2015.

[8] A. Probst, D. Schwamborn, A. Garbaruk, E. Guseva, M. Shur, M. Strelets, and A. Travin. Evaluation of grey area mitigation tools within zonal and non-zonal RANS-LES approaches in flows with pressure induced separation. *International Journal of Heat and Fluid Flow*, 2017.

[9] F X Trias, A. Gorobets, and A. Oliva. A new subgrid characteristic length for large-eddy simulation. *Physics of Fluids*, 115109, 2017.

[10] J. H. Ferziger R. A. Clark and W. C. Reynolds. Evaluation of subgrid-scale models using an accurately simulated turbulent flow. *Journal of Fluid Mechanics*, 91:1–16, 1979.

[11] A. A. Wray O. V. Vasilyev G. S. Winckelmans and H. Jeanmart. Evaluation of subgrid-scale models using an accurately simulated turbulent flow. *Physics of Fluids*, 13(5):1385–1403, 2001.

[12] F X Trias, D. Folch, A. Gorobets, and A. Oliva. Building proper invariants for eddy-viscosity subgrid-scale models. *Physics of Fluids*, 27(6), 2015.

[13] T. Iliescu L. C. Berselli and W. Layton. In *Mathematics of Large Eddy Simulation of Turbulent Flows*. Springer, 2006.

[14] P. Sagaut. In *Large eddy simulation for incompressible flows: an introduction*. Springer, 2005.

[15] B. J. Cantwell. Exact solution of a restricted Euler equation for the velocity gradient tensor. *Physics of Fluids A*, 4:782–793, 1992.

[16] M. S. Chong J. Martin, A. Ooi and J. Soria. Dynamics of the velocity gradient tensor invariants in isotropic turbulence. *Physics of Fluids*, 10:2336–2346, 1998.

[17] J. Smagorinsky. General Circulation Experiments with the Primitive Equations. *Journal of Fluid Mechanics*, 91:99–164, 1963.

[18] A. W. Vreman. An eddy-viscosity subgrid-scale model for turbulent shear flow: Algebraic theory and applications. *Physics of Fluids*, 16(10):3670–3681, 2004.

[19] O. Cabrit S. Bose F. Nicoud, H. B. Toda and J. Lee. Using singular values to build a subgrid-scale model for large eddy simulations. *Physics of Fluids*, 23(8):085106, 2011.

[20] B. Geurts B. Vreman and H. Kuerten. Large-eddy simulation of the temporal mixing layer using the Clark model. *Theoretical and Computational Fluid Dynamics*, 8:309–324, 1996.

[21] D. R. Chapman and G. D. Kuhn. The limiting behaviour of turbulence near a wall. *Journal of Fluid Mechanics*, 170:265–295, 1986.

# 4

# Assessment of the new techniques for mitigating the Grey Area in DDES models

Main contents of this chapter have been submitted to *AIAA Journal*:

A. Pont-Vílchez, A. Duben, A. Gorobets, A. Revell, A. Oliva and F.X. Trias . New strategies for mitigating the Grey Area in DDES models. *AIAA Journal* (submitted).

**Abstract.** The new approach presented in the previous section for mitigating the Grey Area numerical issue, is used in two classic cases and compared with standard methodologies in both incompressible and compressible flow. Moreover, two different codes have been used, *OpenFOAM* and *NOISEtte*, for cross-validation purposes. Encouraging results have been obtained with the new approach, supporting its suitability as a good candidate for addressing the *Grey Area* numerical issue.

## 4.1 Introduction

During the last decades, numerical simulations have become an essential tool for every-day understanding and prediction of the flow behavior in industrial applications. Reynolds-Averaged Navier-Stokes (RANS) models have been, and continue to be, widely used due to their cost-effective nature, but their limitations for predicting complex flow motions and

providing unsteady data are also well-known. Moreover, the routine use of more accurate numerical methodologies such as Large Eddy Simulation (LES) usually require a heavy amount of computational resources, so its use remains relatively low; limited to industrial sectors and research cases where extra accuracy requirements justify the additional expense. In this regard, a set of hybrid RANS-LES methodologies were specifically designed for circumventing the issues mentioned above, modelling the boundary layer using RANS and simulating the unsteady flow away from the wall using LES based methods.
In this context, DDES [1] is one of the most widely used hybrid models, due to its user-friendly non-zonal approach and its proven success in a range of applications, particularly for cases where RANS becomes unreliable, such as massive flow separation. In contrast to the original version of Detached Eddy Simulation (DES) [2], the DDES non-zonal approach not relies only on the mesh for defining the RANS and LES regions, but also on the flow field, by means of the shielding function, $f_d$. However, while some important weaknesses of the initial DES version where resolved, some others remain open. First, the flow separation due to adverse pressure gradient depends mainly on the underlying RANS model, with associated weaknesses and case dependency. The slow transition from RANS to LES also leads to unphysical results, delaying the natural development of flow instabilities free shear layers. This numerical issue is known as the Grey Area ($GA$). While a number of developments have been proposed to address the aforementioned shortcomings, some general issues remain unclosed.
The present chapter is focused on diminishing the unphysical delay in transition for the RANS to LES region, improving the accuracy of the resolved instabilities in such areas. An example of previous efforts to overcome these issues is the extensive work presented by Mockett et al. [3] where two different strategies were described. First, reducing the eddy-viscosity,

$$\nu_{sgs} = \left(C_{sgs}\Delta\right)^2 D_{sgs}\left(\tilde{u}_i\right), \tag{4.1}$$

in transition areas by either diminishing the Subgrid Length Scale (SLS), $\Delta$, or the differential operators, $D_{sgs}\left(\tilde{u}_i\right)$, or both. Second, introducing artificial oscillations for triggering turbulence in the region of interest. Even though both strategies deal with the delay problem, the first one is preferable as it is consistent with the non-zonal DES ideology.
In this regard, a new SLS was introduced [3], sensitive to the flow kinematics and defending the importance of using the maximum meaningful scale at each LES control volume,

$$\tilde{\Delta}_\omega = \frac{1}{\sqrt{3}} \max_{n,m=1,\ldots,8} |\boldsymbol{l}_n - \boldsymbol{l}_m|. \tag{4.2}$$

Where $\boldsymbol{l} = \boldsymbol{\omega}/\|\boldsymbol{\omega}\| \times r_n$, $r_n$ (n=1,...,8 for hexahedral cell) are the locations of the cell vertices. In addition, various alternative differential operators were considered based on other LES models, aside from the classical Smagorinsky [4] ($SMG$). In particular, the $\sigma - LES$ [5] was selected as a good candidate for its ability to switch off in 2D flow regions. When both strategies ($\tilde{\Delta}_\omega$ and $\sigma - LES$) were combined (also called $\sigma - DES$), significant improvements were obtained with respect to the original DDES [1] at comparable computational cost [6,7],
In addition, Shur et al. [8] proposed another SLS in combination with the $SMG$ model,

$$\Delta_{SLA} = \tilde{\Delta}_\omega F_{KH}(\langle VTM \rangle), \tag{4.3}$$

where the $\tilde{\Delta}_\omega$ was modified to switch off in 2D flow regions through a blending function, $F_{KH}(\langle VTM \rangle)$. This strategy is known as the Shear Layer Adapted (SLA) approach. The Vortex Tilting Measure ($VTM$) coefficient is used as an indicator of 2D flow regions,

$$VTM = \frac{|\,(\mathsf{S}\boldsymbol{\omega}) \times \boldsymbol{\omega}|}{\omega^2 \sqrt{-Q_{\tilde{\mathsf{S}}}}}, \tag{4.4}$$

where $\tilde{\mathsf{S}}$ is the traceless part of the rate-of-strain tensor, $\mathsf{S} = 1/2\left(\nabla\bar{\boldsymbol{u}} + \nabla\bar{\boldsymbol{u}}^T\right)$, i.e. $\tilde{\mathsf{S}} = \mathsf{S} - 1/3tr(\mathsf{S})\mathsf{I}$. Note that for incompressible flows $tr(\mathsf{S}) = \nabla \cdot \bar{\boldsymbol{u}} = 0$, therefore, $\tilde{\mathsf{S}} = \mathsf{S}$. Finally, $Q_{\mathsf{A}} = 1/2(tr^2(\mathsf{A}) - tr(\mathsf{A}^2))$ refers to the second invariant of a second-order tensor $\mathsf{A}$. This approach has been successfully applied to several flow configurations [7,9], reducing the delay of the flow instabilities in the shear layer.

The objective of this chapter, which is aligned with the $\sigma - DES$ strategy, consists of exploring a recently developed LES strategy for mitigating the *GA* phenomenon. The hypothesis is that this numerical issue can be mitigated via the appropriate choice of SLS and $D_{sgs}\,(\tilde{u}_i)$ strategies. In this regard, the improvements suggested here are inherited from Trias et al. [10, 11], who developed a new family of LES models, *S3PQR*, and a new kinematic-sensitive SLS, $\Delta_{lsq}$, based on the velocity gradient. They are explained in detail in chapter 3. While both approaches, *S3PQR* and $\Delta_{lsq}$, were originally designed and tested for LES applications, preliminar studies [12,13] showed how they can be successfully applied to address the *GA* issue in DDES simulations.

In this chapter, the performance of the new approach is compared to the existing methodologies described above ($SMG + \Delta_{SLA}$ [8] and the $\sigma - DES$ [6]) in three different flow configurations. Namely, (i) the experimental results obtained by Vogel and Eaton [14] for an incompressible Backward Facing Step (BFS) at $Re_h = 28000$ (based on inflow bulk velocity, $U_b$, and the step edge, $h$) and Expansion Ratio, $ER = 5/4$, a ratio of the outflow vs the input heigths; (ii) the Direct Numerical Simulation (DNS) results of a BFS at $Re_\tau = 395$ (based on the inlet conditions) and $ER = 2$ [15], where the growth of the Kelvin-Helmholtz instabilities in a shear layer is studied in detail and (iii) a compressible subsonic jet at $Re = 1.1 \times 10^6$ and $M = 0.9$ [16,17]. All these simulations have been carried out using two CFD codes, *OpenFOAM* and *NOISEtte* [18].

The rest of the chapter is arranged as follows. In the next section, the new strategies proposed for mitigating the *GA* issue are defined. The cases used for studying the *GA* mitigation capabilities of the standard and new strategies are described in section 4.3, as well as a complete description of the two codes used in this chapter. The behavior of the new approach is compared with the standard mitigation techniques in section 4.4, using the cases and codes mentioned above.

## 4.2 Decaying Homogeneous Isotropic Turbulence (DHIT)

Before applying and comparing the new approaches, $\Delta_{lsq}$, with the present well-established techniques for mitigating the Grey Area, they have been firstly calibrated in a DHIT case (Wray [19] configuration), where the DDES turbulence model acts in LES mode.

Different $C_{DES}$ coefficients have been analysed (Eq. 3.9), concluding that $C_{DES} = 0.65$ is the most appropriate, regardless of the subgrid length scale. The study considering different $C_{DES}$ has not been included in this thesis, but it is worth noting that both meshes, $32^3$ and

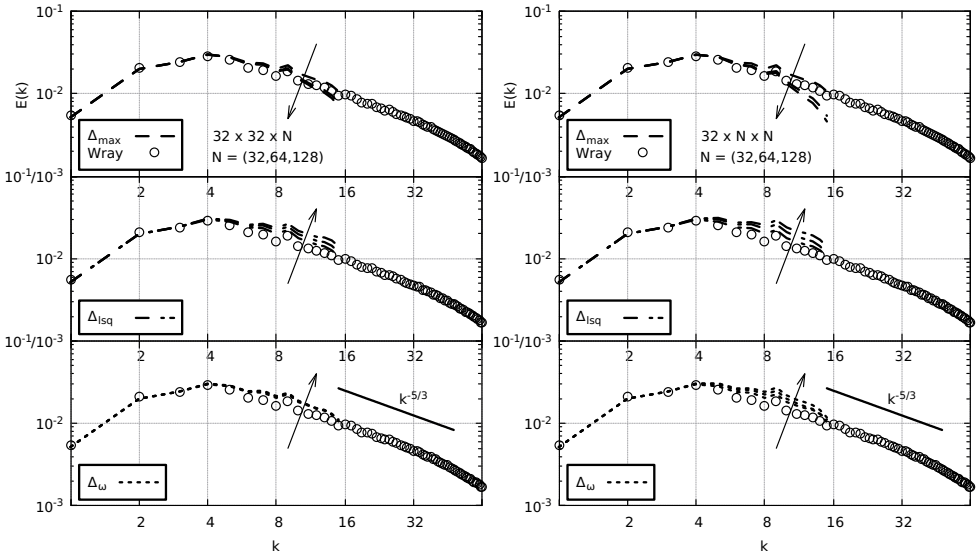


**Figure 4.1:** Assessment of the mesh resilience capabilities for different subgrid length scales in a DHIT ($C_{DES} = 0.65$) case; $\Delta_{\max}$ (top), $\Delta_{lsq}$ (middle) and $\tilde{\Delta}_\omega$ (bottom). "*Book*" (left) and "*Pencil*" (right) cells are considered.

$64^3$ have been studied. Regarding the subgrid length scale resilience in anisotropic meshes, a couple of cell configurations have been considered in figure 4.1, *Book* ($32 \times 32 \times N$,left) and *Pencil* ($32 \times N \times N$,right), respectively. First, $\Delta_{\max}$ is too dissipative with anisotropic meshes in both situations, but their effects are pronounced in the *Pencil* case, where the length scale clearly underestimate the mesh capabilities for solving turbulence. The contrary is true in the $\Delta_{lsq}$ case, where the dissipation introduced by the DDES model is not enough, increasing the energy retained in the smallest scales. This behaviour can be attributed to the subgrid length scale property discussed in section 3.3.1, where $\Delta_{lsq}$ allows values similar to the smallest scale ($\beta^{-1}$). However, in contrast to $\Delta_{\max}$, the same reaction is observed for *Book* and *Pencil* cells, indicating a beneficial lack of sensitivity to the kind of mesh anisotropy. Finally, the most robust behaviour is presented by $\tilde{\Delta}_\omega$, which apparently does not present any missalignment in the *Book* shape and only small discrepancies are observed in the *Pencil* case. This feature is associated with the intrinsic definition of the subgrid length scale, where the diagonal value of the cell volume is assessed. By definition, it means that $\tilde{\Delta}_\omega$ is always going to depend at least on 2 dimensions, being sensitive to the mesh anisotropies, but at the same time limiting their downward excursions, something that cannot be guaranteed in the $\Delta_{lsq}$. Results from $\Delta_{SLA}$ have not been shown here as they behave like $\tilde{\Delta}_\omega$ in a DHIT case, where there is no any clear 2D flow. The spacial filter used in $\langle VTM \rangle$ is actually used for ensuring such feature.
It is worth mentioning here that even we have observed an interesting clear advantage of $\tilde{\Delta}_\omega$

and $\Delta_{SLA}$ over $\Delta_{lsq}$, this is not observed in the choosen flow configurations presented in the next section. We also need to consider that any of the cases simulated in this thesis does not resamble any complex industrial application (at least in terms of geometry), so future research would be needed in this area.

## 4.3 Simulation Set-up

A set of three different flow configurations has been used to test the above-mentioned techniques, considering both incompressible and compressible flows. Moreover, the performance of the new SLS and differential operators has been tested with two different CFD codes, *OpenFOAM* and *NOISEtte*.

### 4.3.1 Cases

All cases used here are well-known in the DDES community for assessing the impact of *GA* mitigation methods. They present free shear layer regions in simple geometrical configurations, where the impact of the model on the anticipated development of instabilities can be easily studied.

- **BFS: Vogel & Eaton**
  This *BFS* configuration resembles the experimental study carried out by Vogel and Eaton [14] at $Re_h = 28000$ and ER equal to $5/4$. The fluid is incompressible and the $Re_\tau$ at the inflow is around 2500. The computational domain, mesh and boundary conditions can be found in work by Spalart et al. [1]. This configuration is a reference case in the DDES literature for studying the RANS to LES transition downstream of the step-edge. Hereafter, this case is named *BFS-VE* .
- **Instabilities' growth at the shear layer**
  As well as considering fluctuation intensity as a means for evaluating model capabilities in the RANS to LES transition region, in this case we may also use a *BFS* case to study the growth of these instabilities along the shear layer. The case reported by Pont-Vílchez et al. [15] covers both of these aspects in an incompressible *BFS* at $Re_\tau = 395$ and $ER = 2.0$. Emphasis was placed downstream of the step-edge, where the shear layer instabilties appear. In the present work, the dimensions of the computational domain have been reduced respect to the reference DNS case, in order to resemble the *BFS-VE* domain. The new dimensions are $24h \times 2h \times 2h$ in the stream-wise, normal and span-wise directions, respectively. The sudden expansion is located at $4h$ from the inflow. The origin of coordinates is placed at the step-edge. Three meshes with different refinement levels in the stream-wise direction (free shear layer area) just downstream the step-edge, $x_1 = [0, h]$, have been considered for evaluating the mesh resilance capabilities of the candidate *GAM* approaches. The length of the first grid cell after the step-edge in the stream-wise direction is 8, 16 and 32 wall-units. The rest of mesh parameters are kept constant. These are: the Poisson growth ratio equal to 1.1, the number of cells per $x_1x_2$-plane equal to 11800 and the number of planes in the periodic direction equal to

60. Regarding the boundary conditions, a turbulent channel flow is set at the inflow at $Re_\tau = 395$. Hereafter, this case is named *BFS-DNS* .

- **Round unheated compressible jet**
  The immersed jet exiting from a conical nozzle at $M_{\text{jet}} = 0.9$ and $Re_D = 1.1 \times 10^6$ based on the jet diameter $D$ and jet exit velocity $U_{\text{jet}}$ is considered. The resulting flow dynamics are similar to cases studied experimentally by several authors in the literature [20–24]. The computational domain, mesh and boundary conditions can be obtained from the study carried out by Shur et al. [25]. Afterwards this case was used in different investigations [8, 26]. It is considered to be a reference configuration for assessing the RANS to LES transition capabilities of different SLS and $D_{sgs}\left(\tilde{u}_i\right)$ in compressible flows. The simulation of the jet follows a two-stages approach when nozzle and jet-plume computation is performed using RANS at the first stage, while only the jet-plume region is considered at the second stage, with profiles from the first stage imposed at the nozzle exit boundary surface. These profiles of gas-dynamic and turbulence model variables were provided by M. Shur and M. Strelets from Peter the Great St. Petersburg Polytechnic University. The structured (hexahedral) Grid 3 from the papers [25] is used for computations of the jet case. It has 160 cells in the azimuthal direction and contains $8.87M$ nodes in total.

### 4.3.2 Codes

Both codes employ a time integration implicit second-order scheme, doing several iteration stages per time step to achieve the desired degree of convergence. The Courant number has been kept below unity in the LES zone to ensure a proper triggering of turbulence. Both codes use the hybrid convective scheme suggested by Spalart et al. [27], switching from Symmetry-Preserving to Upwind-based depending on the flow behavior. In particular, the upwind dissipation vanishes in LES areas, whereas it is activated in RANS and some critical zones to guarantee system stability. The rest of code's features are different. Namely,

- *OpenFOAM*
  This well-known open-source CFD code is based on a collocated unstructured finite-volume approach. All simulations have been carried out using a second-order implicit scheme. The hybrid convective scheme blends between a 2nd order central difference in the LES region and a 2nd order upwind-biased scheme in the RANS and irrotational area.
- *NOISEtte*
  The numerical algorithm realized in the research code *NOISEtte* [28] is based on quasi-1D vertex-centered EBR (Edge-Based Reconstruction) schemes [29, 30]. These schemes combine the advantages of structured and unstructured methods and provide a reasonable balance between accuracy and computational costs in scale-resolving simulation. On arbitrary unstructured meshes, the EBR schemes are theoretically of maximum second-order depending on the type of mesh elements and duals. *NOISEtte* exploits an implicit second-order time integration scheme which is based on Newton iterations algorithm and a bi-conjugate gradient approach for solving the system of linearized algebraic

equations at each iteration. Regarding the convective scheme, *NOISEtte* used a 4th order centered and 5th order upwind schemes in the LES and RANS areas, respectively.

## 4.4 Results and Discusions

The results provided here have been obtained employing the *GAM* techniques shown in table 4.1. They have been grouped by case, which are defined in subsection 4.3.1.

**Table 4.1:** *GAM* techniques considered in this thesis. The new approach is marked with $(^*)$.

| | SLS | $D_{sgs}\left(\tilde{u}_i\right)$ |
|---|---|---|
| | $\Delta_{SLA}$ | $SMG$ |
| $(^*)$ | $\Delta_{lsq}$ | $SMG$<br>$S3PQR$ |
| | $\tilde{\Delta}_{\omega}$ | $SMG$<br>$\sigma$ |

### 4.4.1 BFS: Vogel & Eaton

It can be observed in both codes how the new SLS, $\Delta_{lsq}$, behaves slightly better than the standard strategies for mitigating the *GA* (figure 4.2). Especially at the free shear layer area, close to the step edge. While there is no experimental or high-quality numerical data supporting this comparison, the triggering of oscillations at the free shear layer appear to be linked to an improved resolution of the flow dynamics in the LES region. This is, indeed, the main objective of the *GA* mitigation strategies. Apart from that, all SLS present a good agreement downstream the free shear layer at $x_1 > 2h$.
First, we discuss the results obtained with *OpenFOAM* and using a *SMG* turbulence model. The differences observed between the SLS strategies at the free shear layer area can be explained by drawing a comparison between earlier results for homogeneous flows, shown in figure 3.3 and the $\Delta$ distribution downstream the step-edge in figure 4.3. As expected, $\Delta_{\max}$ returns the highest values, translating to higher dissipation in the shear layer which contributes to an excessive delay. An important reduction of $\Delta$ is shown in figure 4.3 when using $\tilde{\Delta}_{\omega}$, as a 2D flow behaviour in the $x_1x_2$ plane downstream of the step-edge is detected (*GA* region), ignoring $\Delta x_3$ and getting closer to the diagonal value in this plane; $\tilde{\Delta}_{\omega-2D} = \sqrt{(\Delta x_1^2 + \Delta x_2^2)/3}$.
It is worth noting here that $\tilde{\Delta}_{\omega}$ will never provide values lower than the lowest 2D diagonal of the cell,

$$\tilde{\Delta}_{\omega\min} = \min_{i!=j}\left(\sqrt{(\Delta x_i^2 + \Delta x_j^2)/3}\right). \tag{4.5}$$

In this case, $\tilde{\Delta}_{\omega}$ and $\tilde{\Delta}_{\omega-2D}$ do not completely collapse as the numerical oscillations start from the very beginning of the step-edge (rms values in figure 4.3, left, at $x_1/h = 0$ are not

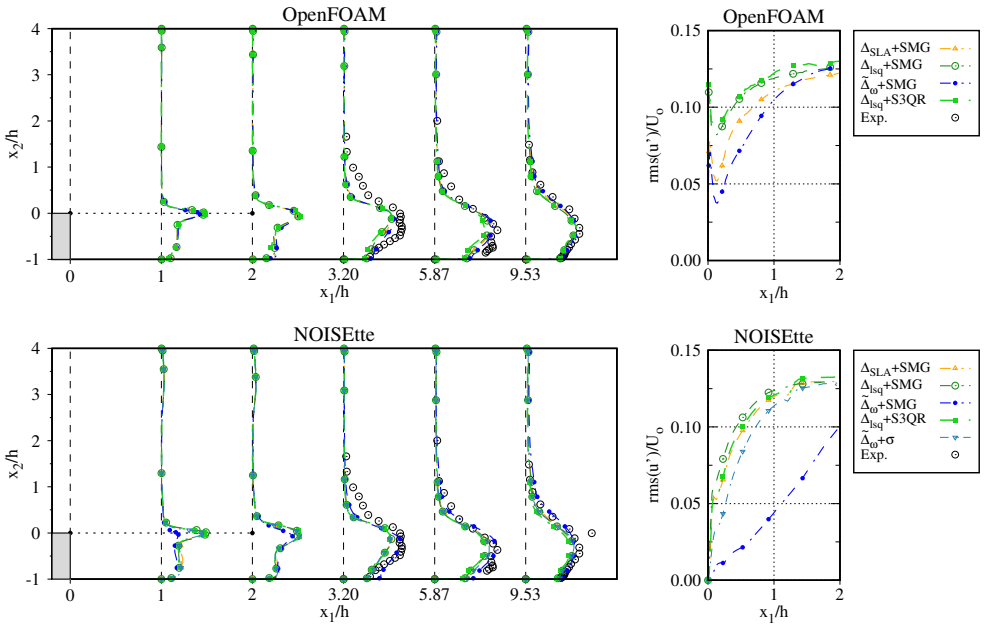


**Figure 4.2:** Resolved Reynolds stresses in the stream-wise direction, rms$(u')$, considering various SLS in combination with different $D_{sgs}$ $(\tilde{u}_i)$ (left) and its evolution at $x_2 = 0$ (right). Where $U_o$ refers to the inflow bulk velocity. Reference experimental data, $Exp.$, has been obtained from Vogel and Eaton [14].

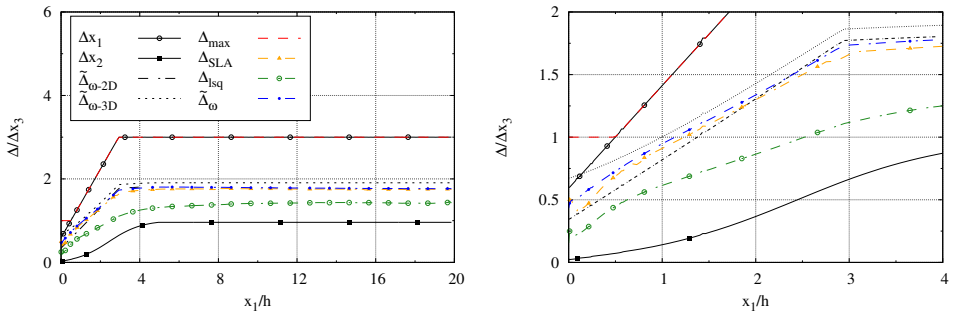


**Figure 4.3:** SLS average at the step-edge ($x_2 = h$) along the stream-wise direction (left),$x_1$, and a zoom view (right).

0). This is attributed to the high aspect ratio close to the step-edge ($\Delta x/\Delta y \sim 32$). Therefore, these oscillations lead to $\Delta$ values which are representative of $3D$ structures, i.e. $\tilde{\Delta}_{\omega-3D} = \sqrt{(\Delta x_1^2 + \Delta x_2^2 + \Delta x_3^2)/3}$ rather than 2D, $\tilde{\Delta}_{\omega-2D}$ (figure 4.3). These undesirable oscillations also affect the $\Delta_{SLA}$ natural behaviour, which is not deactivated close to the step-edge. Considering the impact of these oscillations in the overall simulation, a special test has been carried out in the next case in order to understand how they are affected by the aspect ratio at the step-edge.
In contrast to $\tilde{\Delta}_\omega$, where the minimum value is limited by Eq. 4.5, $\Delta_{lsq}$ can provide values as small as the wall mesh refinement allows $\Delta x_2$ (the order of wall units in RANS-LES simulations). This interesting property was noted previously in chapter 3 and in figure 3.3 for "Simple Shear" dynamics. This feature is thus highly relevant to the BFS, and many other configurations exhibiting similar separation and subsequent development of instabilties in the shear layer. The small $\Delta$ values lead to a strong reduction of the eddy-viscosity, generally unlocking the Kelvin-Helmholtz instabilities and improving the quality of the simulation in the LES region. However, while we can observe in figure 4.3 how $\Delta_{lsq}$ follows a similar trend than $\Delta x_2$ distribution, there is a clear offset, mainly produced by the initial oscillations at the step-edge. It explains why the transition from "Simple Shear" to "Pure Rotation" cannot be completely appreciated in figure 4.3 (both terms are defined in figure 3.3). It is important noting here that $\Delta_{lsq}$ still presents the lowest values of $\Delta$, which explains the good behaviour of the oscillations observed in figure 4.2.
The behavior of the fluid close to the wall has also been studied by means of the skin friction, $\left\langle C_f \right\rangle$, distribution in both, the upper and lower walls in figure 4.4.
Apart from showing a slightly better performance for $\Delta_{lsq}$ in the lower wall, we can confirm that both $\Delta_{lsq}$ and $\tilde{\Delta}_\omega$ behave in a really similar way. It was not so predictible considering that $\Delta_{lsq}$ can present values around $\Delta x_n$ (where $n$ indicates the normal wall direction) close to the wall (figure 3.3), could severly reduce the RANS area due to the LES invasions (harming the shielding function), reducing the turbulent viscosity and strongly affecting the skin friction.

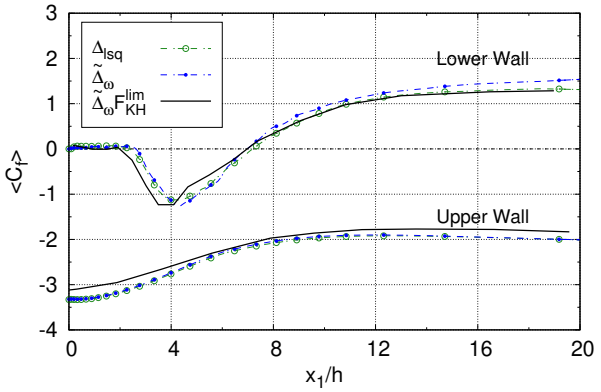


**Figure 4.4:** Skin friction, $\left\langle C_f \right\rangle$, at the lower and upper walls downstream of the step edge for the Vogel and Eaton BFS case [14].

Therefore, the fact of observing that $\Delta_{lsq}$ and $\tilde{\Delta}_\omega$ present a similar behavior, clearly indicates that the new approach does not significantly affects the DDES shielding function in such flow configuration.
Regarding the results obtained with other differential operators, we can note that combining $\tilde{\Delta}_\omega$ with a 2D-sensitive formulation, such as $\sigma$, results in a significant improvement in the free shear layer area (figure 4.2). This is in good agreement with the observations carried out by previous authors [6,7]. This is not the case for $\Delta_{lsq} + S3QR$, which presents almost no difference in comparison with $\Delta_{lsq} + SMG$. Figure 4.2 also demonstrates that very similar trends are observed in both codes, *OpenFOAM* and *NOISEtte*, which is clearly a good indication of the reliability and code independence of the new approach.
While the *BFS-VE* case is an important reference for hybrid methods, the lack of detailed reference data in the free shear layer region reduces the scope for a more detailed analysis of model performance. For this reason, a comparison with DNS data has been performed in the next section, using another *BFS* configuration [15]. In particular, it enables a detailed examination of the intriguing oscillations which appear just after the step-edge in the *OpenFOAM* . They are anticipated to be due to the high cell aspect ratio in this area, $\Delta x_1/\Delta x_2 \sim 32$, but their relation is not clear. As such, a set of meshes with different aspect ratios and refinements downstream the step-edge are tested in the *BFS-DNS* case.

### 4.4.2 Instabilities' growth at the shear layer

As identified in the previous section, the motivations for considering this case; 1) to investigate performance of the new appproach in free shear layer region and 2) to assess their sensitivity in this region, to high aspect ratio cells. Figure 4.5 demonstrates how rms$(u')$ is affected by

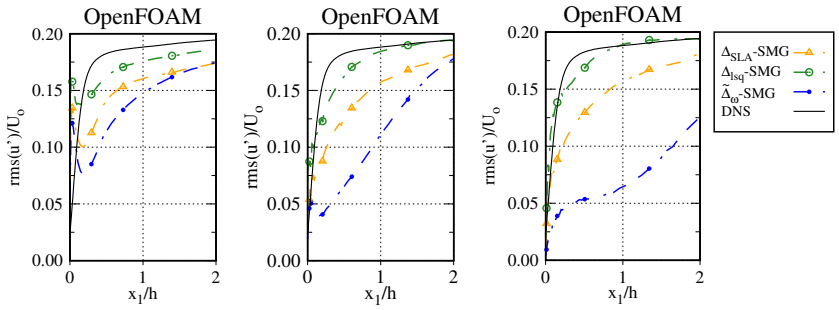


**Figure 4.5:** Resolved Reynolds stresses, rms$(u')$, along the stream-wise direction at $x_2 = 0$, considering similar meshes with different aspect ratios, $\Delta x_1/\Delta x_2$, at the step edge. These are: 32 (left), 16 (middle) and 8 (right). Where $U_o$ refers to the inflow bulk velocity. Reference data, DNS, has been obtained from Pont-Vílchez et al. [15].

the cell aspect ratio, $\Delta x_1/\Delta x_2$, at the step edge in the $x_1x_2$ plane. In addition to observing that stronger fluctuations are triggered by $\Delta_{lsq}$ compared to the other candidates, we can also appreciate the good alignment with the DNS dataset. This supports the hypothesis that $\Delta_{lsq}$ contributes to an improved definition of the $Kelvin - Helmholtz$ -instabilities in the shear layer region. Furthermore, it seems that the observed oscillations just after the step-edge are strongly mitigated when the cell aspect ratio in this region is reduced. Other interesting interpretations can be made from figure 4.5, such as the strong mesh resilience presented by $\Delta_{lsq}$ and $\Delta_{SLA}$ with respect to $\tilde{\Delta}_\omega$. The poor performance of $\tilde{\Delta}_\omega$ observed in figure 4.5 (left) is attributed to the cell's stream-wise size (at $x_1/h \sim 1$) and the strong dependence of this value on $\tilde{\Delta}_\omega$. This is not true for the other definitions of SLS, since $\Delta_{lsq}$ might not depend on this value (figure 3.3) and $\Delta_{SLA}$ can be considerably reduced if a 2D flow is detected (as in this case). Finally, it also seems that while there appears at first glance to be some 'benefit' of these unphysical oscillations in the development of turbulence downstream of the step, this is likely to be fortuitous, since the tests for $AR = 32$ never entirely recover the DNS levels of rms$(u')$. The subsequent analysis considers only the mesh with $\Delta x_1/\Delta x_2 = 16$. The rms distributions along the stream-wise direction are presented in figure 4.6. In addition to a significant improvement of $\Delta_{lsq} + SMG$ in comparison to $\tilde{\Delta}_\omega + SMG$ and $\Delta_{SLA} + SMG$ at the shear layer, all SLS behave similarly downstream of the step-edge ($x_1 > 2$) for both codes. A general misalignment is seen at $x_1 = 8$, which is attributed to the lack of mesh resolution in this region. The positive effect of using a 2D sensitive differential operators, such as $\sigma$, in combination with $\tilde{\Delta}_\omega$ is demonstrated once again in the free shear layer area (figure 4.6, right). In a similar way to in the previous case, there was almost no sensitivity of $\Delta_{lsq}$ to the $D_{sgs}$ $(\tilde{u}_i)$ used, as as observed in the *BFS-VE* case, similar results are obtained with both codes, *OpenFOAM* and *NOISEtte*.

It is worth noting here that in both BFS we observed how $\tilde{\Delta}_\omega + SMG$ presented a clear delay in the shear layer oscillations in comparison to other SLS, such as $\Delta_{SLA} + SMG$ and $\Delta_{lsq} + SMG$. However, in the simulations carried out with *NOISEtte*, $\tilde{\Delta}_\omega + SMG$ is the one that presented the

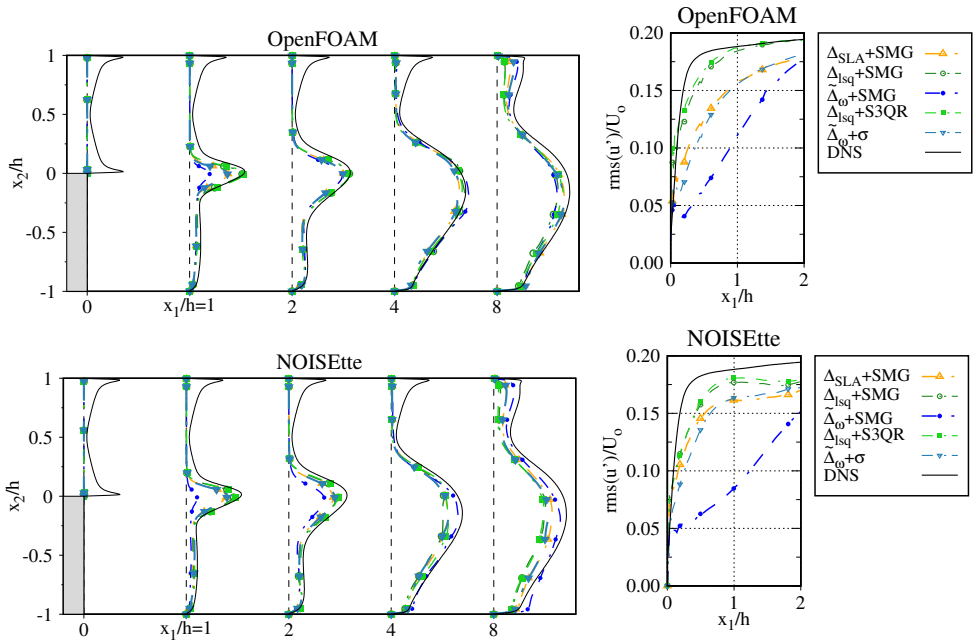


**Figure 4.6:** Resolved Reynolds stresses in the stream-wise direction, rms$(u')$, considering various SLS in combination with different $D_{sgs}$ $(\tilde{u}_i)$ (left) and its evolution at $x_2 = 0$ (right). Where $U_o$ refers to the inflow bulk velocity. Reference data, DNS, has been obtained from Pont-Vílchez et al. [15].

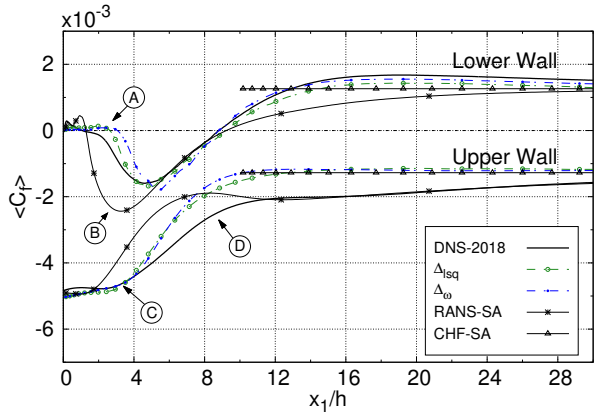


**Figure 4.7:** Skin friction, $\left\langle C_f \right\rangle$, at the lower and upper walls downstream of the step edge. Reference data, $DNS$, has been obtained from Pont-Vílchez et al. [15].

best results downstream of the step edge, once the delay of the shear layer was recovered. This effect is due to the fact the vortex created in the shear layer with $\tilde{\Delta}_\omega + SMG$ are more energetic than those created with the other considered SLS. In other words, as the difussion is higher and the convection lower, the eddies created in the shear layer does not decompose in smaller eddies so quickly. This mechanism explains the presence of higher oscillation downstream of the step-edge for those SLSwhich are too diffussive. It is also true that this effect is not so well observed in the OpenFOAM case. This is attributed to the convective schemes, as the one used by *NOISEtte* provides lower levels of numerical dissipation.

Regarding the behavior of the fluid close to the wall, we can observe the skin friction, $\left\langle C_f \right\rangle$, distribution in both, the upper and lower walls in figure 4.8.

First, the improvements of $\left\langle C_f \right\rangle$ coefficient triggered by the better resoultion of the shear layer can be clearly observed at the lower wall (Fig.4.8, left, **A**) with the $\Delta_{lsq}$. In that case, the $\left\langle C_f \right\rangle$ peak is also better captured than the $RANS - SA$ simulation and $\tilde{\Delta}_\omega$ (**B**). Moreover, the improvement of $DDES - SA$ respect to the $RANS - SA$ is also evident at the upper wall, where the separation point is delayed (**C**). However, $DDES - SA$ model does not properly capture the channel flow recovering process neither in the upper nor the lower walls (**D**). The $\left\langle C_f \right\rangle$ depletion at the upper wall is produced because of the LES interference into the RANS zone, diminishing the eddy viscosity in a place where turbulence is not well triggered yet. The improvements observed in the $\left\langle C_f \right\rangle$ at the lower wall with $\Delta_{lsq}$ is in good agreement with the results presented in *BFS-VE* (section 4.4.1). Again, they clearly indicate that the new approach does not significantly affects the DDES shielding function in such flow configuration. Unfortunately, this observation has been obtained only comparing the same *BFS*flow configuration, so

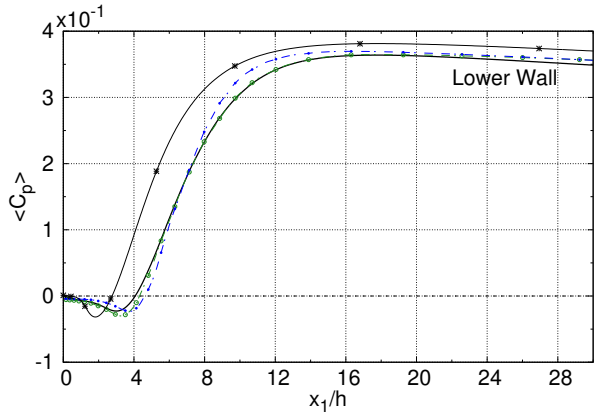


**Figure 4.8:** Pressure coefficient, $\langle C_p \rangle$, at the lower wall downstream of the step edge. Reference data, $DNS$, has been obtained from Pont-Vílchez et al. [15].

it cannot be extrapolated to other cases (where extra research is clearly needed). Similar trends can be observed with the pressure coefficient, $\langle C_p \rangle$, distribution, where $DDES - SA$ models present a clear advantage over $RANS - SA$, as they are clearly benefited from the transient resolution of the flow at the shear layer.
Finally, the instabilities' growth at the shear layer presented by different SLS is analyzed using the same approach described by Pont-Vílchez et al. [15]. A scheme view of this phenomenon is presented in figure 4.9. The instabilities' size in the stream-wise direction, $\Delta\delta_1$, is calculated using a set of 2-point correlations of $u'_2$ along the stream-wise direction downstream of the step-edge (figure 4.10). Unfortunately, this technique cannot be applied for assessing the instabilities' size in the normal direction ($\Delta\delta_2$), as the flow behaves laminarly in some parts along the normal direction. These feature makes the 2-point correlations unusable for estimating $\Delta\delta_2$, so another approach has been used [15, 31],

$$\Delta\delta_2 = \Delta U_1 / (\partial \langle u_1 \rangle / \partial x_2)_{\max}. \tag{4.6}$$

Even though the rms profiles present a strong dependence on the $SLS$ (figure 4.6) along the shear layer, this is not so significant in the $\Delta\delta_1$ distribution (figure 4.10, top). In particular, $\Delta_{lsq}$, together with $\Delta_{SLA}$, show the best alignment at $x_1 \in [0, 0.8h]$. This strong correlation with DNS data is somewhat reduced downstream, leading to a shallower slope in comparison to $\tilde{\Delta}_\omega$ and the DNS. This deterioration is attributed to the mesh coarsening in this region.
Regarding $\Delta\delta_2$, it seems to be quite sensitive to the SLS (figure 4.10, bottom). This was an expected behaviour as the terms used for estimating $\Delta\delta_2$ ( Eq.4.6), indirectly depends on other terms which are highly influenced by SLS, such as rms$(u')$. Hence, figure 4.10 (bottom) clearly demonstrates once again how diffusion introduced by $\Delta_{SLA}$ and $\tilde{\Delta}_\omega$ is too high to ensure the correct development of the Kelvin-Helmholtz instabilties along the shear layer.

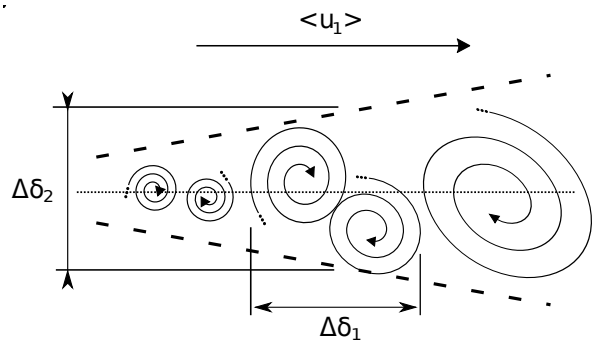


**Figure 4.9:** Schematic view of the Kelvin-Helmholtz vortices in a shear layer, where $\Delta\delta_1$ and $\Delta\delta_2$ represent a estimation of the vortex size in the stream-wise and normal direction, respectively.

### 4.4.3 Round unheated compressible jet

The jet plume region characteristics obtained using different approaches realized in both codes (*NOISEtte* and *OpenFOAM* ) are presented on the figures 4.11-4.15. In terms of the correspondence with the reference data, the first observation is that all approaches evaluated in this thesis capture the jet dynamics reasonably well, with the exception of one model. The limited capability for *GA* mitigation of the $\tilde{\Delta}_\omega$ length scale in the jet case is expected and was already reported in previous studies [3, 8, 16].
Figures 4.11 and 4.12 present a comparison of the averaged stream-wise velocity and its rms distributions, correspondingly, over the jet centerline. All the approaches (except $\tilde{\Delta}_\omega + SMG$) allow to predict the length of the jet core region more or less correctly. The results obtained using the *NOISEtte* research code are notably more consistent than the *OpenFOAM* ones. This behaviour could be due to the numerical scheme employed for convective fluxes and its dissipation properties. *NOISEtte* uses the higher accuracy EBR scheme which exploits extended stencils to achieve higher resolution which results in less dissipation from the numerical scheme. So the RANS-to-LES transition in the shear layer develops more smoothly, without sudden exposure-like wakes or instabilities. This observation is supported by figure 4.12, where the rms levels of stream-wise velocity start to grow permanently, in the region $2x/D$ till $3.5x/D$ and are noticeably overestimated by the region $5 < x/D < 10$, in contrast to the corresponding distributions obtained using the *NOISEtte*. After reducing a maximum between $10 < x/D < 12$, the centerline distributions of $\mathrm{rms}(u')$ obtained by all the considered *GA* mitigation approaches and both codes are close to each other and to the experimental values.
A more in-depth evaluation of performance is now considered by analyzing the distributions of various characteristics along the lip line downstream of the nozzle edge; presented in the figures 4.13-4.15. The averaged subgrid length scale normalized by its maximum, $\Delta_{\max}$, local value and turbulent to molecular viscosity ratio are shown on the figures 4.13 and 4.14, correspondingly. By analyzing these plots the following features can be revealed. First of all, none of the

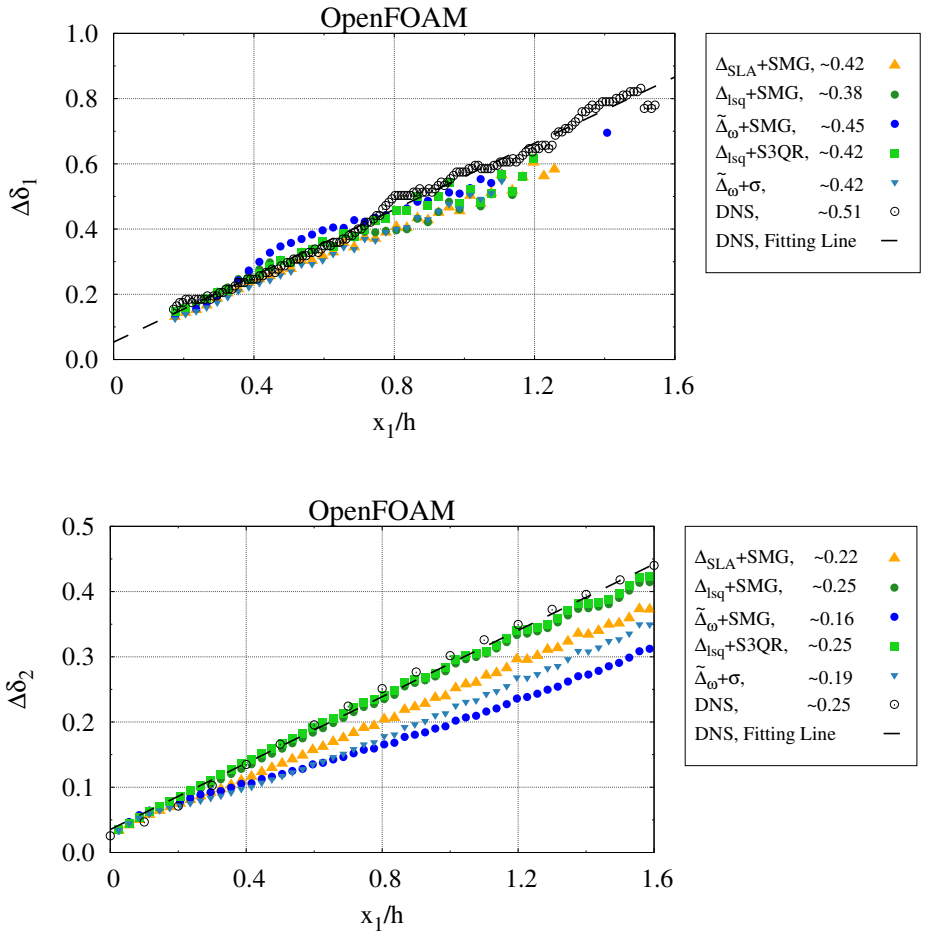


**Figure 4.10:** Estimation of the Kelvin-Helmholtz rate of growth in the streamwise (top) and normal (bottom) directions downstream of the step-edge using different SLS, $\Delta\delta_1$ and $\Delta\delta_2$ respectively. Reference data, DNS, has been obtained from Pont-Vílchez et al. [15]. The float value in the legend shows the slope of the linear regression, which have been calculated for each curve.

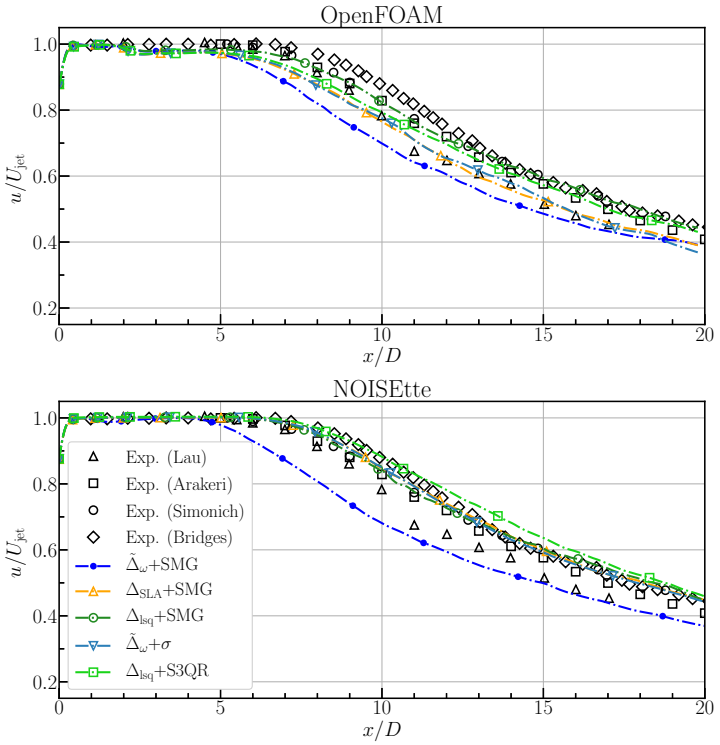


**Figure 4.11:** Average of the stream-wise velocity over the jet center line starting from the jet nozzle exit.

considered subgrid scales ($\tilde{\Delta}_\omega$, $\Delta_{SLA}$ and $\Delta_{lsq}$) does reach $\Delta_{\max}$ value either at the early shear layer region (as it is highly desirable for fast RANS-to-LES transition) or far downstream the nozzle exit. This is related with the anisotropy of the mesh used in the simulations along the lip line. Another obvious property is that the $\Delta_{lsq}$ values and, accordingly, turbulent viscosity levels are significantly lower than those provided by $\tilde{\Delta}_\omega$ and $\Delta_{SLA}$ length scales. In the very early shear layer region (see the right plots of figure 4.13), at $x/D \lesssim 0.1$, the $\Delta_{SLA}$ length scale drops to very low values with strong growth till $x/D \approx 0.3$ (due to impact of $F_{\mathrm{KH}}$ ($\langle \mathrm{VTM} \rangle$) function). The $\Delta_{lsq}$ is proportional to $\Delta_{\min}$ before $x/D = 0.2 - 0.3$. After $x/D = 0.3$ both length scales ($\Delta_{SLA}$ and $\Delta_{lsq}$) have the same increasing trend up to $x/D \approx 0.9$. In the developed shear layers regions, with resolved 3D turbulence, the $\Delta$ distributions behave like $O(\Delta_{\max})$ with slight deviation in the approximate region $0.4\Delta_{\max} < \Delta < 0.7\Delta_{\max}$. The turbulent viscosity levels (presented on the figure 4.14) mostly follow the corresponding subgrid length scale values' trends. The distributions of stream-wise velocity rms values are presented on the figure 4.15.

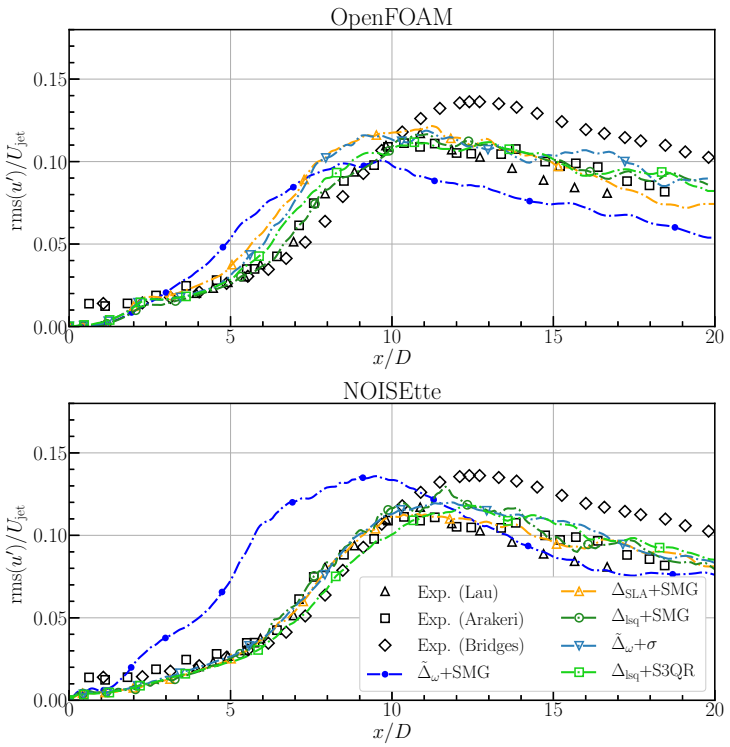


**Figure 4.12:** Average of the stream-wise velocity root-mean square over the jet center line starting from the jet nozzle exit.

Overall, all the considered approaches result in a good correlation with the reference data and with each other. It is being observed for both codes, *NOISEtte* and *OpenFOAM*, too. The only noticeable discrepancy can be revealed in the early shear layer region at $0 < x/D < 2$: the peak values of rms$(u')$ from the OpenFOAM simulations are higher than the NOISEtte ones. It can be attributed to, as already mentioned above in this subsection, to the behaviour of the numerical scheme for convective fluxes: low dissipativity and higher accuracy of the numerical scheme facilitate earlier and more smooth RANS-to-LES transition while the turbulent viscosity has the same levels. This slight delay results in a notably more intense "numerical" transition downstream, that is manifested in higher levels velocity rms distributions in this part of the shear layer. It is seen from the figure 4.15 (right) that $\Delta_{SLA}$ provides faster development of the separated flow apparently due to the lower levels of turbulent viscosity. As also pointed out in the previous subsections (4.4.1 and 4.4.2) two peaks of stream-wise velocity rms are observed in the early shear layer region (see right subfigures of figure 4.15): the first lays at $x/D \approx 0.05$ in the NOISEtte distributions and at $x/D \approx 0.15$ in the OpenFOAM ones; the second – in the

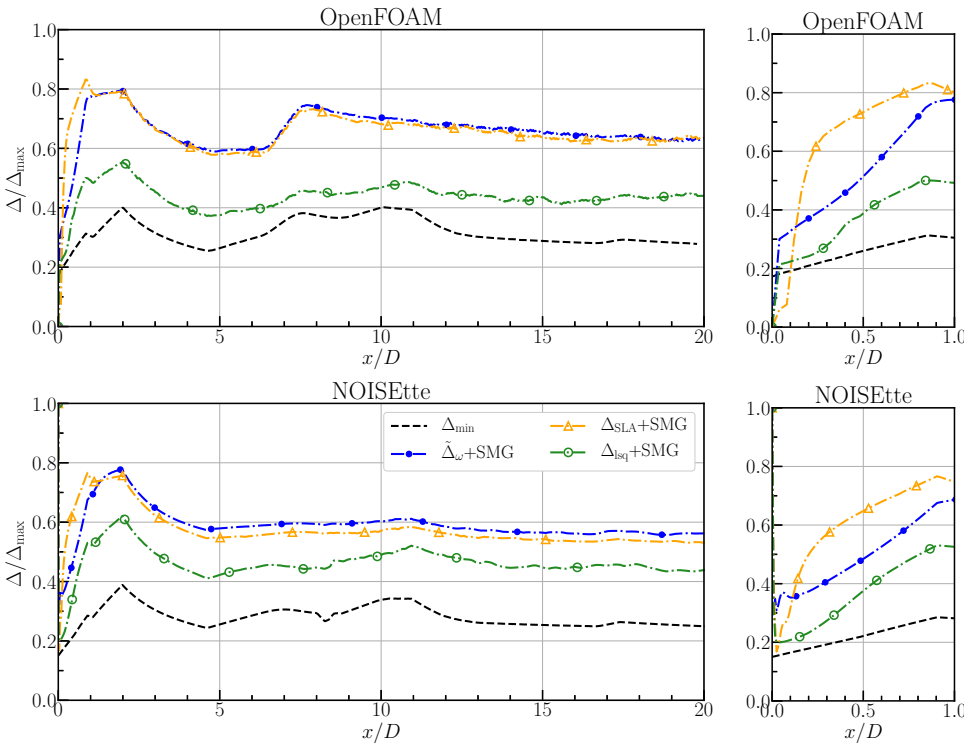


**Figure 4.13:** Average of the subgrid length scales over the lip line starting from the jet nozzle exit (left) and its zoom view near the edge (right).

region $0.3 < x/D < 0.7$, depending on the method and the code used. The first peak, driven by RANS-to-LES "numerical" transition, has an unphysical nature, likely related to the mesh anisotropy in this region, while the second is attributed to the resolved turbulence in the shear layer.

The usage of alternative LES subgrid model, $\sigma$ in combination with $\tilde{\Delta}_\omega$ and $S3QR$ in combination with $\Delta_{lsq}$, perceptibly addresses the $GA$ problem by ensuring much lower dissipation in the very early shear layer regions. It is seen from figures 4.11, 4.12 and 4.15 that the results obtained using $\tilde{\Delta}_\omega + \sigma$ and $\Delta_{lsq} + S3QR$ are in close agreement with those provided by $\Delta_{SLA} + SMG$ in the jet core region. Downstream, $x/D \approx 7 - 8$, the predicted jet plume flow characteristics become more distinguishable. It is conducted by the LES model and corresponding turbulent dissipation provided by it. While the $\sigma$ model increases turbulent viscosity, with respect to results using $SMG$, $S3PQR$ model yields reduced levels (see figure 4.14). In general, the incorporation of an alternative LES model enhances the simulation of the jet and does not lead to any noticeable drawbacks.

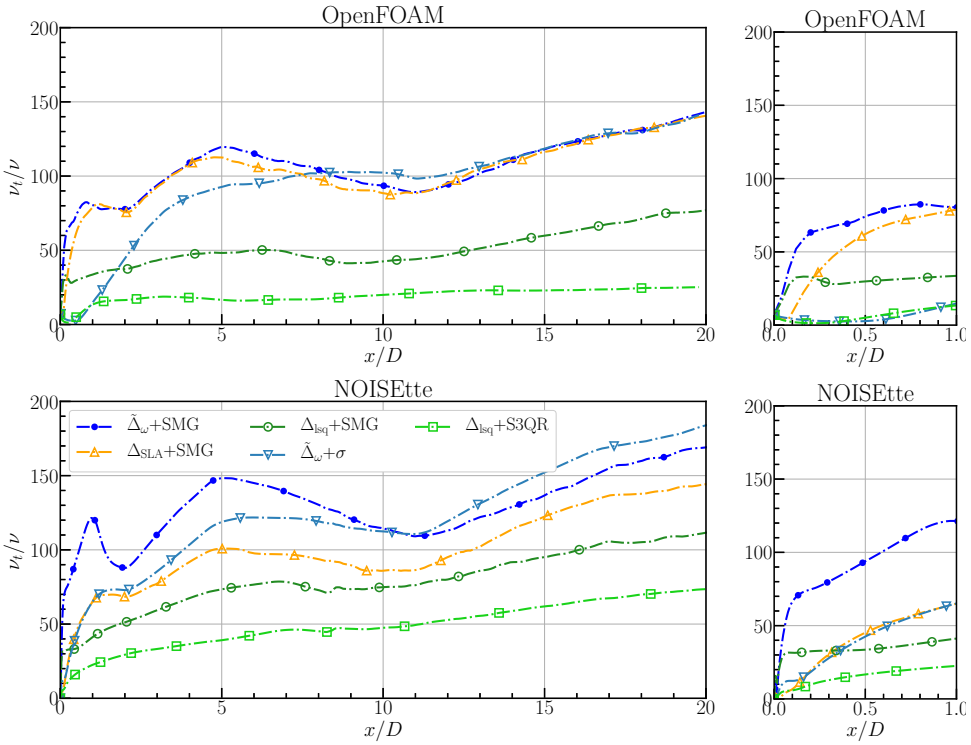


**Figure 4.14:** Average of the turbulent to molecular viscosity ratio over the lip line starting from the jet nozzle exit (left) and its zoom view near the edge (right).

## 4.5 Conclusions

The main aim of this work was to address, or at least partly mitigate, the Grey Area issue present in DDES models by means of techniques initially developed for LES turbulence models. In both applications there is an inherent need to reduce $\nu_{sgs}$ in critical regions, where flow does not strictly behave in a fully turbulent manner. For this reason, we decided to compare some recently developed Grey Area Mitigation techniques, such as $\Delta_{SLA} + SMG$ and $\tilde{\Delta}_\omega + \sigma$, with two new approaches initially designed for LES models (see section 3.3), in order to assess their ability to move from RANS to LES in areas where the flow presents a complex behaviour such as free shear layers.

The new approaches have been demonstrated to behave in a similar, and in some cases superior, manner to those techniques previously proposed to address those issues, such as $\Delta_{SLA} + SMG$ and $\tilde{\Delta}_\omega + \sigma$. This conclusion has been supported by applying the new approach to three different cases (considering incompressible and compressible flows), each computed with two

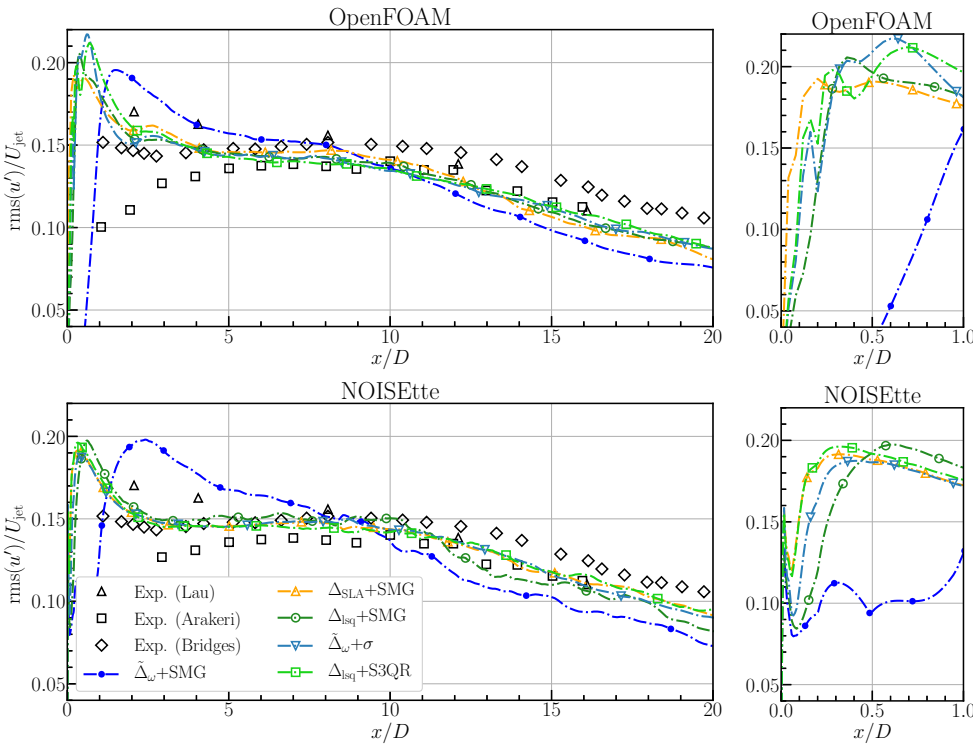


**Figure 4.15:** Average of root mean square of the stream-wise velocity over the lip line starting from the jet nozzle exit (left) and its zoom view near the edge (right).

different codes. As well as demonstrating improved performance, the new approaches are grounded in well-established physical *LES* modelling assumptions, whereas the standard *GAM* techniques incorporate a certain degree of tuning and blending which renders the model more empirical.
It is also worth mentioning that the beneficial influence of $\Delta_{lsq}$ is considerably more impactful than that obtained when using a differential operator sensitised to 2D flows, such as *S3QR*; the effect of these models is only noticed when the *SLS* is too difussive, such as for $\tilde{\Delta}_{\omega}$. In contrast, when $\Delta_{lsq}$ is used, the substitution of *SMG* with *S3QR* resulted in only minor differences.

# References

[1] P. R. Spalart, S. Deck, M. L. Shur, K. D. Squires, M. Kh Strelets, and A. Travin. A new version of detached-eddy simulation, resistant to ambiguous grid densities. *Theoretical*

*and Computational Fluid Dynamics*, 20(3):181–195, 2006.

[2] P. R. Spalart, W-H Jou, M. Strelets, and S. Allmaras. Comments on the Feasibility of LES for Wings, and on a Hybrid RANS/LES Approach. In *In 1st AFOSR international conference on DNS/LES*, pages 137–147, 1997.

[3] Charles Mockett, Marian Fuchs, Andrey Garbaruk, Michael Shur, Philippe Spalart, Michael Strelets, Frank Thiele, and Andrey Travin. Two Non-zonal Approaches to Accelerate RANS to LES Transition of Free Shear Layers in DES. In *Progress in Hybrid RANS-LES Modelling*, pages 187–201, Cham, 2015. Springer International Publishing.

[4] J. Smagorinsky. General circulation experiments with the primitive equations. *Monthly Weather Review*, 91(3):99–164, 1963.

[5] F. Nicoud, H.B. Toda, O. Cabrit, S. Bose, and J. Lee. Using singular values to build a subgrid-scale model for large eddy simulations. *Physics of Fluids*, 23(8):085106, 2011.

[6] M. Fuchs, J. Sesterhenn, F. Thiele, and C. Mockett. Assessment of novel DES approach with enhanced SGS modelling for prediction of separated flow over a delta wing. In *22nd AIAA Computational Fluid Dynamics Conference*, 2015.

[7] A. Probst, D. Schwamborn, A. Garbaruk, E. Guseva, M. Shur, M. Strelets, and A. Travin. Evaluation of grey area mitigation tools within zonal and non-zonal RANS-LES approaches in flows with pressure induced separation. *International Journal of Heat and Fluid Flow*, 68:237–247, 2017.

[8] Mikhail L. Shur, Philippe R. Spalart, Mikhail Kh Strelets, and Andrey K. Travin. An Enhanced Version of DES with Rapid Transition from RANS to LES in Separated Flows. *Flow, Turbulence and Combustion*, 95(4):709–737, 2015.

[9] Ekaterina K. Guseva, Andrey V. Garbaruk, and Mikhail Kh Strelets. Assessment of Delayed DES and Improved Delayed DES Combined with a Shear-Layer-Adapted Subgrid Length-Scale in Separated Flows. *Flow, Turbulence and Combustion*, 98(2):481–502, 2017.

[10] F X Trias, D. Folch, A. Gorobets, and A. Oliva. Building proper invariants for eddy-viscosity subgrid-scale models. *Physics of Fluids*, 27(6):065103, 2015.

[11] F X Trias, A. Gorobets, and A. Oliva. A new subgrid characteristic length for large-eddy simulation. *Physics of Fluids*, 29:115109, 2017.

[12] A Pont-Vílchez, D Santos, F X Trias, A Duben, A Revell, and A Oliva. Assessment of LES techniques for mitigating the Grey Area in DDES models. In *8th European Conference for Aeronautics and Aerospace Sciences*, 1-4 July, Madrid, Spain, 2019.

[13] A. Pont-Vílchez, F. X. Trias, A. Revell, and A. Oliva. Assessment and comparison of a recent kinematic sensitive subgrid length scale in hybrid rans-les. In Yannick Hoarau, Shia-Hui Peng, Dieter Schwamborn, Alistair Revell, and Charles Mockett, editors, *Progress in Hybrid RANS-LES Modelling*, pages 97–107, Cham, 2020. Springer International Publishing.

[14] J C Vogel and J K Eaton. Combined Heat Transfer and Fluid Dynamic Measurements Downstream of a Backward-Facing Step. *J. Heat Transfer*, 107(4):922–929, 1985.

[15] A. Pont-Vílchez, F. X. Trias, A. Gorobets, and A. Oliva. Direct numerical simulation of backward-facing step flow at $re_\tau = 395$ and expansion ratio 2. *Journal of Fluid Mechanics*, 863:341–363, 2019.

[16] M.L. Shur, P.R. Spalart, and M.K. Strelets. Jet noise computation based on enhanced DES formulations accelerating the RANS-to-LES transition in free shear layers. *International Journal of Aeroacoustics*, 15(6-7):595–613, 2016.

[17] M. Fuchs, C. Mockett, M. Shur, M. Strelets, and J.C. Kok. Single-stream round jet at M = 0.9. In C. Mockett, W. Haase, and D. Schwamborn, editors, *Go4Hybrid: Grey Area Mitigation for Hybrid RANS-LES Methods*, volume 134, pages 125–137, Cham, 2018.

[18] I V Abalakin, P A Bakhvalov, A V Gorobets, A P Duben, and T K Kozubskaya. Parallel research code NOISEtte for large-scale CFD and CAA simulations. *Vychisl. Metody Programm.*, 13(3):110–125, 2012.

[19] A. Wray. Unpublished DNS data. Available on AGARD database: "Test Cases for the Validation of Large- Eddy Simulations of Turbulent Flows", 1997.

[20] Jark C. Lau, Philip J. Morris, and Michael J. Fisher. Measurements in subsonic and supersonic free jets using a laser velocimeter. *Journal of Fluid Mechanics*, 93(1):1–27, jul 1979.

[21] J. C. Lau. Effects of exit Mach number and temperature on mean-flow and turbulence characteristics in round jets. *Journal of Fluid Mechanics*, 105(1):193–218, 1981.

[22] J Simonich, S Narayanan, T Barber, and M Nishimura. High subsonic jet experiments. I - Aeroacoustic characterization, noise reduction and dimensional scaling effects. In *6th Aeroacoustics Conference and Exhibit*. American Institute of Aeronautics and Astronautics, 2000.

[23] V. H. Arakeri, A. Krothapalli, V. Siddavaram, M. B. Alkislar, and L. M. Lourenco. On the use of microjets to suppress turbulence in a Mach 0.9 axisymmetric jet. *Journal of Fluid Mechanics*, 490:75–98, 2003.

[24] James Bridges and Mark Wernet. Establishing Consensus Turbulence Statistics for Hot Subsonic Jets. In *16th AIAA/CEAS Aeroacoustics Conference*, Aeroacoustics Conferences. American Institute of Aeronautics and Astronautics, jun 2010.

[25] M.L. Shur, P.R. Spalart, and M.Kh. Strelets. LES-based evaluation of a microjet noise reduction concept in static and flight conditions. *Procedia Engineering*, 6:44–53, jan 2010.

[26] Alexey P. Duben and Tatiana K. Kozubskaya. Evaluation of quasi-one-dimensional unstructured method for jet noise prediction. *AIAA Journal*, 57(7):1–14, 2019.

[27] Philippe Spalart, Michael Shur, Michael Strelets, and Andrey Travin. *Sensitivity of Landing-Gear Noise Predictions by Large-Eddy Simulation to Numerics and Resolution*. 2012.

[28] A. Gorobets. Parallel algorithm of the noisette code for cfd and caa simulations. *Lobachevskii Journal of Mathematics*, 39(4):524–532, 2018.

[29] B. Koobus, F. Alauzet, and A. Dervieux. Numerical algorithms for unstructured meshes. In F. Magoules, editor, *Computational Fluid Dynamics*, Progress in Astronautics and Aeronautics, pages 131–204. CRC Press, 2011.

[30] I.V. Abalakin, P.A. Bakhvalov, and T.K. Kozubskaya. Edge-based reconstruction schemes for unstructured tetrahedral meshes. *International Journal for Numerical Methods in Fluids*, 81(6):331—-356, 2016.

[31] C. D. Winant and F. K. Browand. Vortex pairing : The mechanism of turbulent mixing-layer growth at moderate Reynolds number. *Journal of Fluid Mechanics*, 63(2):237–255, 1974.

# 5

# Conclusions and further work

## 5.1 Concluding remarks

The first chapter has attempted to provide a general overview of turbulence, from a physical and mathematical point of views. The different numerical approaches for modelling turbulence have also been introduced. The implications of the turbulence model selection are discussed using a practical example, showing up its huge impact in both computational resources and degree of modelling. These studies, together with RANS unreliability for certain configurations, the unfeasibility of LES/DNS simulations for industrial applications and the impressive rate of growth of the computational resources during the last years, are clear indicators that Hybrid RANS-LES models will be the next main technique to be adopted by the industrial sector in the near future (shifting the RANS predominance).
Within the family of hybrid models, Delayed-Detached Eddy Simulation (DDES) outstands due to its user-friendly non-zonal approach and its proved success in several applications. Despite their benefits, these models usually suffer from a slow RANS to LES transition (named *Grey Area*), resulting in unphysical delays of critical flow instabilities in sensitive regions, such as Kelvin-Helmholtz structures in free shear layers. In this regard, this thesis has performed a consistent study of different techniques for mitigating such a delay, as well as presenting a promising easy-to-apply new strategy. This is explained in detail in chapter 3 and tested in chapter 4. However, due to the lack of publicly available highly reliable data set, we have previously carried out a DNS of a BFS at $Re_\tau = 395$ and expansion ratio (ER) two in the second chapter for comparison purposes. As a result, the thesis provides a highly reliable data set publicly available on internet, as well as a competitive new technique for mitigating the *Grey Area* shortcoming.

### 5.1.1 Concluding remarks on the DNS simulation

A DNS of a BFS with a $ER = 2$ has been carried out at $Re_\tau = 395$, defining a case close to the recirculation length asymptotic behaviour. A turbulent channel flow has been used as an inflow, which has been obtained from a previous simulation. All tests have provided reasonable results concluding that the parameter values satisfy the challenging DNS requirements. Once verified, the DNS results have been compared with the experimental and numerical studies present in the literature. Besides presenting good agreement with the experimental results, the nearness in the recirculation length asymptotic behaviour zone has also been observed.
The rate of growth of the Kelvin-Helmholtz instabilities have been identified through two-point correlations in the stream-wise and normal directions. A switching from circular to elliptical structures has been detected close to the step-edge (up to $\sim 0.4h$) produced by the advection velocity and the vortex pairing phenomenon. The elliptical shape trend agrees with experimental observations, showing a major-to-minor axis ratio close to 2.
Finally, the results obtained with this DNS have been used in the present thesis for comparing the reliability of the new approaches for mitigating the *Grey Area* phenomenon in DDES models. Currently, DNS data is publicly available on internet for being used by the scientific community.

### 5.1.2 Concluding remarks on the new GAM

The main aim of this thesis was to address, or at least partly mitigate, the Grey Area issue present in DDES models by means of techniques initially developed for LES turbulence models. In both applications there is an inherent need to reduce $\nu_{sgs}$ in critical regions, where flow does not strictly behave in a fully turbulent manner. For this reason, we decided to compare some recently developed Grea Area Mitigation techniques, such as $\Delta_{SLA} + SMG$ and $\tilde{\Delta}_\omega + \sigma$, with two new approaches initially designed for LES models ($\Delta_{lsq}$ and $S3QR$), in order to assess their ability to move from RANS to LES in areas where the flow presents a complex behaviour such as free shear layers.
The new SLS, $\Delta_{lsq}$, was initially tested and calibrated with the DHIT case, where we observed how $\tilde{\Delta}_\omega$ offered better resiliance capabilities in comparison to $\Delta_{lsq}$. This feature is associated with the intrinsic definition of $\tilde{\Delta}_\omega$, where the diagonal value of the cell volume is assessed. By definition, it means that $\tilde{\Delta}_\omega$ is always going to depend at least on 2 dimensions, being sensitive to the mesh anisotropies, but at the same time limiting their downward excursions, something that cannot be guaranteed in the $\Delta_{lsq}$.
It is worth mentioning here that even we have observed an interesting clear advantage of $\tilde{\Delta}_\omega$ and $\Delta_{SLA}$ over $\Delta_{lsq}$ in the DHIT it case, this is not observed in the other flow configurations presented in the thesis (BFS and jet). Regarding these other cases, $\Delta_{lsq}$ have been demonstrated to behave in a similar, and in some cases superior, manner to those techniques previously proposed to address the Grey Area, such as $\Delta_{SLA} + SMG$ and $\tilde{\Delta}_\omega + \sigma$. This conclusion has been supported by applying the new approach to incompressible and compressible flows, and also running the simulations using two different codes, *OpenFOAM* and *NOISEtte*. The same trends have been observed in all the comparisons.
Special attention has been focused on the BFS case, due to its suitability for studying the free-shear layer development and also for the fact of having reliable DNS data. In both BFS we

observed how $\tilde{\Delta}_\omega + SMG$ presented a clear delay in the shear layer oscillations in comparison to other SLS, such as $\Delta_{SLA} + SMG$ and $\Delta_{lsq} + SMG$. However, in the simulations carried out with *NOISEtte*, $\tilde{\Delta}_\omega + SMG$ is the one that presented the best results downstream of the step edge, once the delay of the shear layer was recovered. This effect is due to the fact the vortex created in the shear layer with $\tilde{\Delta}_\omega + SMG$ are more energetic than those created with the other SLS ($\Delta_{lsq}$ and $\Delta_{SLA}$). In other words, as the difussion is higher and the convection lower, the eddies created in the shear layer does not decompose in smaller eddies so quickly. This mechanism explains the presence of higher oscillation downstream of the step-edge for those SLS which are too diffussive. It is also true that this effect is not so well observed in the OpenFOAM case. This is attributed to the convective schemes, as the one used by *NOISEtte* provides lower levels of numerical dissipation.
Regarding the turbulent models behavior close to the wall, they have been studied by means of the sking friction, $\left\langle C_f \right\rangle$. We have observed that either in the *BFS-VE* or the *BFS-DNS* , $\Delta_{lsq}$ presented a slightly better performance in the lower wall. Apart from this, we have confirmed that both $\Delta_{lsq} + SMG$ and $\tilde{\Delta}_\omega + SMG$ behave in a really similar way. This fact was not so predictible considering that $\Delta_{lsq} + SMG$ can present values around $\Delta x_n$ (where $n$ indicates the normal wall direction) close to the wall (figure 3.3), which could severly harm the DDES shielding function, reducing the RANS area because of the LES invasions. It would directly lead to a reduction of the turbulent viscosity, so strongly affecting the flow properties close to the wall such as the skin friction. Therefore, the similar behavior observed in $\Delta_{lsq} + SMG$ and $\tilde{\Delta}_\omega + SMG$ clearly indicates that the new approach does not significantly affects the DDES shielding function in such flow configuration. Unfortunately, it cannot be extrapolated to other cases, so extra research in this area is clearly needed. Similar trends were observed with the pressure coefficient, $\left\langle C_p \right\rangle$, distribution, where $DDES - SA$ models present a clear advantage over $RANS - SA$, as they are clearly benefited from the transient resolution of the flow at the shear layer. In particular, the new SLS approach, $\Delta_{lsq}$, presented a better transition in the adverse pressure gradient zone than $\tilde{\Delta}_\omega$.
Another interesting observation from the skin friction distribution is the recirculatino length, which has presented a similar accuracy in all DDES turbulent models.
Apart from demonstrating an acceptable performance in all cases, the new approaches are grounded in well-established physical *LES* modelling assumptions, whereas the standard *GAM* techniques incorporate a certain degree of tuning and blending which renders the model more empirical.
It is also worth mentioning that the beneficial influence of $\Delta_{lsq}$ is considerably more impactful than the one obtained when using a differential operator sensitised to 2D flows, such as *S3QR*; the effect of these models is only noticed when the SLS is too difussive, such as for $\tilde{\Delta}_\omega$. In contrast, when $\Delta_{lsq}$ is used, the substitution of $SMG$ with *S3QR* resulted in only minor differences.

## 5.2 Further work

The future strategies to develop and continue this study are mainly focused on the application of the new approach for mitigating the *Grey Area* in new flow configurations and also investigating how they perform when other physics are coupled to the fluid dynamics.
First, for the applicability in new configurations, we are mainly concerned in understanding how the new approach, $\Delta_{lsq}$, can affect the RANS area close to the wall (shielding function). Even though we have observed that the skin friction in the BFS behaves similarly in all turbulence models (so indicating that the shielding function is not significantly affected by the new approaches), it is not clear which effect they can have in other scenarios.
In particular, for those cases with free inflow boundary conditions, where the $\nu_t$ values are significantly smaller than the ones presented by the cases studied in this thesis. For instance, this can be the case of any bluff-body, such as circular cylinders or airfoil profiles, or any other flow configuration where the flow does not has a developed turbulence at the inflow, such as the wall-mounted hump. In all these situations (at high Reynolds values), the effects of turbulence can be present either at the very beginning or developed through the wall. In DDES models, only the RANS-mode close to the wall can attempt to control the skin friction development; provide acceptable values of $\nu_t$; and predict the separation point (in case of any). LES is clearly incapable of managing such situations properly because the meshes used in DDES are insufficient for developing a proper level of resolved turbulence in such regions. Therefore, a reduction/damage of the RANS area close to the wall can have an impact into the overall simulation. This is the case for the new SLS approach, as the values it provides can be around $\Delta x_n$ (where $n$ indicates the normal wall direction) close to the wall. This issue has not been observed in this thesis, basically because all the considered cases presented a developed turbulence (high $\nu_t$ values) at the inflow, activating the shielding function and providing an stable RANS region in the critical areas.
Besides the skin friction and the flow behavior close to the wall, there is another interesting topic related to the flow configurations chosen in this thesis. This is related to the clear stability advantage of $\tilde{\Delta}_\omega$ and $\Delta_{SLA}$ over $\Delta_{lsq}$ observed in the DHIT case. Even though it was not clearly observed in the other cases (BFS and jet), it does not mean that it could play an important role in simulating real complex industrial application, where the common meshes usually present a high level of anisotropy, resembling the book and pencil meshes commented in section 4.2.
After studying the benefits and the possible flaws provided by the new approach into the flow dynamic DDES simulations, there are still lots of questions that remain unanswered. In particular, the effect that the new approaches can cause in simulations where other physics are coupled, such as fluid-structure interaction, chemical species reaction, heat transfer, aeroacoustics. Apparently, all simulations can be benefited from a better resolution of the instabilities in the shear layer area (in other words, reduction of the Grey Area issue), as all these couplings clearly depend on the quality of the unsteady data. In this regard, the chosen flow configurations studied in this thesis set a good basis for analysing such couplings, as the BFS cases are commonly used for testing heat transfer and chemical species models in canonical geometries, and Jet is a well-known case for the aeroacoustics field.